A MULTI-SCALE INVESTIGATION OF WAVES IN THE SOUTH CHINA SEA: INTEGRATING HINDCASTS, TREND ANALYSIS, MULTIFRACTAL SIGNATURES, AND NATURE-BASED SOLUTIONS

TIZIANO BAGNASCO

PhD

The Hong Kong Polytechnic University

2026

The Hong Kong Polytechnic University

Department of Civil and Environmental Engineering

A multi-scale investigation of waves in the South China Sea: integrating hindcasts, trend analysis, multifractal signatures, and nature-based solutions

Tiziano Bagnasco

A thesis submitted in partial fulfilment of the requirements for the degree of Doctor of Philosophy

November 2025

CERTIFICATE OF ORIGINALITY

I hereby declare that this thesis is my own work and that, to the best of my knowledge and belief, it reproduces no material previously published or written, nor material that has been accepted for the award of any other degree or diploma, except where due acknowledgment has been made in the text.

______________________________ (Signed)

Tiziano Bagnasco

______________________________ (Name of student)

Dedication

This thesis is dedicated to all those who have supported me throughout my academic journey and personal life. I extend my deepest gratitude to my family, especially my parents, for their unwavering support and for funding my education.

Abstract

The South China Sea (SCS) is a region of critical economic and ecological importance, subject to complex wave climates influenced by monsoon systems and climate change. However, a comprehensive, holistic understanding of its wave dynamics, from basin-scale extremes to coastal interactions, is still needed. This thesis aims to provide a high-resolution, multi-scale characterization of wave processes in the SCS. It specifically investigates long-term trends in annual maximum wave heights, their underlying multifractal properties, and the efficacy of mangroves as a natural coastal defense.

To achieve this, a two-way coupled wave-current high-resolution hindcast was developed for the SCS. A more specific treatment was reserved for typhoons and extreme events, that were simulated with the Holland parametric wind model. The hindcast data were then analyzed using a non-stationary extreme value approach to characterize significant wave height trends and for return level estimations. Moreover, a multifractal detrended fluctuation analysis (MF-DFA) was performed to the significant wave height series to uncover their scaling properties. Finally, the wave dissipation capacity of mangroves was quantified through a focused case study in the Mai Po Nature Reserve, Hong Kong.

The results reveal a solid performance of the SCHISM-WWMIII model, with

the wave-current coupled hindcast providing robust nearshore skills, enhanced by the Holland model for accurate typhoon peak H_S and storm surge predictions. Non-stationary extreme value analysis identifies significant wave height trends, with most pronounced negative trends of about -0.045 m/year in northern and eastern SCS and positive trends up to around 0.019 m/year in southern regions, amplified by 20-30% during typhoon seasons, and 25-year return levels reaching 12 m in central-northwestern SCS, with projected increases by 2122. MF-DFA uncovers synoptic (10-21 days), seasonal (5-7 months), and inter-annual (1.4-1.7 years) time scales, with northern SCS showing super-persistence (Hurst exponents > 1.8) and southern regions greater stability. Mangrove dissipation at Mai Po reduces wave heights from 1.2-1.7 m offshore to centimeters inland, primarily due to the effects of a shallow bathymetry, indicating that the effects of vegetation are marginal.

This research establishes a robust numerical framework and provides novel insights into the non-stationary and multiscale nature of SCS waves. The findings have direct implications for coastal hazard mitigation, climate adaptation planning, and the conservation of nature-based coastal defenses like mangrove ecosystems.

Publications arising from the thesis

Bagnasco, T., A. Stocchino, M. I. Vousdoukas, and J. Wang (2025). "A two-way coupled wave–current high resolution hindcast for the South China Sea". In: *Applied Ocean Research* 161, p. 104672.

Bagnasco, Tiziano et al. (2025). "Characterization of significant wave height trends in the South China Sea based on wave hindcast results: a non-stationary extreme value approach". In: *Applied Ocean Research* (Currently under review)

International Conference Participation

- RCEM 2023-International Conference on River, Coastal and Estuarine Morphodynamics, Urbana-Champaign, Illinois, USA (2023)
- ICCE 2024-International Conference on Coastal Engineering, Rome, Italy (2024)
- The 3rd Hong Kong and Macau Ocean & Areas of Excellence (AoE) Forum, Hong Kong (2024)

Acknowledgements

I must once again acknowledge my family, to whom I owe a profound debt of gratitude for their overwhelming support throughout this endeavor. My appreciation also extends to my supervisor for his constant encouragement and belief in my potential, to my friends for always being there for me, and to my colleagues and all the individuals whose paths have crossed mine during this particular time of my life. I also hold a special appreciation for all my loved ones—past, present, and future—for their unwavering presence.

Thank you.

Contents

List of Figures

List of Tables

Chapter 1

Introduction

1.1 Research context and motivation

The South China Sea (SCS) is one of the most dynamic and economically vital marine regions in the world, characterized by complex wave climates driven by seasonal monsoons, tropical cyclones, and intricate bathymetric features. Its waves influence a wide range of activities, from shipping and offshore engineering to coastal protection and ecosystem stability. Despite its importance, a comprehensive understanding of long-term wave dynamics, extreme events, and their interactions with coastal systems remains incomplete, particularly at regional scales. This knowledge gap is critical to address, given the increasing threats posed by climate change, including rising sea levels and intensifying storm activity, which may alter wave regimes and exacerbate coastal vulnerabilities.

A primary challenge in studying wave climatology in the SCS is the scarcity of long-term, high-resolution observational data. While satellite altimetry and buoy measurements provide valuable snapshots, they are often limited in spatial coverage or temporal duration. To overcome this limitation, this research employs numerical wave hindcasting, a powerful approach that reconstructs historical wave conditions using the hydrodynamic model SCHISM fully coupled to the spectral wind wave model WWMIII. By generating a multi-decadal hindcast database for a large portion of the SCS (covering the years 1970-2022), this study provides an unprecedented foundation for analyzing wave climate variability, validating models against sparse observations, and establishing baseline data for further statistical and dynamical investigations. A dedicated section of this work is devoted to the analysis of typhoons and extreme events that occurred in the selected time frame: the Holland parametric wind model was deployed to better reproduce and simulate the extreme events.

Beyond hindcasting, this thesis advances the understanding of wave dynamics through several innovative analytical approaches. It examines long-term trends and applies non-stationary extreme value analysis (NEVA) to H_S data arising from the above-mentioned wave hindcast, addressing a critical limitation of traditional extreme value models that assume climate stationarity. Given the evidence of changing storm patterns and sea-level rise, this approach offers a more realistic framework for assessing future risks to coastal infrastructure and marine operations. In this way it is possible to detect and quantify the presence of monotonic trends in the study domain in order to locate the most vulnerable areas. A comparison is then made between the dataset that includes the Holland simulated extreme events and the dataset that does not account for them. Moreover, the analysis allows to estimate return levels of H_S with different approaches and for given return times.

Furthermore, the research explores the complexity of wave climate variability through multifractal detrended fluctuation analysis (MF-DFA), a method capable of uncovering hidden scaling behaviors, long-term persistence, and intermittency in the H_S time series in the SCS. Such insights are valuable for improving predictive models and understanding the underlying physical processes governing wave climate dynamics.

Finally, recognizing the increasing importance of nature-based solutions for coastal protection, this research investigates the role of mangroves as natural wave attenuators. The area investigated in this thesis is the Mai Po nature reserve in Hong Kong. Nine water level gauges were installed in three different sections and acquired water level elevations in 2023 and 2024. Mangrove forests, with their dense root systems and vegetation, are known to dissipate wave energy, yet their effectiveness under varying hydrodynamic conditions in the SCS remains understudied. By quantifying wave attenuation through numerical modeling and empirical validation, this work provides critical insights for coastal resilience strategies, particularly in regions where mangroves serve as a first line of defense against erosion and storm surges.

The motivation for this research is both scientific and societal. From a scientific perspective, it advances the state of knowledge in wave climate modeling, non-stationary extremes, and nonlinear time series analysis, offering methodologies that can be applied to other ocean basins facing similar data limitations. From a societal standpoint, the findings have direct implications for maritime safety, coastal planning and adaptation, supporting policymakers, engineers, and environmental managers in making informed decisions.

By integrating numerical hindcasting, statistical extremes, fractal analysis, and ecological interactions, this thesis delivers a comprehensive perspective on wave dynamics in the SCS in an era of growing climatic uncertainty.

1.2 Research objectives and significance

The overarching goal of this thesis is to advance the understanding of wave dynamics in the South China Sea (SCS) through a combination of numerical modeling, statistical analysis, and ecological applications. To achieve this, the study is structured around four primary objectives.

The research aims to develop a high-resolution, multi-decadal wave hindcast for a large portion of the SCS using state-of-the-art spectral wave models such as SWAN or WAVEWATCH III. This hindcast will serve as a foundational dataset for reconstructing historical wave conditions, validating model performance against sparse observational data, and analyzing the spatial and temporal variability of wave climates under different meteorological forcings, including monsoons and tropical cyclones.

The study seeks to investigate long-term trends and non-stationary extreme wave behavior in the SCS. Traditional extreme value analysis often assumes climatic stationarity, which may lead to underestimations of future risks in a changing climate. By applying advanced non-stationary extreme value models (NEVA) to H_S data, this work will provide more accurate estimates of return levels for extreme waves, offering critical insights for coastal hazard assessment and infrastructure design.

Moreover, the research explores the multifractal characteristics of H_S time series through multifractal detrended fluctuation analysis (MF-DFA). This approach will identify scaling behaviors, long-range dependence, and intermittency in wave climate variability, shedding light on the underlying dynamical processes that govern wave generation and propagation in the SCS. Such findings could enhance the predictability of wave climates and contribute to improved numerical modeling techniques.

Finally, the research quantifies wave attenuation through mangrove forests using numerical simulations and empirical validations, providing actionable knowledge for nature-based coastal protection strategies.

This study holds substantial scientific and practical significance, addressing critical gaps in wave climate research while offering actionable insights for marine industries, policymakers, and coastal communities. From a scientific perspective, this research contributes to several advancing fields. The high-resolution wave hindcast fills a crucial data gap in the SCS, enabling more accurate climatological studies and model validations. The application of non-stationary extreme value analysis challenges traditional assumptions in wave climate studies, providing a methodological framework that can be adapted to other regions experiencing climatic non-stationarity. Meanwhile, the multifractal analysis of H_S time series offers novel insights into the complexity of wave dynamics, potentially refining stochastic and deterministic wave prediction models.

From a practical standpoint, the findings have direct implications for marine safety and coastal resilience. The improved characterization of extreme wave risks supports safer maritime operations and more robust coastal infrastructure design, particularly in typhoon-prone regions.

Furthermore, the investigation of mangroves as natural wave attenuators underscores the importance of ecosystem-based adaptation in coastal protection. By quantifying the wave-dissipating capacity of mangroves, this research provides empirical support for conservation efforts and the integration of nature-based solutions into coastal management plans. This is particularly relevant for vulnerable communities in the SCS, where mangroves serve as critical buffers against erosion and storm surges, providing a framework that can be adapted for other vulnerable coastal regions globally.

In summary, this thesis bridges fundamental and applied research, offering a holistic understanding of wave dynamics in the SCS while delivering tools and knowledge that can inform climate adaptation, marine resource management, and sustainable development in the region.

1.3 Thesis structure and organization

This thesis is organized to systematically investigate wave dynamics in the South China Sea, progressing from foundational concepts to advanced analyses and practical applications.

The Introduction establishes the research context, highlighting the scientific and societal motivations for studying wave hindcasting, extreme events, and coastal interactions in this region. It clearly defines the study's objectives and anticipated contributions to both academic research and coastal management practices.

A comprehensive Literature Review follows, critically examining existing work on numerical wave modeling, hindcasting methodologies, non-stationary extreme value analysis, and the role of mangroves in wave attenuation. This chapter synthesizes current knowledge while identifying key gaps that the present research aims to address.

The Methodology chapter details the integrated numerical framework, combining the SCHISM model for hydrodynamic processes with WWMIII for spectral wave simulations. It elaborates on the implementation of typhoon parametrizations, trend analysis techniques, multifractal detrended fluctuation analysis (MF-DFA), and approaches for quantifying mangrove attenuation effects.

Results are presented thematically, beginning with validation of the wave hindcast system before exploring observed trends in extreme wave behavior, multifractal characteristics of wave height time series and mangrove-induced wave dissipation. Each section includes targeted interpretation of the findings, maintaining direct alignment with the research objectives.

Finally, the last chapter synthesizes the key insights and places them within the broader context of coastal hydrodynamics and climate change adaptation. It critically evaluates the study's contributions, acknowledges methodological limitations, and proposes actionable directions for future research. The chapter concludes by emphasizing the implications of the findings for science, policy, and sustainable coastal development.

Supplementary technical details and extended datasets are provided in the Appendices to ensure reproducibility and support further investigation.

Chapter 2

Research background and literature review

2.1 Numerical modeling approaches in coastal hydrodynamics

The selection of numerical models is primarily determined by the specific objectives of the analysis. In recent years, unstructured-grid models have emerged as a robust alternative to traditional regular-grid models, particularly for large-scale applications, as highlighted by Mentaschi et al. (2023). Unstructured-grid models offer significant advantages in coastal and oceanic simulations due to their ability to generate flexible meshes that conform to complex shorelines and intricate bathymetric features. This adaptability is particularly valuable in regions with archipelagos or irregular topographies, where resolution requirements vary considerably across the domain. The increasing demand for high-resolution simulations across diverse spatial and temporal scales has further driven the adoption of unstructured-grid approaches (Dietrich et al. 2011).

Among the most widely used unstructured-grid circulation models are the Finite-Volume Coastal Ocean Model (FVCOM, C. Chen et al. (2003)) and the System of HydrodYnamic Finite Element Modules (SHYFEM, Federico et al. (2017) and Umgiesser et al. (2004)). Other prominent models include ADCIRC (Luettich et al. (1992) and Lynch et al. (1996)), TELEMAC (Galland et al. (1991)), and the Semi-Implicit Cross-scale Hydroscience Integrated System Model (SCHISM, Y. Zhang and Baptista (2008), Y. J. Zhang et al. (2016), and Y. J. Zhang et al. (2023)). These models have been extensively applied in coastal and estuarine hydrodynamics due to their ability to efficiently represent complex geometries and multi-scale processes.

In the context of spectral wave modeling, several frameworks are commonly employed. These include SWAN (Booij et al. (1999)), TOMAWAC (Benoit et al. (1997)), and WAVEWATCH III (Tolman (1991)). Additionally, models such as WAM (Group (1988)), MIKE21 SW (Sørensen et al. (2005)), CREST (Ardhuin et al. (2001)), and WWMIII (Roland et al. (2008), Roland et al. (2009), and Roland et al. (2012)) are widely used for simulating wave dynamics across different environments. The versatility of these models allows for accurate representation of wave processes in coastal regions, further enhancing the capabilities of modern hydrodynamic simulations.

The integration of unstructured-grid circulation models with spectral wave models has significantly advanced the field of coastal hydrodynamics, enabling more precise and efficient simulations of coupled wave-current interactions in complex coastal systems.

2.2 Wave hindcasting

The existing literature provides several examples and applications of both global-scale wave hindcasts (M. A. Hemer et al. 2013; Perez et al. 2017; Stopa et al. 2019; Mentaschi et al. 2023) and more regionally focused studies (Mirzaei et al. 2013; Liang et al. 2016; Shi et al. 2019). The Eastern part of the North Atlantic coast was studied by Bauer (2001), who produced a high-resolution ocean wave hindcast from 1981 to 1993 with the WAM wave model. Pilar et al. (2008) generated a 44-year wave hindcast (1958-2001) with the WAM model and Dodet et al. (2010) investigated the wave climate variability using a 57-year wave hindcast (1953-2009) obtained with a spectral wave model forced with reanalysis wind fields. Later in 2013, Bertin et al. (2013) developed a 109-year wind wave hindcast for the North Atlantic Ocean based on the 20th century atmospheric reanalysis (20CR). Recently, a new dataset for the North Atlantic European waters has been published with a relatively high spatial resolution (Alday and Lavidas 2024). Mentaschi et al. (2013b) analyzed the performance of WAVEWATCH III in the Western Mediterranean Sea concerning seventeen storm events. The Central and South Pacific was investigated by Durrant et al. (2014) while generating a 31-year global wave hindcast with the deployment of WAVEWATCH III. Perez et al. (2017) also generated a global wave hindcast from 1979 to 2015 with an improved resolution of 0.25° in coastal areas and near the poles. Only later, Mentaschi et al. (2023) developed a 73-year global hindcast of waves and storm surges utilizing SCHISM-WWMV and considering an unstructured mesh characterized by more than 650000 nodes and with the highest resolutions ranging between 2 and 4 kilometers near costal areas.

The area examined in this workr encompasses a substantial portion of the SCS: a marginal sea of the Western Pacific Ocean enclosed by the Indochinese Peninsula, China, Taiwan, Philippines, Indonesia, Malaysia and Borneo. During the summer and autumn seasons, this region experiences the impact of intense winds and typhoons, occasionally leading to significant harm to coastal structures, offshore installations, and vessels (Shi et al. 2017; H. Wang et al. 2017). In fact, the climatology of this area is strongly influenced by the East Asia monsoon, with northerly winds prevailing during the boreal winter and southerly winds dominating in the summer. Qian et al. (2020) studied the climatology of wind-seas and swells of the SCS and assessed that the significant wave heights of wind seas are predominant and significantly higher than the significant wave heights of swells. Moreover, they highlighted that the wind is affected by strong seasonality and ranges from mean values of wind velocities greater than 8 m/s during winter to values around 6 m/s during summer. Regarding the wave conditions in the area, J. Wang et al. (2021) analyzed the spatiotemporal variations of H_S in the SCS and found that the maximum values of significant wave heights occur during summer (typically between 5 m and 11 m with peaks that can reach 15 m in July) and lowest values occur during winter and spring with values between 1 m and 7 m. Moreover, the spatial pattern of the maximum significant wave height is found to be consistent with the trajectories of most tropical cyclones. Regarding the tidal conditions, the South China Sea predominantly features a microtidal regime, with the largest M2 tide amplitude of about 2 meters in the Taiwan Strait, as reported by a numerical study of the tidal dynamics in the SCS by Zu et al. (2008).

Extensive research efforts have been undertaken in this region to develop forecasting or hindcasting of waves, analyze wave climate trends, and achieve a comprehensive understanding of the wave dynamics. Several studies focused on wave condition analysis and wave energy assessment (Z. Wang et al. 2018; Jiang et al. 2019; Sun et al. 2020; S. Yang et al. 2020). Researchers have also been exploring the effects of concurrent storm-tide-tsunami events (J. Wang and P. L.-F. Liu 2021) and the observations and modeling of typhoon waves (S. Yang et al. 2015; Y. Xu et al. 2017; Wu et al. 2018). The literature also includes examples of wave hindcasts produced in this region. Mirzaei et al. (2013) conducted a 31-year wave hindcast using the WAVEWATCH III model, aiming to evaluate the long-term alterations and inter-annual variations in the wave climate of the SCS. The hindcast employed a minimum resolution of 0.3 degrees to depict the wave characteristics accurately and provided results every 3 hours, which could lead to neglecting important peaks in the wave height distributions. The wave climate in the Bohai Sea, Yellow Sea, and East China Sea for the period spanning 1990 to 2011 was investigated by Liang et al. (2016) using the SWAN model and a minimum resolution of 1 arcminute. Another study by Shi et al. (2019) produced a wave hindcast covering the time span from 1979 to 2017 along the Chinese coast reaching resolutions of 1 km in shallow areas deploying the TOMAWAC model. A limitation of the latter study is that, as noted in the conclusions, the long-term trends in the wave climate may be affected by temporal inhomogeneities in the wind field.

Numerical wave modeling can be performed accounting for the influence and interaction of currents or by neglecting them entirely. As mentioned by Kong et al. (2024), the exchange of data in two-way coupled models between waves and currents results in a more accurate representation of some real complex phenomena such as the wave-induced turbulent mixing in 3D applications (Kumar et al. 2012). Practice has shown that, typically, coupled models exhibit superior performance in simulating wave conditions compared to wave-only models (Kong et al. 2024). This improvement can be attributed to the inclusion of current effects, which play a significant role in accurately depicting phenomena such as dissipation, wave breaking, wave refraction and wave steepening (Ardhuin et al. 2012).

The analysis presented in this study is based on the two-way fully coupled SCHISM-WWMIII modeling system. A detailed description of the model setup is provided in the subsequent sections. The primary objective of this analysis is to produce a 53-year wave hindcast for a significant portion of the South China Sea, with a specific focus on the coastline of the Guangdong province, which is one of the most densely populated regions in China (Z. Chen et al. 2022) with a population of about 86.17 million, as per 2020 (Xie et al. 2024). The numerical simulations in terms of wave characteristics and water levels have been validated against offshore satellite altimeter observations, coastal wave measurement stations and tidal gauges.

2.3 Trend analysis and non-stationary extreme value analysis

The simplest and most straightforward method for assessing trends in sea state datasets is to perform a linear regression over certain variables of the time series. This methodology has been widely used to analyze H_S trends, including studies in the Northwest Pacific Ocean (Ruggiero et al. 2010), the western coast of the United States (Allan and Komar 2006), Gulf of Mexico (Appendini et al. 2014), the Arabian Sea (Shanas and Sanil Kumar 2014), the Balearic Sea (Cañellas et al.

2024), the South China Sea (Shi et al. 2019) and the Italian Seas (Martucci et al. 2010).

A modified approach that is not influenced by outliers and therefore provides an improved slope estimation is the so-called Theil-Sen (TS) method (Sen 1968; Theil 1992). The TS slope was employed to analyze trends in monthly quantiles in the Adriatic Sea (Pomaro et al. 2017). Vanem and Walker (2013) estimated long term trends of H_S in the North Atlantic ocean by means of the Theil-Sen estimator and then compared the results with other existing methods. More sophisticated approaches, such as the wavelet analysis, were used by Castelle et al. (2018) in order to assess the time-variation of temporal modes of variability in the Atlantic coast of Europe.

When analyzing changes and temporal trends of geophysical variables (such as temperature, wind velocities and wave characteristics), the non-parametric Mann-Kendall (MK) statistical test (Mann 1945; Kendall 1948) is the preferred method. Concerning the assessment of trends in the H_S distribution, the MK test was used by J. Wang et al. (2021) to identify significant trends in the South China Sea based on a 71-year old wave reanalysis. Caloiero et al. (2019) performed a trend analysis based on the MK test in the southern part of Italy while similar approaches were conducted by Nguyen et al. (2022) in Vietnam and by Aydoğan and Ayat (2018) in the Black Sea.

While the techniques discussed above (linear regression, Theil-Sen slope estimator, and non-parametric Mann-Kendall test) are effective for the detection and quantification of trends in wave climate parameters, they do not directly address changes in extreme wave conditions, which are critical for coastal risk assessment and engineering design. In order to evaluate extremes, extreme value analysis

(EVA) provides a framework for estimating return levels under the assumption of stationarity or by incorporating temporal trends (non-stationary EVA). Typically, traditional infrastructure design has been based on stationary return levels, which assume that the statistical properties of extreme events do not vary over time (Tank et al. 2009). However, robust evidence is indicating that the intensity and frequency of extreme events is continuously changing also due to the induced effects of climate change (Milly et al. 2008; Change 2007). Thus, it is becoming of primary importance to account for non-stationarity in extremes and in this context, Non-stationary Extreme Value Analysis (NEVA) has recently emerged as a powerful approach, providing more reliable estimates of return levels and trends. In this context, Menéndez and Woodworth (2010) implemented a non-stationary extreme value approach to analyze changes in maxima of total elevations and surges over the 20th century. In a more recent work conducted by Boumis et al. (2023), a non-stationary extreme value theory was applied to model the behavior of extreme sea levels and quantify the evolution of annual maximum values using revised probabilistic sea-level rise projections. Other notable works are those presented by Baldan et al. (2022), Galiatsatou et al. (2021), and Mentaschi et al. (2016). Many other studies are listed and cited in the systematic literature review about applications of nonstationary extreme value analysis in the coastal environment provided by Radfar et al. (2023).

Among the methodological advances in this field, Cheng et al. (2014) introduced a practical Matlab package (called NEVA) for estimating stationary and especially non-stationary return levels. Several applications regarding the latter methodology can be found in the literature. Luo and Zhu (2019) analyzed extreme H_S in the SCS and modeled extreme H_S using the non-stationary GEV approach in the NEVA package. Similarly, Du et al. (2024) applied the NEVA framework to analyze the trends of 50- and 100-year wave heights. In a work published by Toimil et al. (2021), future projections of coastal erosion in northern Spain are investigated following the same non-stationary approach. Moreover, De Leo et al. (2021) analyzed the non-stationary behavior of annual maxima series of significant wave height and peak period in the Mediterranean Sea and Vanem (2015) applied a non-stationary analysis of extremes in an area of the North Atlantic Ocean.

The region investigated in this study comprises the majority of the South China Sea, as presented in the work performed by Bagnasco et al. (2025). The northwestern Pacific and the South China Sea are characterized by severe typhoon activity, leading to intense surface waves that pose a threat to both the economy of the area and to human lives (Y. Xu et al. 2017). The effects of typhoons have been extensively investigated in previous works. For instance, Y. Xu et al. (2017) performed simulations of three typhoon events in the South China Sea and then compared the generated typhoon waves with observations retrieved from wave buoys. A. Li et al. (2020) investigated the dependence of typhoon-induced storm surge and wave set-up on typhoon intensity and size in the South China Sea. Differently, Pham et al. (2019) characterized the spatio-temporal variations of extreme sea level and explored their long-term evolution along the low-lying, densely populated coasts of the South China Sea by applying a dynamic linear model for the generalized extreme value distribution.

In this study, a non-stationary analysis of annual significant wave height (H_S) extremes in the South China Sea is conducted, based on the hindcast data from Bagnasco et al. (2025) (1970-2022) and employing the framework established by Cheng et al. (2014). After identifying the presence of statistically significant trends by means of the MK test and computing the trend estimation based on the TS slope estimator, a non-stationary Generalized Extreme Value distribution (GEV) was applied to all the nodes of the hindcast mesh. In this way, it was possible to estimate the return levels for certain sets of return periods. The dataset hereby considered includes a series of typhoons that occurred in the numerical domain that were simulated with the parametric Holland model (G. Holland 2008). Since the non-stationary extreme value analysis was applied to annual extremes of H_S, incorporating typhoon events significantly improved the reliability for both trend estimates and return level calculations.

2.4 Multifractal detrended fluctuation analysis

Fractals are structures or processes that exhibit a statistically self-similar pattern across a wide range of spatial or temporal scales (Glenny et al. 1991). Fractal phenomena are widely observed throughout the natural world (e.g., the morphology of coastlines and river networks, and the branching structures of trees) and in physical and chemical systems (e.g., fractal noise and soil particle distributions). The fundamental objective of fractal analysis is to discover underlying order within complex, high-dimensional, and stochastic datasets by quantifying their fractal dimensions. This approach enables the modeling of dynamic environmental changes, thereby facilitating the optimization of distribution models. Consequently, fractal analysis has been formalized as a core methodology, contributing substantially to recent progress in data science.

The detrended fluctuation analysis method (hereby called DFA, (C.-K. Peng et al. 1994)) is a commonly adopted method to determine (mono-) fractal scaling properties and detect long-range correlations in non-stationary and noisy time series. It has been effectively applied across a wide range of disciplines, including DNA sequencing (C.-K. Peng et al. 1994; Buldyrev et al. 1998), neuron spiking (Blesić et al. 1999), long time weather records (Koscielny-Bunde et al. 1998; Talkner and Weber 2000), economics time series (Stanley and Mantegna 2000) and many more. A key reason for using the DFA method is to prevent the spurious detection of correlations that arise from non-stationarities in the time series.

A time series can exhibit a simple monofractal scaling behavior that can be described by a single scaling exponent. However, in some cases, it is possible to observe crossover time scales that separate regimes characterized by different scaling exponents (Kantelhardt et al. 2001; K. Hu et al. 2001). In other cases, the scaling behavior is more complex, and different scaling exponents are required for different segments of the time series, indicating the presence of multifractal properties that require the application of a multifractal analysis.

Generally, multifractality arises when a time series exhibits varying scaling behaviors across different interwoven fractal subsets, necessitating a spectrum of scaling exponents to fully capture its dynamics. Unlike monofractal systems, which are described by a single scaling exponent, multifractal systems display a range of scaling behaviors that reflect their complex, heterogeneous structure. This complexity often stems from the interplay of multiple underlying processes or the presence of long-range correlations with diverse statistical properties. Multifractal scaling is addressed by applying the multifractal detrended fluctuation analysis methodology (MF-DFA, (Kantelhardt et al. 2002)) which is an extension of the standard DFA method proposed by C.-K. Peng et al. (1994).

Despite its use across diverse fields, MF-DFA has also been applied to wave height time series even though there are only a few examples in the literature. G. Liu et al. (2019) applied this methodology to wave height data collected at Chaolian Island (China) between 1963 and 1989 to analyze their statistical characteristics, finding the presence of weak multifractality. In his thesis, López Avila (2020) investigated the significant wave height series of 52 wave measurements distributed in the western Mediterranean, between the period 2000-2005. López Avila (2020) concluded that the areas of greatest asymmetry were related to wind instability and wave height and persistence with an upward trend in wave height was observed in fetches influenced by strong northern winds. Later, H. Liu et al. (2023a) applied the MF-DFA method to analyze the hourly significant wave height records of a series of locations in the South China Sea. The signals were mostly characterized by dominant long-range correlations and showed a crossover point at around 12-13 days, therefore dividing the fluctuation of the significant wave height series into two parts. Moreover, H. Liu et al. (2023b) used the MF-DFA method to determine thresholds based on the changes of long-term correlations arising from the analysis of long-term significant wave height series in the South China Sea.

In this study, hourly values of significant wave heights spanning the period 1970-2022 were considered to perform the MF-DFA method. The data is retrieved from the two-way fully coupled wave-current hindcast provided by Bagnasco et al. (2025), which covers a large portion of the South China Sea (SCS). The objective is to analyze the behavior of significant wave height SCS as a whole, assessing potential short- and long-term correlations and determining the characteristic time scales prevalent in the region.

2.5 Mangroves as natural coastal wave attenuators

Mangroves are unique ecological systems located at the interface of land and sea along tropical and subtropical coastlines. Mangrove coastal vegetation displays life-history adaptations to overcome challenges associated with establishment in dynamic, mobile substrates influenced by currents and ocean waves, as well as high salinity (0–90 ppt) in waterlogged, anoxic sediments (Kamil et al. 2021). Nonetheless, mangroves contribute to coastal protection by reducing wave height and energy, serving as a natural barrier against incoming waves and thereby mitigating erosion (W. K. Lee et al. 2021). In recent decades, studies have highlighted the multifaceted benefits of mangrove trees, including: 1) preserving coastal biodiversity (Nehru and Balasubramanian 2018), 2) serving as critical nursery habitats for juvenile fish and crustaceans (Punchihewa and Krishnarajah 2019; Kamil et al. 2021), 3) offering coastal protection against flooding and erosion by dissipating wave energy (Chang et al. 2020), and 4) providing significant carbon sequestration to support climate regulation services (Bell-James et al. 2020).

Waves are attenuated through interactions with mangrove forests, driven by reduced water depths and resistance from mangrove roots, stems, and canopies in sufficiently deep water. Wave energy dissipation due to wave deformation depends on wave parameters (height, length, and period) and water depth, particularly in the intertidal zone's morphology, and can be numerically estimated when these parameters are known (Phan et al. 2019; Kamil et al. 2021).

Laboratory studies have elucidated the role of mangrove density and configuration in wave attenuation. Research by Hashim and Catherine (2013) demonstrated that denser mangrove forests achieve greater wave height reduction, with staggered and tandem arrangements showing minimal differences. Vegetated areas exhibited approximately twice the wave reduction compared to non-vegetated areas, with mangroves exerting higher drag forces that enhance energy dissipation. Similarly, Pasha and Tanaka (2016) and Pasha and Tanaka (2017) found that higher densities of emergent vegetation more effectively attenuates wave energy, with dissipation influenced by current direction, velocity, water depth, and vegetation density. Numerical modeling complemented these experiments to address limitations in generating stable current velocities.Kristiyanto, Armono, et al. (2013) explored the role of wave steepness, defined by wave height and period, in wave dissipation through laboratory and field studies, deriving the transmission coefficient (Kt) as the ratio of incident to transmitted wave height. Strusińska-Correia et al. (2013) investigated wave attenuation across varying mangrove forest widths under tsunami conditions, showing greater reduction in wider forests due to longer wave travel distances. However, laboratory mangrove models often simplify structures (e.g., using cylinders), omitting roots, branches, and canopies, which may affect the accuracy of wave attenuation estimates. Additionally, bed friction in wave flumes is typically ignored, despite the need to replicate the muddy substrates characteristic of mangrove environments.

Regarding numerical modeling, significant advancements have been made in understanding wave attenuation by mangroves, often represented as coastal vegetation. Iimura and Tanaka (2012) used Boussinesq-type equations with porosity and resistance terms to model tsunami energy reduction, showing greater water level and velocity reductions with increased vegetation density. Validation experiments indicated a 10% error, highlighting the need for improved modeling of vegetation boundaries and back-row effects. Similarly, Teh et al. (2009) incorporated the Morison equation into the TUNA-RP model, using mangrove geometry data from Penang, Malaysia, to demonstrate that wave height and velocity reduction ratios vary with wave and mangrove parameters. Adytia and Husrin (2019) refined this approach by adding bottom roughness dissipation terms to model nonlinear tsunami wave attenuation, relating required mangrove width to wavelength for specific dissipation rates. For short-period waves, Van Rooijen et al. (2015) extended the XBeach model with formulations from Mendez and Losada (2004) to quantify attenuation of short waves, infragravity waves, and mean flow. Z. Hu et al. (2014) modeled vegetation drag in tidal currents, finding wave attenuation of 96–97% during high tides and 85–90% during low tides, with mangrove canopies and roots playing key roles in high and low tides, respectively.

Abdullah et al. (2019) used the Mansard-Funke method and spectral analysis to assess wave amplitude, period, and mangrove density, noting higher energy dissipation in denser mangroves under submerged conditions. Recent studies have shifted toward modeling mangroves as flexible vegetation, with the XBeach model adapted to account for dynamic vegetation motion, improving predictions of wave dissipation (Yin et al. 2021; Yin et al. 2022; Ma et al. 2024).

The area investigated in this work concerns the Mai Po Nature Reserve, located in the northwestern part of Hong Kong near the Inner Deep Bay. The Mai Po Nature Reserve has been the subject of extensive research, providing a foundation for understanding its ecological and wave attenuation functions.

Studies indicate that wave height reductions in such environments can reach up to 90% in some cases (Mclvor et al. 2012; Rasmeemasmuang and Sasaki 2015). Despite hypothetical predictions of wave and storm surge attenuation in the Mai Po region, field measurements of wave activity and water levels remain scarce, underscoring the need for this project's field-based data collection (Wikramanayake et al. 2020; De Dominicis et al. 2023). Key publications provide foundational data on Mai Po's mangrove ecosystem. Early work by Khan (1999) documented the structure and composition of Mai Po's seaward mangrove forest, detailing ground elevation and seedling density. Owen and R. Lee (2004) examined sediment dynamics in Deep Bay, highlighting human impacts on sedimentation processes relevant to the coastal environment of Mai Po. Y. Chen and Wai (2005) modeled wave-current interactions in Deep Bay, demonstrating that wind significantly influences wave propagation and increases suspended sediment concentrations by up to 20 times when wave and current magnitudes are comparable. Wave attenuation studies provide critical insights for this research. Mclvor et al. (2012) reported wave height reductions of 13–55% over 100 m of mangroves, with greater reductions associated with higher mangrove density, using models like SWAN (Simulating Waves Nearshore). Similarly, Rasmeemasmuang and Sasaki (2015) found wave reductions of 20–90% in mangrove forests, influenced by hydrodynamic, botanical, and geological factors (Rasmeemasmuang and Sasaki 2015). Garzon et al. (2019) investigated Spartina saltmarshes in Chesapeake Bay, noting that wave attenuation (50–70% for wave heights of 1.55 m and 0.8 m, respectively, at 250 m from the marsh edge) depends on water depth, plant height, and current directions. Wikramanayake et al. (2020) applied the Sea Level Affecting Marshes Model to assess habitat impacts under sea level rise scenarios (1.5 m and 2.0 m) for 2050, 2075, and 2100, indicating potential mangrove and tidal flat impacts by 2100 under various accretion rates.

Advanced remote sensing studies (Q. Li et al. 2019; Q. Li et al. 2021) utilized WorldView-3 and LiDAR data to classify seven mangrove species in Mai Po and estimate biophysical parameters such as canopy height, cover, stratification, leaf area index, and biomass, which may correlate with drag coefficients and wave attenuation. Best et al. (2022) quantified wave attenuation in Guyana's mangrove belt, reporting rates of 0.002–0.0032 m^{-1} within mangroves compared to 0.0003–0.0004 m^{-1} on bare mudflats, with attenuation positively correlated to vegetation density. The wave height reduction rate, α (m^{-1}), is calculated as:

$$\alpha = \frac{\Delta H_{s,0}}{H_{s,0}\Delta x}, \tag{2.1}$$

where $\Delta H_{s,0}$ is the wave height reduction (m), $H_{s,0}$ is the initial wave height (m), and Δx is the distance in the direction of wave propagation (m) (Best et al. 2022). Finally, De Dominicis et al. (2023) highlighted the effectiveness of mangroves in attenuating extreme water levels in the Pearl River Delta, emphasizing the role of vegetation patch width and drag, though focused on storm surges rather than short-period wind waves. These studies collectively underscore the importance of field measurements to validate wave attenuation models in Mai Po, addressing the gap in empirical data and enhancing the understanding of mangrove-mudflat systems as natural coastal defenses.

Chapter 3

Methodology

This study is based on a 2-dimensional, 2-way coupled model, combining the Semi-implicit Cross Scale Hydroscience Integrated System Model SCHISM and the third-generation spectral Wind Wave Model WWMIII. The 2-way coupling implies that the current velocities and sea water levels are provided to the wave model and the latter computes the wind stresses that are then handed back to SCHISM. More details and formulations about the two models are provided in the following Sections.

3.1 SCHISM: model framework and governing equations

SCHISM (Semi-implicit Cross-scale Hydroscience Integrated System Model) is an open-source community-supported modeling system based on unstructured grids, designed for seamless simulation of 3D baroclinic circulation across creek-lake-river-estuary-shelf-ocean scales that was implemented by Dr. Zhang in 2016 (Y. J.

Zhang et al. 2016). This unstructured-grid model is the upgrade of an existing model (SELFE) (Y. Zhang and Baptista 2008) which is the Semi-implicit Eulerian-Lagrangian Finite-element model for cross-scale ocean circulation. As reported in the SCHISM v5.9 user manual, the main characteristics of the model can be listed as follows:

- 1) Finite-element/finite-volume formulation
- 2) Unstructured mixed triangular/quadrangular grid in the horizontal dimension
- 3) Hybrid SZ coordinates or new LSC^2 in the vertical dimension
- 4) Polymorphism: as ingle grid can mimic 1D/2DV/2DH/3D configurations
- 5) Semi-implicit time stepping (no mode splitting): no CFL stability constraints, which results in higher numerical efficiency
- 6) Robust matrix solver
- 7) Higher-order Eulerian-Lagrangian treatment of momentum advection
- 8) Natural treatment of wetting and drying suitable for inundation studies
- 9) Mass conservative and monotonicity-enforced transport: TVD^2
- 10) No bathymetry smoothing necessary
- 11) Very tolerant of bad-quality meshes in the non-eddying regime

SCHISM been successfully used in several applications to model tsunami hazards, short wave-current interactions, storm surge, sediment transport, oil spills, 3D baroclinic cross-scale lake-river-estuary-plum-shelf-ocean circulations, ecology, biogeochemistry and water quality. With the hydrostatic and Boussinesq approximations, the Navier-Stokes equations can be written as shown below.

$$\text{Momentum equation}: \frac{Du}{Dt} = \mathbf{f} - g\nabla\eta + \mathbf{m}_z - \alpha|\mathbf{u}|\mathbf{u}L(x, y, z), \tag{3.1}$$

$$\mathbf{f} = f(v, -u) - \frac{g}{\rho_0}\int_z^\eta \nabla\rho\, d\zeta - \frac{\nabla p_a}{\rho_0} + \alpha g\nabla\psi + \mathbf{F}_m + \mathit{other}, \tag{3.2}$$

Continuity equations in 3D and 2D depth-averaged forms:

$$\boldsymbol{\nabla}\cdot\mathbf{u} + \frac{\partial w}{\partial z} = 0, \tag{3.3}$$

$$\frac{\partial\eta}{\partial t} + \nabla\cdot\int_{-h}^{\eta}\mathbf{u}\,\mathrm{d}z = 0, \tag{3.4}$$

$$\text{Transport equation}: \frac{\partial C}{\partial t} + \nabla\cdot(\mathbf{u}C) = \frac{\partial}{\partial z}\left(k\frac{\partial C}{\partial z}\right) + F_h, \tag{3.5}$$

$$\text{Equation of state}: \rho = \rho(S, T, p), \tag{3.6}$$

Where:

- $\mathbf{u}(x, y, z, t) = (u, v)$: Horizontal velocity components in $\mathrm{m\,s^{-1}}$
- $w(x, y, z, t)$: Vertical velocity in $\mathrm{m\,s^{-1}}$
- p: Hydrostatic pressure in Pa
- p_A: Atmospheric pressure reduced to MSL in Pa
- ρ, ρ_0: Water density and reference density in $\mathrm{kg\,m^{-3}}$
- $\mathbf{f}$: Other forcing terms in momentum equations (baroclinic gradient, horizontal

viscosity, Coriolis, earth tidal potential, atmospheric pressure, radiation stress) - typically treated explicitly in numerical formulation

- $g = 9.81\,\mathrm{m\,s^{-2}}$: Acceleration of gravity
- C: Tracer concentration (salinity, temperature, sediment, etc.) in relevant units
- ν: Vertical eddy viscosity in $\mathrm{m^2\,s^{-1}}$
- k: Vertical eddy diffusivity for tracers in $\mathrm{m^2\,s^{-1}}$
- $\mathbf{F}_m$: Horizontal viscosity in $\mathrm{m^2\,s^{-1}}$
- F_h: Horizontal diffusion and mass sources/sinks in $\mathrm{m^2\,s^{-1}}$

and

$\nabla = \left(\frac{\partial}{\partial x}, \frac{\partial}{\partial y}\right)$	Horizontal gradient operator
$\frac{D}{Dt} = \frac{\partial}{\partial t} + \mathbf{u} \cdot \nabla$	Material derivative
(x, y)	Horizontal Cartesian coordinates
z	Vertical coordinate (positive upward)
t	Time
$\eta(x, y, t)$	Free-surface elevation in m
$h(x, y)$	Bathymetric depth (from fixed datum) in m

The momentum equation (as shown in Equations 3.1 and 3.2) can also account for the effects of vegetation. α(x,y) is a vegetation parameter that represents the vegetation-related density variable, expressed in $\mathrm{m^{-1}}$ and defined as:

$$\alpha(x, y) = D_\nu N_\nu \frac{C_{D\nu}}{2}, \tag{3.7}$$

where:

D_ν is the stem diameter

N_ν is the vegetation density (stems per m^2)

$C_{D\nu}$ is the bulk form drag coefficient

The selection of $C_{D\nu}$ is the object of several studies with values that vary between 0 and 3 (Tanino and Nepf 2008; Nepf and Vivoni 2000), and is validated against reported laboratory study values. The underlying assumption in the SCHISM model is to treat the vegetation elements as solid cylinders. Flexibility of the stems or sheltering effects within a cluster of vegetation can lead to one or two orders of reduction in the drag forces, and Gaylord et al. (2008) showed that the drag coefficient is also species-dependent. Since SCHISM allows 'polymorphism' with mixed 2D and 3D cells in a single grid (Y. J. Zhang et al. 2016), the vertical eddy viscosity term can be expressed in different forms as shown here:

$$m_z = \begin{cases} \frac{\partial}{\partial z}\left(\nu \frac{\partial u}{\partial z}\right) & \text{for 3D cells} \\ \dfrac{\tau_w - \chi_u}{H} & \text{for 2D cells} \end{cases} \tag{3.8}$$

and the vegetation term:

$$L(x, y, z) = \begin{cases} \mathcal{H}(z_v - z), & \text{3D} \\ 1, & \text{2D} \end{cases} \tag{3.9}$$

where ν is the eddy viscosity, τ_w is the surface wind stress, $H = h + \eta$ is the total water depth (with h being the resting depth measured from a fixed datum),

$\chi = C_D|\mathbf{u}|$ is the bottom friction term, C_D is the bottom drag coefficient and $\mathcal{H}$ is the Heaviside step function:

$$\mathcal{H}(x) = \begin{cases} 1, & x \geq 0 \\ 0, & x < 0 \end{cases} \tag{3.10}$$

Where z_ν is the z-coordinate of the canopy and **u** denotes the depth-averaged velocity in a 2D region.

3.1.1 Boundary conditions

The differential equations in Section 3.1 need Initial Conditions (ICs) and Boundary Conditions (BCs). Typically, all state variables (η,**u**, C) are specified at time t = 0 as ICs and these are also specified at all open lateral boundary segments (open ocean, rivers, etc.). However, not all variables need to be specified at all boundary segments. The vertical BCs for momentum equation, continuity equation, transport equation, and equation of state are described in detail below as these impact the numerical scheme. Note that these only apply to 3D cells; for 2D cells, the momentum equation (see Equation 3.8) has considered the BCs. At the sea surface, SCHISM enforces the balance between the internal Reynolds stress and the applied shear stress:

$$\nu \frac{\partial \mathbf{u}}{\partial z} = \boldsymbol{\tau}_w \quad \text{at} \quad z = \eta \tag{3.11}$$

where the wind surface stress τ_w can be parametrized using the approach of Zeng et al. (1998) or the simpler one introduced by Pond and Pickard (1983). If the wind model is invoked, the stress can also be calculated from the wave model. Since the bottom boundary layer is usually not well resolved in ocean models, the no-slip condition at the sea or river bottom (u = w = 0) is replaced by a balance between the internal Reynolds stress and the bottom frictional stress:

$$\nu \frac{\partial \mathbf{u}}{\partial z} = \boldsymbol{\tau}_b \quad \text{at} \quad z = -h \tag{3.12}$$

The specific form of the bottom stress τ_b depends on the type of boundary layer used. In case of turbulent boundary layer (Blumberg and Mellor 1987), given its prevalent usage in ocean modeling, the bottom stress is defined as:

$$\boldsymbol{\tau}_b = C_D |\mathbf{u}_b| \mathbf{u}_b \equiv \chi \mathbf{u}_b \tag{3.13}$$

The velocity profile in the interior of the bottom boundary layer obeys the following logarithmic law:

$$\mathbf{u} = \frac{\ln\left(\frac{z+h}{z_0}\right)}{\ln\left(\frac{\delta_b}{z_0}\right)} \mathbf{u}_b, \quad -h + z_0 \leq z \leq \delta_b - h \tag{3.14}$$

which is smoothly matched to the exterior flow at the top of the boundary layer. In the previous equation (Equation 3.14), δ_b is the thickness of the bottom computational cell (assuming that the bottom is sufficiently resolved in SCHISM that the bottom cell is inside the boundary layer), z_0 is the bottom roughness, and u_b is the velocity measured at the top of the bottom computational cell. Therefore, the Reynolds stress inside the boundary layer is computed as:

$$\nu \frac{\partial \mathbf{u}}{\partial z} = \frac{\nu}{(z+h) \ln\left(\frac{\delta_b}{z_0}\right)} \mathbf{u}_b \tag{3.15}$$

Utilized the turbuluence closure theory discussed below, it is shown that the Reynolds stress is constant inside the boundary layer:

$$\nu \frac{\partial \mathbf{u}}{\partial z} = \frac{k_0}{\ln\left(\frac{\delta_b}{z_0}\right)} C_D^{1/2} |\mathbf{u}_b| \mathbf{u}_b, \quad z_0 - h \leq z \leq \delta_b - h \tag{3.16}$$

Equation 3.16 shows that the vertical viscosity term in the momentum equation vanishes inside the boundary layer. Moreover, the drag coefficient can then be calculated as discussed in Blumberg and Mellor (1987):

$$C_D = \left(\frac{1}{k_0} \ln\left(\frac{\delta_b}{z_0}\right) \right)^{-2} \tag{3.17}$$

3.2 WWMIII: model framework and governing equations

As anticipated in Section 2.1, WWMIII (Wind Wave Model III) is an unstructured-grid, state-of-the-art, third-generation spectral wind wave model that can be coupled to SCHISM in order to simulate the sea state in coastal and ocean waters. WWMIII is the upgraded version of WWMII, the details of which are well explained in Roland et al. (2008) and Roland et al. (2009). The theory behind the model and the equations that will be hereby shown are presented and discussed in the thesis written by Roland (Roland et al. 2008).

The main equation that needs to be solved is the Wave Action Equation (WAE):

$$\frac{\partial N}{\partial t} + \nabla_{\boldsymbol{x}}(\dot{\boldsymbol{X}} N) + \frac{\partial}{\partial \sigma}(\dot{\theta} N) + \frac{\partial}{\partial \theta}(\dot{\sigma} N) = S_{\text{tot}} \tag{3.18}$$

Where the wave action density spectrum (N) is defined as:

$$N(t, \mathbf{X}, \sigma, \theta) = \frac{E(t, \mathbf{X}, \sigma, \theta)}{\sigma} \tag{3.19}$$

And

$\frac{\partial N}{\partial t}$	represents the change in time of the wave action density spectrum
$\nabla_{\boldsymbol{x}}(\dot{\boldsymbol{X}}N)$	represents the advection in horizontal space
$\frac{\partial}{\partial \sigma}(\dot{\theta}N) + \frac{\partial}{\partial \theta}(\dot{\sigma}N)$	represents the advection in spectral space
S_{tot}	represents the sum of all the source terms

Specifically, the source function S_{tot} accounts for several contributions that govern the local evolution of the wave spectrum:

$$\frac{dN}{dt} = \underbrace{S_{\text{in}}}_{\text{Wind input}} + \underbrace{S_{\text{nl4}}}_{\text{Quadruplets}} + \underbrace{S_{\text{ds}}}_{\text{Dissipation}} + \underbrace{S_{\text{nl3}}}_{\text{Triads}} + \underbrace{S_{\text{br}}}_{\text{Breaking}} + \underbrace{S_{\text{bf}}}_{\text{Friction}} + \underbrace{S_{\text{bg}}}_{\text{Scattering}} + \cdots \tag{3.20}$$

As shown in Equation 3.20, S_{in} is the energy input caused by the wind, S_{nl4} and S_{nl3} are the source terms related to nonlinear interactions in deep and shallow water, S_{ds} and S_{br} are the energy dissipation terms in deep and shallow water due to whitecapping and wave breaking, S_{bf} is the energy dissipation due to bottom friction and S_{bg} is the energy dissipation induced by interactions between the waves and the sea floor (also called Bragg-Scattering). Most of these processes are formulated as semi-empirical equation, except for the Boltzmann integral, describing the nonlinear energy transfer in deep water (S_{nl4}), which can be accurately estimated for any arbitrary wave spectrum. In Equation 3.19, E is the variance density related to a certain spectral bin (dθ, dσ) as function of time and the spatial coordinate vector **X**. The advection velocities in the different phase spaces were originally derived by Keller (1958):

$$\dot{\boldsymbol{X}} = \boldsymbol{c}_x = \frac{d\boldsymbol{X}}{dt} = \frac{d\omega}{d\boldsymbol{k}} = \boldsymbol{c}_g + \boldsymbol{U}_A \tag{3.21}$$

$$\dot{\theta} = c_\theta = \frac{1}{k}\frac{\partial \sigma}{\partial d}\frac{\partial d}{\partial m} + \boldsymbol{k}\frac{\partial \boldsymbol{U}_A}{\partial s} \tag{3.22}$$

$$\dot{\sigma} = c_\sigma = \frac{\partial \sigma}{\partial d}\left(\frac{\partial d}{\partial t} + \boldsymbol{U}_A \cdot \nabla_{\boldsymbol{x}} d\right) - c_g k \frac{\partial \boldsymbol{U}_A}{\partial s} \tag{3.23}$$

In the last three equations, s represents the coordinate in wave propagation and m the coordinate perpendicular to it. In case of no current, the advection velocity in σ-direction vanishes and in deep-water scenarios with the absence of currents, the component in θ-space becomes zero. The nonlinear evolution of waves is governed by the source term S_{tot}, which in deep water conditions is typically decomposed into three fundamental components: a wave-wave interaction term, a wind-induced growth term, and a dissipation term. A key distinguishing feature of third-generation wave models compared to their first- and second-generation predecessors lies in their explicit, albeit approximate, treatment of nonlinear wave-wave interactions through the Discrete Interaction Approximation (DIA) (S. Hasselmann 1985). This approach provides a more physically consistent representation of spectral energy mechanisms, representing a significant advancement in spectral wave modeling capabilities. Regarding wave growth mechanisms, most spectral wave models adopt the theoretical framework proposed by Miles (1957). A notable exception is the formulation developed by Tolman and Chalikov (1996), which builds upon the earlier work of Chalikov and Belevich (1993) to provide an alternative parametrization of wind-wave generation. Wave energy dissipation remains the least understood component of wave dynamics, with current representations relying primarily on semi-empirical formulations. These include the whitecapping dissipation models (K. Hasselmann (1974), as extended by Komen et al. (1984) and P. Janssen et al. (2005)) and the quasi-saturation approach proposed by Phillips (1985).While recent studies incorporating field measurements and laboratory experiments (I. R. Young and Babanin 2006; Ardhuin et al. 2008) have advanced our physical understanding of dissipation processes, model parametrizations still require substantial a posteriori calibration to achieve satisfactory agreement with observations. The treatment of dissipation terms is intrinsically linked to wind input parametrizations, as both processes are typically developed and calibrated in tandem. This interdependence raises fundamental questions about the conventional separation of source terms into distinct growth and dissipation components. Ardhuin et al. (2008), for instance, proposed an alternative framework that distinguishes between ocean-atmosphere and ocean-ocean interactions, grouping wind-forced swell dissipation together with exponential growth terms. This approach highlights the complex interplay between different energy exchange processes in the coupled air-sea system. The WavewatchIII (WWIII) model has been implemented with two distinct sets of source term parametrizations: (1) the well-established formulation by Tolman and Chalikov (1996) and (2) the more recent physics package by Ardhuin et al. (2010), incorporating the J. Bidlot et al. (2005) parametrization along with the ACC350 formulation documented in the WWIII user manual. Similarly, the WWMIII model supports source terms parametrizations based on the series of developments by Ardhuin et al. (2009), Ardhuin et al. (2010), and Ardhuin et al. (2011). These implementations utilize a modified version of the WAM Cycle 4 wind input formulation, where the positive part of the wind input is retained while introducing an ad hoc reduction of the friction velocity. This adjustment serves to key purposes: first, it establishes balance with a saturation-based dissipation formulation that incorporates various options for cumulative effects; second, it effectively reduces the drag coefficient under high wind conditions. The modification specifically targets the wind input reduction for high-frequency wave components under strong wind forcing, thereby improving the model's performance across extreme wind regimes.

3.2.1 Holland model parametrization for typhoons

As mentioned in the previous Sections, typhoons and extreme events were included in the analysis and accurately simulated with the Hurricane Pressure-Wind Model (G. Holland 2008). More specifically, the tropical cyclone forcing in SCHISM was provided by the PaHM parametric modeling system which was developed by NOAA's Office of Coast Survey Storm Surge Modeling Team. The parametric models that can be adopted are the Generalized Asymmetric Vortex Holland Model (Gao et al. 2013; Gao 2018) and the Holland model (G. Holland 2008).

The latter formulation was therefore chosen to characterize the wind and pressure fields related to a series of typhoons and extreme events that were observed during the years covered by the wave hindcast (1970-2022). Extreme events that occurred outside the numerical domain were excluded from the analysis. Typhoon data were obtained from the International Best Track Archive for Climate Stewardship (IBTrACS; Knapp et al. (2010)), with only complete records retained for analysis. The data can be retrieved from the following website: (https://www.ncei.noaa.gov/products/international-best-track-archive). Events with missing critical parameters (e.g., maximum radius or peak wind speed) were systematically excluded to maintain data quality. In this way, a total of 32 events were included in the simulations as shown below:

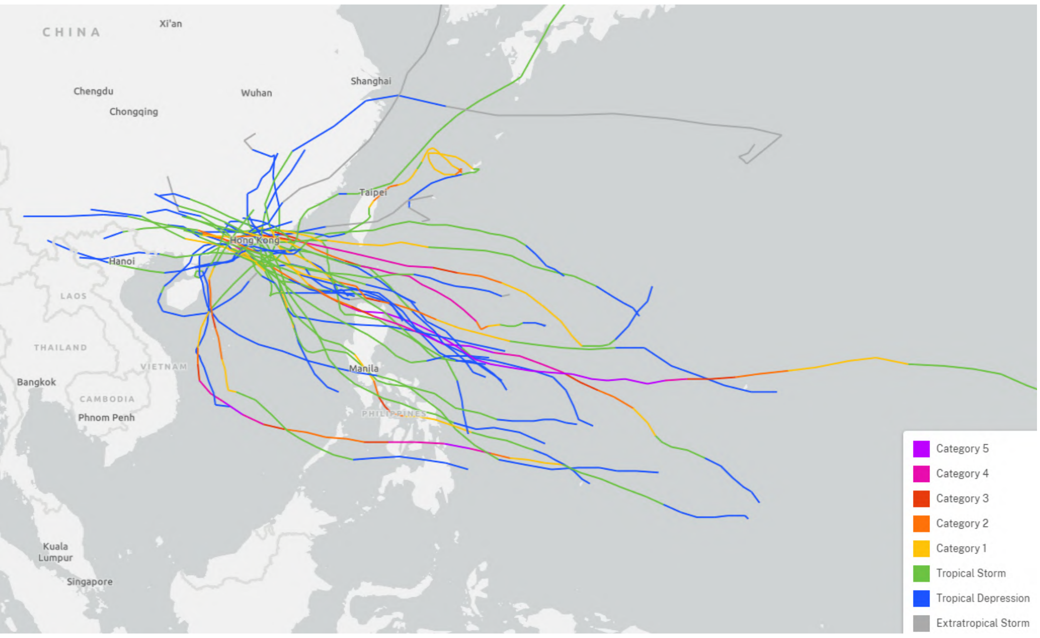

Figure 3.1: Typhoon tracks analyzed in this work, source International Best Track Archive for Climate Stewardship (IBtrACS).

The pressure field is characterized by the following equation:

$$P(r) = P_c + (P_n - P_c)\, e^{-\left(\frac{R_{\text{max}}}{r}\right)^B} \tag{3.24}$$

where $P(r)$ is the pressure at radius r, P_c is the central pressure, P_n is the ambient pressure (assumed constant at 1013.25 mbar), R_{max} is the radius of maximum winds and B is the Holland parameter: it defines the shape of the pressure profile and is calculated according to this relationship:

$$B = \frac{\rho_{\text{air}}\ e\ V_{\max}^2}{P_n - P_c} \tag{3.25}$$

where ρ_{air} is the density of air. The wind speed field $V_g(r)$ is calculated according to the following:

$$V_g(r) = \sqrt{V_{\max}^2 \left(\frac{R_{\max}}{r}\right)^B e^{1-\left(\frac{R_{\max}}{r}\right)^B} + \left(\frac{rf}{2}\right)^2} - \frac{rf}{2} \tag{3.26}$$

where V^2max is the maximum wind speed and f is the Coriolis parameter.

3.3 Numerical model setup

The domain considered in this paper covers the majority of the SCS, spanning from longitudes of approximately 106° E to 123° E and from latitudes of approximately 3° N to 28° N. Figure 3.2 shows the part of the South China Sea considered for the numerical simulations. A particular focus was dedicated to the Great Bay Area (GBA) and the coasts along the Guangdong Province (China).

This study is based on a 2-dimensional, two-way coupled model, combining SCHISM and the third-generation spectral Wind Wave Model WWMIII. In this configuration, SCHISM applies the 2D depth-integrated barotropic equations. The two-way coupling implies that the current velocities and sea water levels are provided to the wave model and the latter computes the wind stresses that are then handed back to SCHISM according to the parametrization based on the wave age of Donelan et al. (1993). The structure of SCHISM is derived from the origi-

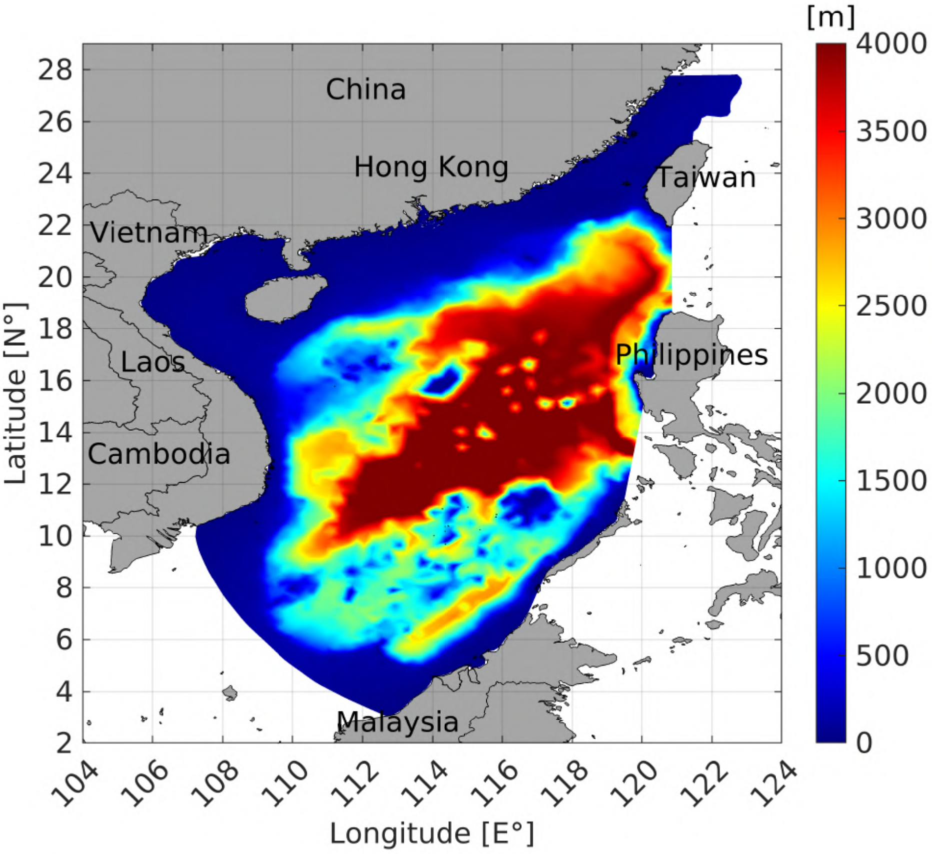

Figure 3.2: Portion of the South China Sea investigated with the bathymetry contours.

nal Semi-implicit Eulerian-Lagrangian Finite-Element model (SELFE) (Y. Zhang and Baptista 2008; Y. J. Zhang et al. 2016). The integration time steps implemented in the analysis are 100 s for SCHISM and 600 s for WWMIII: this implies that the two models exchange information every 6 time steps. This choice was made after testing different model time steps in order to minimize possible numerical dispersion errors and/or excessive truncation errors. Being SCHISM a semi-implicit model itself that applies no mode splitting, the fulfillment of the CFL constraint is more easily met and this leads to greater numerical stability. As stressed by Huang et al. (2022), the typical integration time steps used in these types of field applications usually vary between 100 s and 200 s. The unstructured mesh covers the majority of the South China Sea (SCS) and was generated with the aid of the 13.1 version of SMS (Surface-water Modeling System by Aquaveo, https://www.xmswiki.com/wiki/SMS:SMS). Both SCHISM and WWMIII share the same unstructured mesh which comprises 15523 nodes and 29039 triangular elements. The lowest mesh resolution is circa 0.008° around the GBA and reaches a size of 0.35° in the open ocean. Several unstructured meshes were generated and tested in order to find the optimal mesh that provides sufficient resolution and that contains the computational time. The bathymetry of the whole domain was extracted from the 2022 General Bathymetric Chart of the Oceans (GEBCO) dataset (Weatherall et al. 2015) with a resolution of 15 arc-second intervals and then merged with a more refined dataset of 2020 water depths related to Hong Kong only and provided by the Hong Kong Hydrographic Office (HO) of the Marine Department (https://www.hydro.gov.hk/eng/). Subsequently, the bathymetry was interpolated on the unstructured mesh. Since the unstructured mesh size becomes coarser offshore and far from the GBA region, most of the islands were neglected in the mesh generation, including Paracel Islands. This is because, in these cases, the mesh size is larger than the dimension of the islands themselves.

The bottom friction was evaluated considering a minimum boundary layer thickness of 0.2 m and a roughness length equal to $5.78 \cdot 10^{-6}$m and constant for all the nodes. The latter corresponds to a Manning coefficient of about 0.012 s/m$^{1/3}$ which was also applied by J. Wang and P. L.-F. Liu (2021) for a similar application in the SCS. The atmospheric forcing (sea level pressure and wind velocities) and the tidal oscillations at the open boundaries start from a zero value and then have a warm-up time equal to 365 days in order to provide enough time for the oceanic conditions to settle properly in such a large domain. The wetting and drying mechanism was considered active and accounted for a minimum water depth of 0.01 m. The surface stress was calculated according to the parameters of Donelan et al. (1993), whose formulation is based on the wave age. The discretization of the spectral domain was performed regrouping the frequencies into 36 bins (lower limit of 0.04 Hz and higher limit of 1 Hz) and the directions into 24 bins with minimum and maximum directions of respectively 0° and 360°. The wave boundary layer was activated and treated as explained by Soulsby (1997). WWMIII solves the wave action equation and accounts for different contributions and phenomena, mainly referred to as source terms, that cause the energy content to be rearranged within the spectrum. The work done in this paper considers non-linear interactions (DIA approximation, S. Hasselmann (1985)), wind-induced energy input and wave energy dissipation in deep waters (whitecapping) according to the ST4 parametrization (Ardhuin et al. 2010). The wave model incorporates the JONSWAP bottom friction parametrization (K. Hasselmann et al. 1973) with a bottom friction coefficient equal to 0.067 m^2s^{-3} (Bouws and Komen 1983) and shallow water wave breaking characterized by a constant gamma criterion. The wave breaking formulation is based on the work of Battjes and J. Janssen (1978) and the model also incorporates the effects of triad 3-wave interactions (LTA Lumped Triad Approximation, Eldeberky (1997)).

The numerical simulations aimed at generating a 53-year wave hindcast covering the time period between the years 1970 and 2022. The outputs of both SCHISM and WWMIII are generated and saved hourly and comprise the main variables used for the purpose of this paper: significant wave height (H_S), peak wave period (T_p), mean wave direction (D_m) and water level (h).

3.3.1 Input forcings

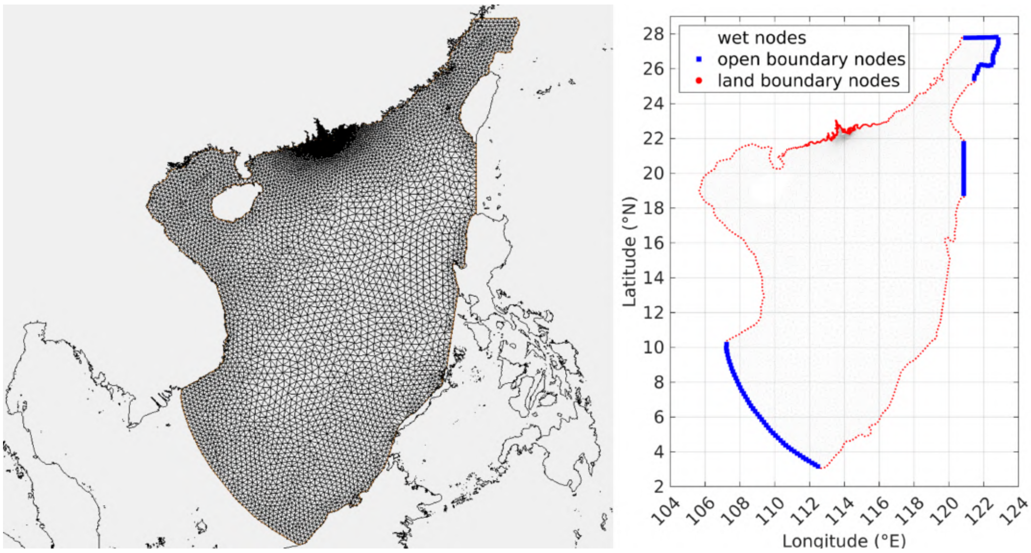

Figure 3.3: Left panel: mesh used for the numerical simulations. Right panel: Details of the unstructured mesh and boundaries of the numerical domain.

The boundary conditions applied at the open boundary nodes of the unstructured mesh (blue nodes in Figure 3.3, right panel) consist of the 8 major harmonic components of the tides (M2, S2, N2, K2, K1, O1, Q1, P1) and were extracted from the FES2014 package (Carrere et al. 2015). The boundary nodes that connect Malaysia to the region above Manila in the Philippines were considered as land nodes since the portion of water that they exclude is enclosed by various islands and therefore not essential for wind waves generation. Regarding the wave conditions at the open boundary, no conditions were applied. It was shown in Chapter 9, Section 9, that the final results were not impacted by the choice of open boundary condition, including the imposition of time signals from available hindcast datasets. The main meteorological forcing employed are hourly data of sea level pressures and wind velocities defined over a 0.25° x 0.25° grid obtained from the fifth generation ECMWF reanalysis (ERA5) (Hersbach et al. 2023).

To improve the quality of the forcing wind data ERA5 wind velocities were compared to the IFREMER blended velocities (https://cerweb.ifremer.fr/datarmor/products/satellite/l4/multi-sensor/ifr-l4-ewsb-blendedwind-glo-025-6h-rep/data/) that were estimated from reprocessed and near real-time scatterometer and radiometer data jointly with ERA Interim wind re-analyses. Wind velocities are provided on a 0.25° x 0.25° global grid for each synoptic time (00:00; 06:00; 12:00; 18:00 UTC). Detailed descriptions of the data, methods and accuracy issues can be found in Bentamy and Fillon (2012), Bentamy et al. (2017), Bentamy et al. (2019), and Desbiolles et al. (2017). The comparison resulted in a bias correction of the ERA5 wind field. This correction was necessary because wind velocities derived from reanalysis products often exhibit bias under high wind conditions (extreme scenarios). By comparing these values with satellite radiometer observations, a more accurate representation of the meteorological forcing can be achieved (Campos et al. 2022; Benetazzo et al. 2022; Elshinnawy et al. 2024). A similar approach was also adopted by Zhai et al. (2023), who performed a bias-correction of the ERA5 wind field in the SCS considering wind measurements from 15 buoys. The study revealed that ERA5 winds can underestimate or overestimate the wind intensities. In a more recent work conducted by Elshinnawy et al. (2024), a new parametrization of the wind source terms in WAVEWATCH III has been proposed in order to correct the ERA5 wind speed bias that is found to occur for significant wave heights larger than 7.5 m.

For the matter of this work, in order to correct the bias, the analysis was preprocessed as follows. The 10-meter northward and eastward wind velocity components provided by the ERA5 dataset span from 1970 to 2022 and are defined hourly on a regular grid of 0.25°. In contrast, the IFREMER dataset contains wind velocity components from 1992 to 2020 that are available every 6 hours on a different regular grid of 0.25°. Although the locations of the two datasets did not align, a series of pre-processing steps were undertaken to ensure consistent spatiotemporal resolution between them. First, a downsampling process was applied to the ERA5 velocities in order to convert them to a 6-hourly interval. Additionally, a cubic spatial interpolation was performed in order to transfer the ERA5 data onto the IFREMER grid. The velocities occurring at each grid node, for a specific year, were grouped into bins of 1 m/s and the 6-hourly biases were divided into 0.10 m/s bins. Subsequently, a probability density function was computed enabling the assignment of velocities falling within a specific bin to the most probable 6-hourly bias bin value for that particular year. This final operation yielded a 6-hourly map representing the most likely biases for both the wind velocity components. To further fine-tune the biases, an additional cubic spatial interpolation was performed so that hourly maps of biases were generated. These maps were then added to the original ERA5 wind field, resulting in a corrected wind field suitable for utilization in the numerical simulations.

3.4 Model validations and statistical performance indexes

The validation of the model required at first the tuning of the integration time steps for both the SCHISM and the WWMIII models as well as the choice of the unstructured mesh size. The overall quality of the results and the performance of the model were quantified through the comparison with observations provided by physical stations (in terms of H_S, T_p, D_m, h) and satellite measurements (in terms of H_S).

3.4.1 Statistical analysis

The validation was carried out by evaluating a series of statistical indicators that are commonly used in literature (Shi et al. 2019; Mentaschi et al. 2015) for assessing the accuracy of the results such as the Correlation Coefficient CC, centered Root Mean Square Difference $RMSD$ and the Standard deviation σ. These three fundamental indicators can be grouped within the Taylor diagram (Taylor 2001), which provides an effective graphical representation of the results. As also mentioned by Mentaschi et al. (2015) it is advised not to rely on the more traditional error indicators (such as the Normalized Root Mean Square Error $NRMSE$ and the Scatter Index SI); instead, a more accurate evaluation of the errors can be performed with the exploitation of the symmetrically normalized root mean square error HH (Hanna and Heinold 1985; Mentaschi et al. 2013a). Mentaschi et al. (2013a) pointed out that, in some circumstances, simulations that exhibit negative biases tend to be characterized by smaller $RMSE$ values: this implies that, paradoxically, these simulations perform better that simulations with no biases. For these reasons, the statistical indicators considered in the validation for scalar integrated variables (H_S and T_p) are:

$$\text{Correlation Coefficient} \qquad CC = \frac{\sum(S_i - \bar{S}) \cdot (O_i - \bar{O})}{\sigma_S \cdot \sigma_O \cdot N} \tag{3.27}$$

$$\text{Normalized Bias} \qquad NBI = \frac{\sum(S_i - O_i)}{\sum O_i} \times 100 \tag{3.28}$$

$$\text{Hanna and Heinold indicator} \qquad HH = \sqrt{\frac{\sum(S_i - O_i)^2}{\sum(S_i \cdot O_i)}} \tag{3.29}$$

HH is also referred as a symmetrically normalized root mean square error: it takes into account both the average and scatter components of the error and it is unbiased towards simulations that underestimate the average.
In these formulations N is the total number of samples, S_i and O_i are the simulated and observed variables with their respective means $\bar{S}$,$\bar{O}$ and standard deviations σ_S,σ_O.

A different treatment is reserved for D_m, which is a circular quantity, and therefore normalized with an angle of 2π radiants (Mentaschi et al. 2015):

$$\text{Normalized Bias} \qquad NBI_{D_m} = \frac{\sum \text{mod}_{-\pi,\pi}(S_i - O_i)}{2\pi N} \tag{3.30}$$

$$\text{Hanna and Heinold indicator} \qquad HH_{D_m} = \sqrt{\frac{\sum \left[\text{mod}_{-\pi,\pi}(S_i - O_i)\right]^2}{N}} \cdot \frac{1}{2\pi} \tag{3.31}$$

where $mod_{-\pi,\pi}(S_i - O_i)$ is equal to $(S_i - O_i) - 2\pi$ if $(S_i - O_i) > \pi$. Vice versa, $mod_{-\pi,\pi}(S_i - O_i)$ is equal to $(S_i - O_i) + 2\pi$ if $(S_i - O_i) < -\pi$.

Finally, in order to better represent the accuracy of the results, also the model skill score ($SKILL$) (Murphy 1988), the root mean square error ($RMSE$) and the $BIAS$ were computed.

$$\text{Model skill score} \qquad SKILL = \frac{\sum(O_i - S_i)^2}{\sum(O_i - \bar{O})^2} \tag{3.32}$$

$$\text{Root Mean Square Error} \qquad RMSE = \sqrt{\frac{\sum(O_i - S_i)^2}{N}} \tag{3.33}$$

$$BIAS = \frac{\sum(S_i - O_i)}{N} \tag{3.34}$$

3.4.2 Tidal and wave stations

The simulated water levels (h) and the simulated wave variables considered in this paper (H_S, T_p and D_m) were compared to the observations provided in the stations shown in Figure 3.4. More specifically, the four tide stations T1, T2, T3 and T4, which are detailed in Table 3.1, are managed by the HO and use acoustic sensors to provide water level values every 10 minutes. These records are referred to the Hong Kong time, which is 8 hours head of the Coordinated Universal Time UTC and their values are in meters above the Chart Datum , which is 0.146 meters above the Hong Kong Principal Datum. The two only existing wave stations in the Hong Kong waters, labeled W1 and W2 (details in Table 3.1), are handled by the Port Works Division of the Hong Kong Civil Engineering and Development Department (CEDD). Specifically, they are bed-mounted wave recorders (both

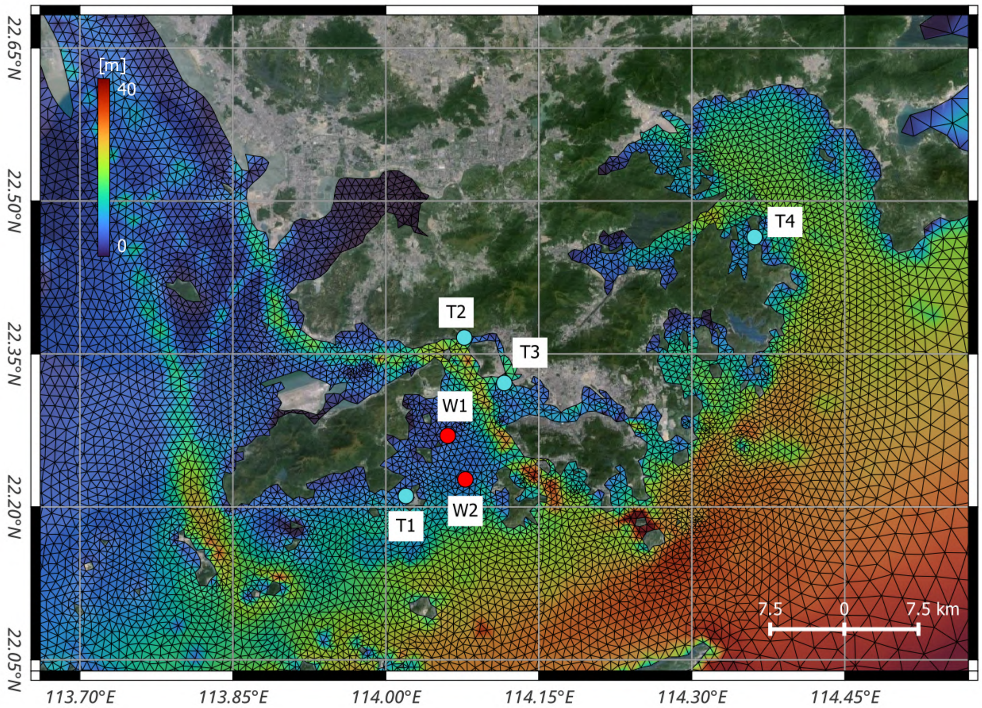

Figure 3.4: Wave stations and tide stations considered for the model validation.

installed at water depths between 9 and 10 m) that provide a hourly long-term wave monitoring program in the harbour starting from 1994.

Station ID	Name	WGS84 Longitude	WGS84 Latitude	Variables	Data availability
W1	Kau Yi Chau	114.0644	22.2649	wave data	Jan 1994 - Dec 2022
W2	West Lamma Channel	114.0767	22.2208	wave data	Jan 1994 - Dec 2022
T1	Cheung Chau	114.0231	22.2142	water level	Feb 2005 - Aug 2020
T2	Ma Wan	114.0713	22.3640	water level	Dec 2004 - Aug 2020
T3	Kwai Chung	114.1227	22.3237	water level	Sept 2001 - Aug 2020
T4	Ko Lau Wan	114.3608	22.4587	water level	Jan 2000 - Aug 2020

Table 3.1: Details of the stations used for the validation of the model.

3.4.3 Satellite wave heights

Further validation of the simulated wave parameters was performed using satellite altimetry. The data were retrieved from the European Space Agency (ESA) Sea

State Climate Change Initiative (CCI) project (Piollé et al. 2020; Dodet et al. 2020) that produced a global dataset of H_S with a spatial resolution of approximately 6 km for each of the satellites deployed in the missions. This study considers the database version 1.1 (Topex satellite from 1992 to 2005) and the database version 3 (Envisat satellite from 2002 to 2012 and Jason-2 satellite from 2008 to 2019) in order to have a proper coverage of most of the hindcast duration. Figure 3.5 shows examples of the satellite tracks in the area of interest. The modeled H_S were interpolated in space and time in order to match the resolution of the measurements along the satellite tracks.

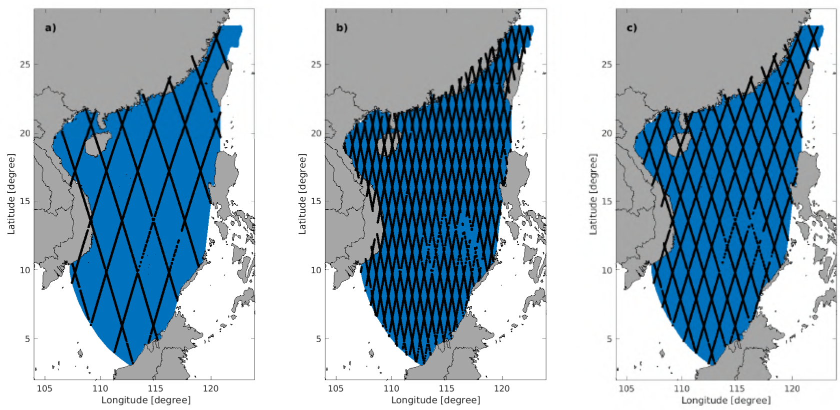

Figure 3.5: Plots of satellite orbits for the three satellites considered: a) TOPEX 2003, b) ENVISAT 2004, c) JASON-2 2016.

3.5 Wave climate trend analysis

For the purpose of estimating wave climate trends, annual maximum (AM) values of significant wave heights were extracted for all nodes of the mesh and then considered in the analysis. The block maxima approach (e.g. retaining annual maximum values of significant wave heights, (Coles et al. 2001)) was therefore adopted for the non-stationary Generalized Extreme Value analysis (GEV). The estimation of trends can be achieved through the implementation of parametric or non-parametric methodologies. The use of a parametric method is contingent upon the assumption of independence and the distribution of the dataset as a normal variable. In contrast, non-parametric methods find application in datasets that are independent (Aydoğan and Ayat 2018). In this work, the Mann Kendall test and the Theil-Sen test are two non-parametric methods that were employed for trend estimation.

The Mann-Kendall test, hereafter referred to as MK, is a non-parametric test that aims at evaluating whether an upward or downward monotonic trend is present within a dataset (Mann 1945; Kendall 1948). The null hypothesis of the test asserts the absence of a monotonic trend in a given time series of n elements x_i, where i= 1, ..., n. The test statistic, Z_{MK}, is computed as:

$$Z_{MK} = \frac{num}{\sqrt{\sigma^2(S)}}, \tag{3.35}$$

where num is defined as:

$$num = \begin{cases} \text{S - 1}, & \text{if S} > 0 \\ 0, & \text{if S = 0} \\ \text{S + 1}, & \text{if S} < 0. \end{cases} \tag{3.36}$$

S and $\sigma^2(S)$ are computed as:

$$S = \sum_{k-1}^{n-1} \sum_{j=k+1}^{n} \delta_{j-k} \tag{3.37}$$

$$\sigma^2(S) = \frac{1}{18}\left[n(n-1)(2n+5) - \sum_{p=1}^{g} t_p(t_p-1)(2t_p+5)\right], \tag{3.38}$$

where the indicator function δ_{j-k} assumes the values 1, 0 or -1 depending on the sign of x_j - x_k (positive, null or negative, respectively); g corresponds to the number of tied groups in the time series and t_p is the number of elements in each pth group, with p = 1 2, ..g. Z_{MK} is then compared to the percentile of the normal distribution. This leads to the corresponding p_{MK} of the statistic:

$$p_{MK} = 2\Phi(-|\mathrm{Z}_{MK}|), \tag{3.39}$$

where Φ represents the cumulative distribution function of the standard normal distribution. Subsequently, the MK test allows to detect statistically significant positive or negative monotonic trends by comparing the p_{MK} of the statistic to the level of significance α by means of the following relationship:

$$\begin{cases} \mathrm{Z}_{MK} > \Phi^{-1}\left(1-\frac{\alpha}{2}\right) & \Rightarrow \text{upward trend} \\ \mathrm{Z}_{MK} < -\Phi^{-1}\left(1-\frac{\alpha}{2}\right) & \Rightarrow \text{downward trend} \\ \mathrm{Z}_{MK} < \left|\Phi^{-1}\left(1-\frac{\alpha}{2}\right)\right| & \Rightarrow \text{no trend} \end{cases} \tag{3.40}$$

In this study, the MK test was performed with a varying level of significance threshold α ranging between 5% and 100%. However, the non-stationary GEV analysis was then applied to all the nodes, hence considering α equal to 100%, in order to assess trends across the entire region.

The Theil-Sen estimation (TS) is another non-parametric method for trend evaluation that identifies the magnitude of a trend by calculating the slope of a linear fit (Theil 1992; Sen 1968). In the context of a time series data x_i (i = 1, …, n), with n being the number of samples), the objective of the TS test is to estimate the median value of the slopes between all possible combination of pairs of data points. The estimation process is outlined as follows and leads to the estimation of the TS slope (b):

$$b = \text{Median}\left(\frac{x_j - x_l}{j - l}\right) \quad \forall l < j, l, j = 1, \ldots, n, \tag{3.41}$$

with x_j and x_l being the jth and lth data of the series, respectively. Differently from a simple least square regression, the TS method is not sensitive to outliers and therefore much more robust (Fernandes and Leblanc 2005; Chervenkov and Slavov 2017).

3.5.1 Non stationary extreme value analysis and return level estimation

Extreme Value Theory (EVT) offers a robust framework for analyzing climate extremes and determining their return levels (Coles et al. 2001; Katz et al. 2002). In a variety of scenarios, the distribution of either the maximum or minimum values of a time series tends to converge to one of the three fundamental statistical distributions: Gumbel, Fréchet, or Weibull. These three distributions can be combined to form the Generalized Extreme Value (GEV) distribution. An alternative form of EVT is the Peak-Over-Threshold (POT) approach, in which only extreme values above a certain chosen threshold are analyzed through a Generalized Pareto distribution (GPD) (Pickands III 1975).

Under the assumption of non-stationarity, the parameters of the distribution functions are time-dependent (Cooley 2009; Katz 2010; Gilleland and Katz 2011; Renard et al. 2012). Specifically, in the NEVA framework, and for the purpose of this work, the location parameter (μ) is assumed to be a linear function of time:

$$\mu(t) = \mu_0 + \mu_1(t), \tag{3.42}$$

while maintaining the shape (ϵ) and scale (σ) parameters constant. The treatment employed for the non-stationary extreme value analysis follows the methodology of the NEVA software package developed by Cheng et al. (2014). In the initial steps of NEVA, the MK test is performed on all the nodes of the mesh in order to detect the presence of trends for a chosen significance level α. Subsequently, regardless of whether the null hypothesis is rejected,the GEV distribution is applied to all the nodes considering annual maximum values of H_S under non-stationary conditions. On the other hand, the POT approach requires the selection of a H_S threshold that in some cases may significantly affect the trend analysis, either in terms of resultant peaks or in magnitude estimation as highlighted by Laface et al. (2016) and Liang et al. (2019). The threshold value can be influenced by climatic trends, while the varying annual frequency of events exceeding this threshold (along with differences in event counts across nodes) introduces challenges in maintaining homogeneity within the reference population relative to AM values (De Leo et al. 2020). Given these limitations, the GEV distribution was selected instead of the POT approach for this analysis. NEVA employs a Bayesian technique to derive the parameters of the chosen distribution. The Bayesian Markov Chain Monte Carlo (MCMC) method is used to infer the posterior parameter distribution from an arbitrary distribution (Braak 2006; Ter Braak and Vrugt 2008; Vrugt et al. 2009). NEVA produces a large number of realizations from the joint posterior distribution of parameters by employing the Differential Evolution Markow Chain (DE-MC). The return levels (q), with the respective return periods (T), that can be calculated according to the NEVA's non-stationary framework are the following:

- standard return levels with design exceedance probability:

$$q_p = \left(\left(-\frac{1}{\ln p}\right)^{\epsilon} - 1\right)\frac{\sigma}{\epsilon} + \mu \tag{3.43}$$

$$T = \frac{1}{1-p}, \tag{3.44}$$

  where p is the non-exceedance probability of occurrence in a given year, q_p is the p-return level and T is the return period calculated according to the formulations provided by Cooley (2012). In this context, the exceedance probability is constant for any given return period during the life of the design.

- standard return levels with time-varying exceedance probability:

$$q_t = 1 - \exp\left\{-\left(1+\epsilon\left(\frac{z_{q0}-\mu}{\sigma}\right)\right)^{-1/\epsilon}\right\} \tag{3.45}$$

$$T = \sum_{x=1}^{x_{\max}} x p_x \prod_{t=1}^{x-1}(1-p_t), \tag{3.46}$$

  where z_{q0} is the event with exceedance probability p_0 = 1 - q_0 at time 0, q_t

is the time-varying return level with respective exceedance probability p_t, x is a generic year and p_x is the exceedance probability at time = x (Salas and Obeysekera 2014). For this matter, sampling approach, parameter estimation and uncertainty assessment remain similar in both design exceedance probability and time-varying exceedance probability frameworks.

- effective return levels:

$$q_p = \left(\left(-\frac{1}{\ln p} \right)^{\epsilon} - 1 \right) \frac{\sigma}{\epsilon} + \mu \tag{3.47}$$

$$T = \frac{1}{1-p} \tag{3.48}$$

The concept of effective return levels was firstly introduced by Katz et al. (2002). Under this perspective, quantiles of extremes vary over time to keep the probability of extreme events constant.

More details about the procedure are well described and documented in Cheng et al. (2014).

3.6 Multifractal detrended fluctuation analysis

For the purpose of this work, hourly values of significant wave heights spanning the period 1970-2022 were considered to perform the MF-DFA method. The data is retrieved from the two-way fully coupled wave-current hindcast provided by Bagnasco et al. (2025), which covers a large portion of the South China Sea (SCS) (as previously shown in Figure 3.2). The numerical mesh deployed in the numerical simulations reaches a fine resolution of around 0.008° in proximity of the Hong

Kong waters and comprises a total of 15523 nodes.

The concept of Multifractal detrended fluctuation analysis (MF-DFA) was firstly introduced by Kantelhardt et al. (2002). MF-DFA is a methodology that can be employed to identify the scaling behavior and the multifractalities of non stationary time series, including for instance significant wave height series (G. Liu et al. 2019; H. Liu et al. 2023a) and it is divided into five major parts. For a given significant wave height time series x(t), t = 1,2, ..., N, the steps are computed as follows:

Step 1: the mean of x(t) is computed and subtracted from the original time series in order to determine the ”profile” Y(i):

$$Y(i) = \sum_{t=1}^{i}(x(t) - \overline{x}), \quad i = 1, 2, \ldots, N \tag{3.49}$$

Step 2: Y(i) is divided into N_s = int (N/s) non-overlapping segments of equal length s. Since N may not be a multiple of the considered time scale s, it is possible that the ending part of the signal will be neglected. In order to include these values, the same procedure is applied starting from the end of the record. In this way, $2N_s$ segments are obtained altogether. However, for the purpose of this study, since the time series comprises 52 years of data, only the initial segmentation was used for analysis.

Step 3: for each segment v, the local trend is evaluated by means of a least-square fit of the data. By then computing the difference between the original time series $Y(i)$ and the fits p_v(i), the detrended time series for a segment of duration s is evaluated:

$$Y_s(i) = Y(i) - p_v(i), \tag{3.50}$$

where $p_v(i)$ is the fitting polynomial in the vth segment. In this work, the fitting procedure is performed by considering quadratic polynomials (characteristic of quadratic DFA) even though other choices foresee even linear, cubic, or higher order polynomials.

Step 4: in this fourth step, the q-th order fluctuation function $F_q(s)$ is computed:

$$F_q(s) = \left[\frac{1}{2N_s}\sum_{v=1}^{2N_s}(F_s^2(v))^{q/2}\right]^{1/q}, \tag{3.51}$$

being $F_s^2(v)$ the variance of the detrended time series $Y_s(i)$ for each of the $2N_s$ segments, computed by averaging over all data points i in the vth segment:

$$F_s^2(v) = \langle Y_s^2(i)\rangle = \frac{1}{s}\sum_{i=1}^{s} Y_s^2[(v-1)s+i] \tag{3.52}$$

Note that for different detrending orders q different fluctuation functions are obtained and for q = 2 the standard DFA procedure is retrieved:

$$F(s) = \left[\frac{1}{2N_s}\sum_{v=1}^{2N_s}(F_s^2(v))\right]^{1/2}, \tag{3.53}$$

Step 5: the scaling behavior of the fluctuation functions is determined by analyzing $F_q(s)$ versus s for each value of q on a log-log plot:

$$F_q(s) \propto C_s^{h(q)} \tag{3.54}$$

Here, the slope of log $F_q(s)$ and $logs$ is the Generalized Hurst exponent $h(q)$. When q = 2, the exponent $h(2)$ is identical to the well known Hurst exponent H, with $h(2)$ varying between 0 and 1. Moreover, the analysis of time series correlation can be conducted using the value of H:

$$\begin{cases} H = 0.5 \Rightarrow \text{the time series is uncorrelated} \\ 0 < H < 0.5 \Rightarrow \text{the time series presents an anti-persistent behaviour} \\ 0.5 < H < 1 \Rightarrow \text{the time series has long-range correlation} \end{cases} \tag{3.55}$$

Additionally, if the time series is characterized by monofractality, this implies $h(q)$ being a constant coefficient, independent of q. Multifractality is instead present whenever there is a significant dependence of $h(q)$ on q. In this case, for values of q<0, $h(q)$ depicts the scaling behavior of the segments with small fluctuations. Differently, for values of q>0, $h(q)$ depicts the scaling behavior of the segments with large fluctuations.

Multifractal time series can also be analyzed by means of the singularity spectrum $f(\alpha)$. We first define the classical multifractal scaling exponents $\tau(q)$ and the generalized multifractal dimensions $D(q)$ as:

$$\tau(q) = qh(q) - 1 \tag{3.56}$$

$$D(q) \equiv \frac{\tau(q)}{q-1} = \frac{qh(q)-1}{q-1} \tag{3.57}$$

$f(\alpha)$ is related to $\tau(q)$ via a Legendre transform (Frisch 1985):

$$\alpha = \tau'(q) \quad \text{and} \quad f(\alpha) = q\alpha - \tau(q), \tag{3.58}$$

where α is the singularity strength or Hölder exponent, while $f(\alpha)$ is the dimension of the subset of the series that is characterized by α. Using Equation 3.56, Equations 3.58 can be further expanded and lead to the definition of both α and $f(\alpha)$ in function of $h(q)$:

$$\alpha = h(q) + qh'(q) \quad \text{and} \quad f(\alpha) = q[\alpha - h(q)] + 1 \tag{3.59}$$

The methodology hereby described was applied to all the nodes of the numerical domain in order to depict the general behavior of the H_S time series. The primary goal of the analysis using multifractal detrended fluctuation analysis (MF-DFA) is to determine the typical time scales associated with significant wave height (H_S) variations in the South China Sea. By analyzing the log-log plots of the fluctuation functions F_n versus the time window s, knee points —where the slope changes significantly— are identified at each location. These knee points correspond to specific values of s, which represent the typical time scales characterizing the multifractal behavior of the wave data. A more detailed analysis was then performed on a set of different locations in the SCS to highlight spatial discrepancies and/or similarities.

3.7 Mangrove attenuation effects on wave action

This section focuses on the investigation of wave attenuation across the mangrove intertidal wetland in Mai Po Nature Reserve. To this end, continuous water level monitoring was performed along three transects strategically positioned at representative locations within the marshes. Additionally, numerical simulations were conducted to evaluate the influence of vegetation on wave characteristics in both Mai Po marshes and Futian Reserve.

3.7.1 Numerical domain and field measurements

The study area, Mai Po Nature Reserve, is a critical intertidal wetland located in the northwestern New Territories of Hong Kong, within the Inner Deep Bay region. Renowned for its rich biodiversity, this site encompasses extensive mangrove forests and mudflats, serving as a vital habitat for migratory birds and a natural buffer against coastal wave action. Figure 3.6 shows Deep Bay and the Mai Po Nature Reserve (in the north-eastern part of the Figure).

Figure 3.6: Aerial view of Deep Bay, Hong Kong.

A particular attention was devoted in selecting the perimeter of the mangrove forest, using the available aerial photographs and the published information. The final proposed coverage of the current mangrove forest can be seen in Figure 3.7.

The numerical mesh developed for the simulation encompasses the entire Inner Deep Bay with a minimum spatial resolution of 20 m. Bathymetric data were derived from the 2022 General Bathymetric Chart of the Oceans (GEBCO) dataset (Weatherall et al. 2015), which provides a resolution of 15 arc-seconds. However, this resolution is relatively coarse for detailed coastal studies, and no high-resolution bathymetric surveys are currently available for the Mai Po Nature Reserve study area.

Figure 3.7: Proposed vegetation coverage for the numerical simulations.

After testing the equipment in the 30-m irregular wave channel in the Hydraulics Laboratory (The Hong Kong Polytechnic University), three “synchro-

Sensor ID	N (1980)	E (1980)	HKPD [m]
1	839449.100	820981.314	1.719
2	839451.723	820974.358	1.778
3	839526.355	821128.287	2.142
4	839444.985	820984.423	1.822
5	839537.320	821111.445	1.860
6	839532.459	821115.504	1.942
7	839966.563	820909.319	1.649
8	839959.667	820918.985	1.787
9	839955.824	820925.961	1.763

Table 3.2: Coordinates (N and E) and vertical heights (HKPD) of the sensors referred to the Hong Kong 1980 Geodetic Datum.

nized" water level sensors were installed in each transect from the leading edge of the marshes to where the water level fluctuations subside. In total, a number of nine sensors were deployed in this project. Figure 3.8 shows the position of the nine sensors and Table 3.2 provides the related coordinates.

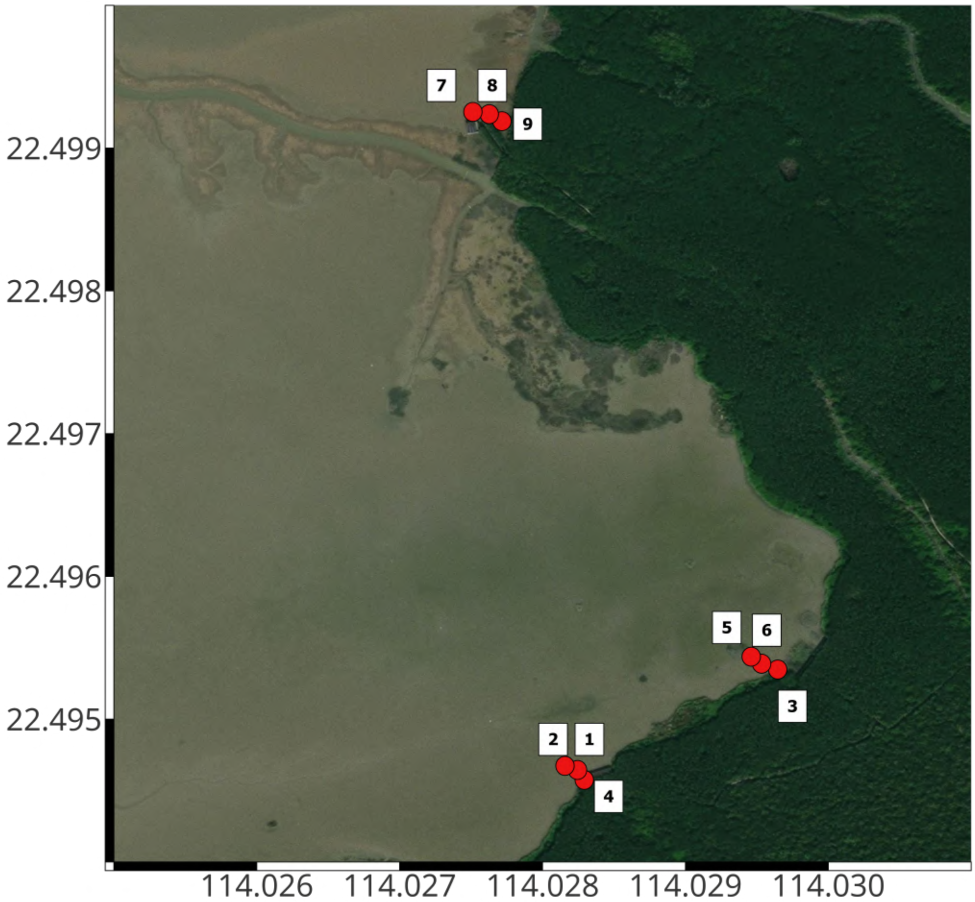

Figure 3.8: Location of the nine sensors installed for the analysis. Longitude and Latitude are shown along the x- and y-axis, respectively.

3.7.2 Model set up

This analysis follows the same numerical framework that was deployed to generate the wave hindcast, as discussed in Section 3.3. However, particular emphasis is placed on the model's representation and treatment of vegetation dynamics. For this reason, specific models are implemented to consider the effect of increased drag due to emergent and submerged vegetation.

3.7.2.1 Vegetation treatment in SCHISM

A coefficient α is included in the bottom stress term of the momentum equation that depends on the vegetation characteristics which is shown in the Navier-Stokes equation below:

$$\frac{Du}{Dt} = f - g\nabla\eta + m_z - \alpha|u|uL(x,y,z) \tag{3.60}$$

Here, u is the horizontal velocity, f represents a number of explicitly treated terms (Coriolis, baroclinic pressure gradient, horizontal viscosity, etc.), g is the gravitational acceleration, η is the surface elevation, m_z the vertical eddy viscosity term (Y. J. Zhang et al. 2016), L(x,y,z) is the vegetation term and the main vegetation parameter 'α' is shown below:

$$\alpha = \frac{D_v N_v C_{Dv}}{2} \tag{3.61}$$

This last equation represents a vegetation related density variable in m^{-1}, where D_v is the stem diameter, N_v is the vegetation density (number of stems per m^2), and C_{Dv} is the bulk form drag coefficient. Selection of C_{Dv} is the topic of other studies with values between 0 and 4 (Nepf and Vivoni 2000; Tanino and Nepf 2008) and is validated against reported laboratory study values. Due to the sensitivity of the above parameter, the hydrodynamic simulations were tested with different values of C_{Dv}.

3.7.2.2 Vegetation treatment in WWMIII

Equation 3.18 presented in Section 3.2 also includes a wave-vegetation sink term named S_{veg}. WWMIII implements the drag force model introduced by Mendez and Losada (2004) of which the main equations are shown below for reference. The vegetation sink term is calculated by

$$S_{\text{veg}} = -\frac{D_{\text{veg}}}{E_{\text{tot}}} N \tag{3.62}$$

where D_{veg} is the vegetation-related dispersion coefficient, defined as

$$D_{\text{veg}} = \frac{\rho}{2\sqrt{\pi}} C_{dv}\, b_v\, N_v \left(\frac{gk}{2\sigma}\right)^3 \frac{\sinh^3(k\alpha_v h) + 3\sinh(k\alpha_v h)}{3k\cosh^3(kh)} H_{\text{rms}}^3 \tag{3.63}$$

Here, C_{dv} is the drag coefficient, b_v is the plant diameter, N_v is the vegetation density, and $\alpha_v h$ is the plant height (α_v being the relative height of the plant). The terms k and σ correspond to the mean wavenumber and mean wave relative angular frequency computed from $T_{m0,1}$. H_{rms} is the root-mean-square wave height, given by $H_{\text{rms}} = H_{m0}/\sqrt{2}$, with H_{m0} denoting the significant wave height. Following Mendez and Losada (2004), C_{dv} can be related to the Keulegan–Carpenter (K) number as follows:

$$C_{dv} = \frac{\exp(-0.0138Q)}{Q^{0.3}} \qquad 7 \leq Q \leq 172 \tag{3.64}$$

with Q defined as:

$$Q = \frac{K}{\alpha_v^{0.76}} \tag{3.65}$$

where the Keulegan–Carpenter number K is given by:

$$K = \frac{u_c T_p}{b_v} \tag{3.66}$$

with T_p the peak wave period and u_c a characteristic velocity acting on the plant. It is defined as the maximum horizontal velocity at the top of the plants ($z = -h + \alpha_v h$) (e.g., Anderson and Smith (2014))

$$u_c = \frac{H_{\text{rms}}\pi}{T_p} \cdot \frac{\cosh(k\alpha_v h)}{\sinh(kh)} \tag{3.67}$$

3.7.3 Set of simulations

Several scenarios were simulated in order to understand the wave and storm surge propagation within Deep Bay and to evaluate the effect of the mangrove forest as follows: Series 1: the first series of simulations was conducted to evaluate wave attenuation along the bay and through the mangrove forest. Three scenarios were simulated using significant wave heights with return periods T_r of 10, 50, and 100 years. For each wave condition, three vegetation drag coefficients (C_{Dv}) were tested: 0 (no vegetation), 2, and 4. The value of 4 represents an extreme condition suggested by Nepf and Vivoni (2000) and Tanino and Nepf (2008), enabling simulation of worst-case scenarios. All simulations were initialized with the water level corresponding to high tide, ensuring complete inundation of both the bay and mangrove forest. This condition represents the most critical scenario for wave propagation. The low tide condition was not investigated, as the mangrove forest becomes dry and wave attenuation is not relevant. Series 2: the storm surge associated with Typhoon Hato (August 2017) was reproduced, with simulations repeated using the same three C_{Dv} values. For the above selected simulations the conditions that were imposed are the following:

1. the eight major harmonic components of the tides (M2, S2, N2, K2, K1, O1, Q1, P1) extracted from the FES2014 package (Carrere et al. 2015).

2. the wave conditions in terms of wave spectrum obtained by a 52-years hindcast produced with the same numerical model strategy (Bagnasco et al. 2025). The hindcast wave data have been analyzed in order to evaluate the wave height and spectral wave period for different storm return periods (10, 50 and 100 years).

3. the storm surge levels during extreme events have been computed using the simulations performed over the entire South China Sea (Bagnasco et al. 2025) and extracted along the present open boundary.

Chapter 4

A two-way coupled wave–current high resolution hindcast for the South China Sea

4.1 Mesh Independence analysis

One of the strictest requirements that any explicit numerical scheme has to fulfill in order to be stable and convergent is the so-called Courant-Friedrichs-Lewy (CFL) condition (Courant et al. 1928): $CFL < 1$, where $CFL = \dfrac{\Delta t \cdot v}{\Delta x}$. In this formula, Δt is the integration time step, v is the flow velocity and Δx is the mesh size. However, the fact that SCHISM is an unstructured model based on implicit time stepping schemes makes the CFL constraint no longer a stringent restriction, as stressed by Y. Zhang and Baptista (2008). For this reason, even significant changes in both the mesh size and time step will not considerably affect the results. Several mesh sizes were tested, with minimum size ranging between 0.001° and 0.01°

in the Hong Kong waters. In particular, five different meshes that differ for the resolution around Hong Kong but share the same grid size offshore and far from the area of interest were considered in the sensitivity analysis: mesh A (minimum size ∼ 0.003°), mesh B (minimum size ∼ 0.004°), mesh C (minimum size ∼ 0.006), mesh D (minimum size ∼ 0.008°), mesh E (minimum size ∼ 0.01°).

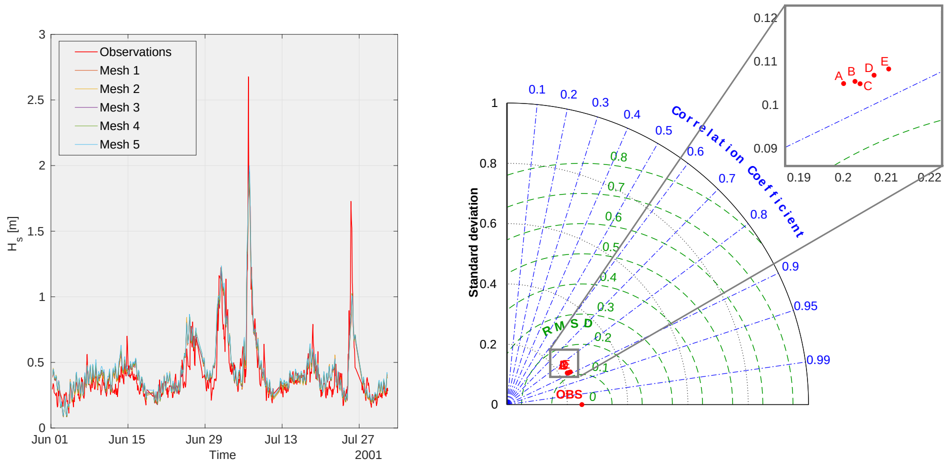

Figure 4.1: Mesh sensitivity test on H_S and related Taylor diagram at station W1 during a time period in 2001.

Figure 4.1 illustrates the outcomes obtained for H_S using the above mentioned unstructured meshes, along with the Taylor diagram in W1 during a time period in 2001. The correlation coefficient (CC) values remain consistently around 0.9, the root mean square difference ($RMSD$) hovers around 0.12 m, and the standard deviation (STD) remains approximately 0.22 m. These results show that increasing the nearshore mesh resolution more than 0.008° doesn't further improve the model skill. Note that a similar analysis has been performed using the observation of the second wave station (W2), not shown here, which lead to very similar results compared to Figure 4.1. A similar analysis was performed comparing the water levels

Station ID	mesh	STD [m]	RMSD [m]	CC
	E	0.636	0.321	0.884
T1	D	0.642	0.316	0.896
	A	0.656	0.334	0.888
	E	0.637	0.326	0.874
T2	D	0.645	0.326	0.881
	A	0.674	0.349	0.880
	E	0.637	0.346	0.855
T3	D	0.645	0.346	0.863
	A	0.673	0.370	0.861
	E	0.578	0.325	0.832
T4	D	0.585	0.322	0.842
	A	0.593	0.333	0.836

Table 4.1: Statistics related to the water levels for the three meshes tested.

at the four tide stations (T1, T2, T3, T4) performing a one month long simulation using three meshes, namely E, D and A. The results in terms of statistical indices are reported in Table 4.1.

The results confirms that no significant differences are detected by comparing the three meshes. Based on the above discussion, a resolution of 0.008° (mesh D) was selected in order to provide sufficient resolution nearshore and reduce the computational time of the numerical simulations.

4.2 ERA5 wind bias correction

As anticipated in Section 3.3.1, ERA5 wind velocities were compared to IFREMER wind velocities in order to apply a hourly bias correction to each node velocity and for the years spanning between 1992 and 2020. The mere comparison between the two datasets, both for the northward and eastward wind components, provides an understanding of the degree of similarity between their distributions. As an example, three locations were selected for analysis: location A (22°N, 114°E), location B (15°N, 114°E), and location C (11°N, 109.25°E). Scatter plots were computed at these locations for the year 2006. Figure 4.2 shows

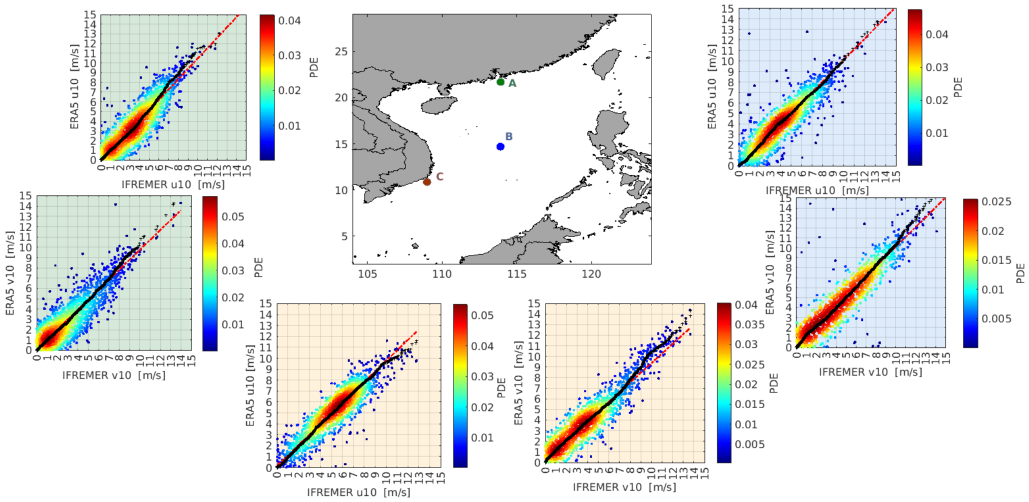

Figure 4.2: Scatter plots and Q-Q plots related to the absolute values of wind velocities in locations A, B, C for 2006.

the positions of these three locations and the related scatter plots where each mark is colored by the spatial density (PDE) of nearby points, computed by means of the Kernel smoothing function. The plots also display the quantiles of the IFREMER wind velocities versus the quantiles of the ERA5 wind velocities. In general, the two distributions are alike if they do not deviate from red dashed line. It can be observed that the two datasets show a strong agreement when the absolute value of their velocity does not exceed circa 7 m/s. In this range of velocities, the eastward and northward wind components therefore manifest robust values of $BIAS$, $RMSE$ and CC. The eastward wind component at location A is characterized by CC equal to 0.998, $RMSE$ equal to 0.169 m and a $BIAS$ of -0.025 m. Beyond that value, the disparities between ERA5 and IFREMER, although still within the range of approximately 1 m/s, begin to grow. In this case, location A shows slightly poorer statistic metrics ($CC = 0.979$, $RMSE = 1.207$ m and $BIAS$ = -1.073 m).

From the plots it seems that ERA5 velocities tend to be higher then IFREMER velocities for values greater than 7 m/s. However, location C seems to show an opposite behavior when the absolute value of the eastward wind velocity exceeds the value of 10 m/s: $BIAS$ reaches a positive value of 0.117 m, $RMSE$ is equal to 0.126 m and CC is equal to 0.983.

Moreover, yearly colored maps were generated in order to show the spatial distribution of the mean wind bias within the SCS: it is therefore possible to understand when the bias becomes positive and when it becomes negative.

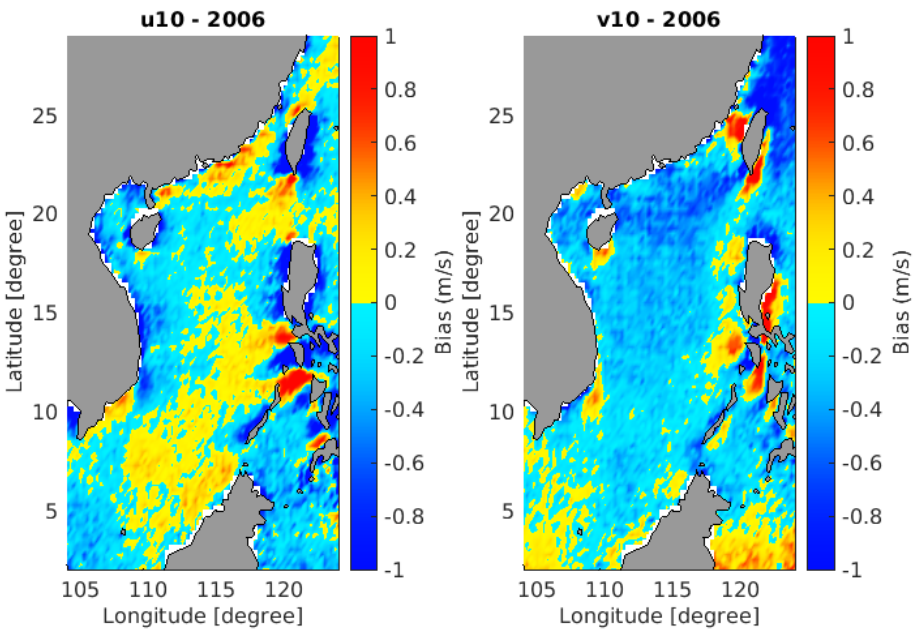

Figure 4.3: Mean annual bias in 2006 for both eastward and northward wind velocity components.

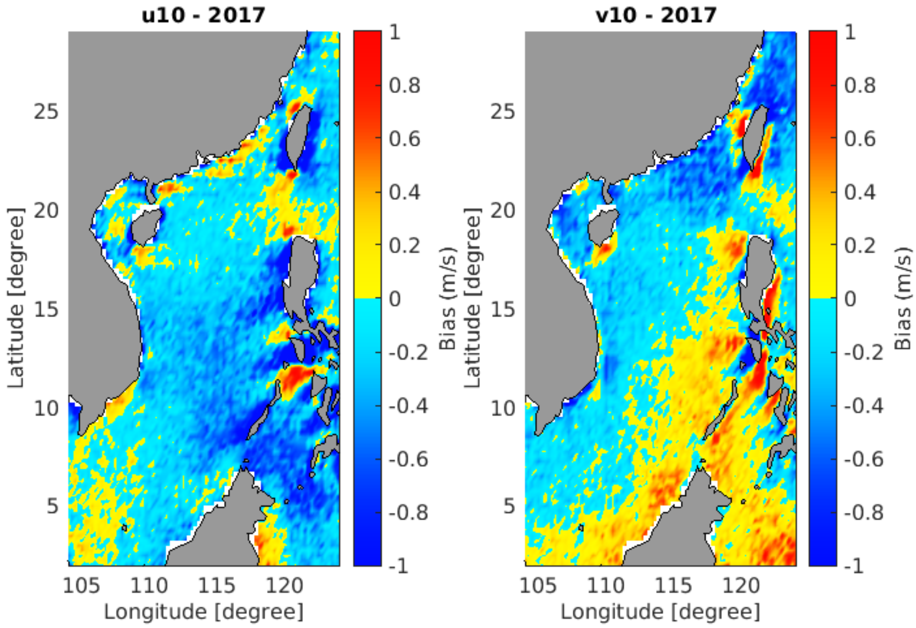

Figure 4.4: Mean annual bias in 2017 for both eastward and northward wind velocity components.

Figure 4.3 and Figure 4.4 show the mean annual bias for the two velocity components for the years 2006 and 2017, as examples. In 2006, the observational data for eastward wind velocities (u_{10}) in the coastal regions between Hainan Island and Taiwan, Taiwan and the northern part of the Philippines, Manila and north of Brunei, and Brunei and Ho Chi Minh City showed positive biases. Differently, the northward wind velocities (v_{10}) are predominantly negative with a few positive patches around Taiwan, at the Philippines and in proximity of Hainan Island. In the year 2017, there appears to be a noticeable resemblance in the behavior of both u_{10} and v_{10} mean biases. Similar to the biases observed in 2006, the coastline extending from the northern open boundary to the left edge of the southern open boundary within the numerical domain exhibits comparable biases. However, in the eastern region of the domain, certain areas around the Philippines, and generally in deep water locations, the mean bias for both components exhibits an opposite sign. The mean annual bias distribution for the entire time range (1992–2020) is provided in Section 9 of Chapter 9 for completeness. The distribution of bias is clearly time and space dependent, with a tendency towards positive bias in the latitude below 15°N. It is often observed a positive bias of the eastward component in the GBA region. The present results seem to be slightly misaligned compared to previous analysis in other ocean basins (Elshinnawy et al. 2024; Campos et al. 2022; Belmonte Rivas and Stoffelen 2019). However, the values of the computed bias are comparable to the above mentioned studies.

4.3 Model performance

The overall performance of the SCHISM-WWMIII two-way coupled model deployed in this study was assessed by considering and analyzing the water level elevations h, significant wave heights H_S, peak wave period T_p and mean wave direction D_m.

As mentioned in Section 3.4.2, 4 tide stations in Hong Kong (T1, T2, T3, T4) handled by the Hydrographic Office of Marine Department (HO) were considered for the water level validation. Hourly modeled water elevation versus hourly observed water elevation were compared for each of the tide stations and for the entire simulation time (1970-2022). Generally, all the locations exhibit similar behavior and demonstrate a solid agreement with the observations.

Table 4.2 summarizes the values of the statistical parameters evaluated to assess the performance of the comparisons. All the four stations are depicted by CC

Station ID	CC	BIAS [m]	RMSE [m]	skill
T1	0.845	0.081	0.369	0.742
T2	0.839	0.102	0.379	0.818
T3	0.803	0.085	0.407	0.720
T4	0.780	0.144	0.407	0.717

Table 4.2: Statistics related to the water levels.

values in the range 0.780 (for T4) and 0.845 (for T1), $BIAS$ values of the order of 0.1 m and $RMSE$ values varying between 0.369 m and 0.407 m. The $SKILL$ parameters for all the locations are greater than 0.7, with the highest value of 0.818 for T2, which suggest a fair agreement between the observations and the simulated variables. C. He et al. (2022) performed a study about coastal macro-vortices dynamics in the Hong Kong waters and validated the 3D FVCOM model against water level observations with the same tidal stations analyzed in this paper. The results lead to CC values of 0.96 in all the stations except for T4 in which CC is equal to 0.95. $RMSE$ ranges between 0.13 m and 0.15 m and the $SKILL$ parameters reach values of 0.97 and 0.98. All these statistics indicate an extremely robust agreement even though the validation only includes the month of December 2017. Differently, statistics of Table 4.2 are referred to the entire available datasets, and therefore cannot be directly compared to the 3D results presented in C. He et al. (2022). Note that the model employed in C. He et al. (2022) was set up with 10 sigma layers and with a spatial resolution down to 50 meters around Hong Kong.

Figure 4.5 displays the Taylor diagrams for all the tide stations in order to provide more information about the comparison. It can be observed that the $RMSD$ values are always less than 0.4 m and that the standard deviations of the simulated water levels fluctuate around 0.6 m.

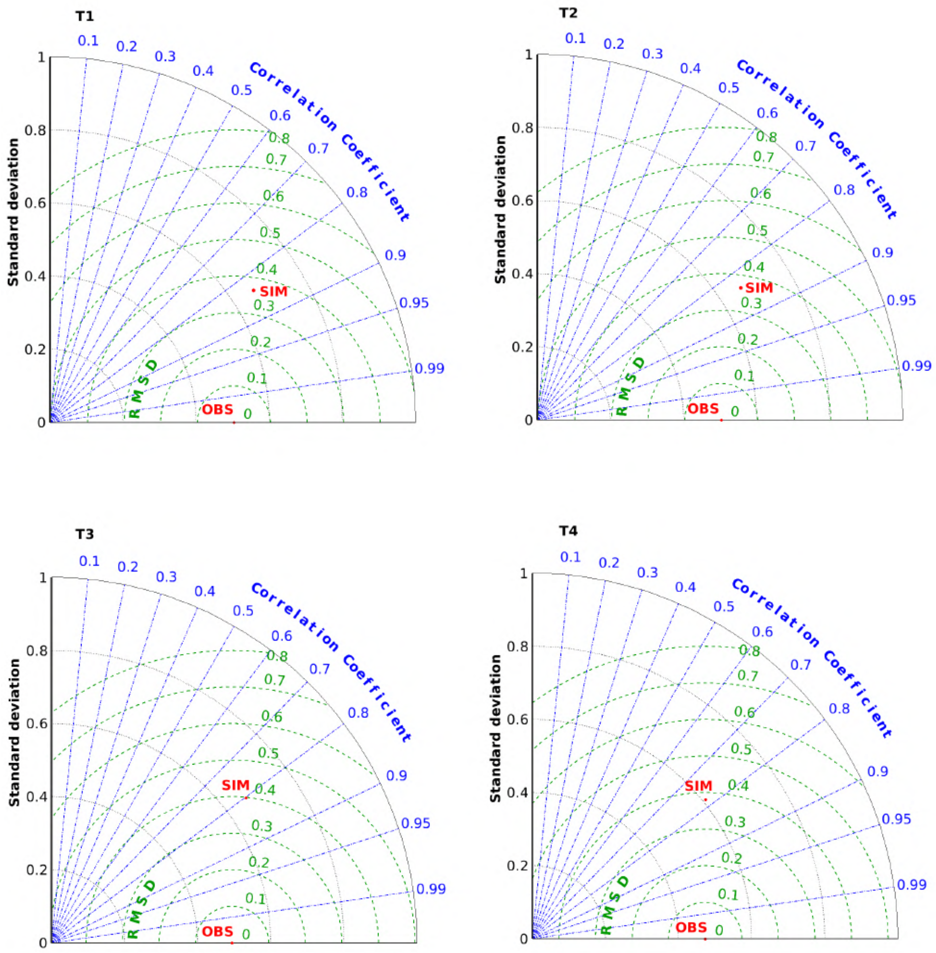

Figure 4.5: Taylor diagrams related to the four tide stations.

Regarding the wave heights validation, the numerical model results were compared to satellite observations. In particular, the significant wave height H_S for the whole numerical domain were interpolated along the satellite tracks, as described in Section 3.4.3.

Table 4.3, Table 4.4 and Table 4.5 show the findings of the yearly statistical analysis for each of the satellite missions considered. It can be observed that the

Year	CC	BIAS [m]	RMSE [m]	NBI [%]	HH
1992	0.884	-0.011	0.475	-0.50	0.204
1993	0.925	-0.060	0.403	-3.90	0.225
1994	0.908	-0.096	0.391	-6.44	0.234
1995	0.935	-0.068	0.384	-4.34	0.208
1996	0.906	-0.091	0.441	-5.70	0.244
1997	0.923	-0.054	0.347	-3.89	0.217
1998	0.935	-0.059	0.350	-4.44	0.219
1999	0.930	-0.019	0.417	-1.17	0.214
2000	0.930	-0.038	0.371	-2.41	0.204
2001	0.918	-0.063	0.381	-4.11	0.219
2002	0.921	-0.055	0.341	-3.92	0.213
2003	0.929	-0.072	0.371	-4.65	0.210
2004	0.907	-0.060	0.393	-3.86	0.225
2005	0.899	-0.103	0.375	-7.82	0.253

Table 4.3: TOPEX Statistics 1992-2005.

Year	CC	BIAS [m]	RMSE [m]	NBI [%]	HH
2002	0.923	-0.074	0.363	-4.86	0.212
2003	0.921	-0.074	0.372	-5.01	0.220
2004	0.914	-0.043	0.362	-2.92	0.218
2005	0.922	-0.091	0.391	-6.00	0.225
2006	0.922	-0.066	0.394	-4.32	0.224
2007	0.935	-0.055	0.374	-3.59	0.208
2008	0.928	-0.035	0.384	-2.25	0.211
2009	0.931	-0.024	0.359	-1.54	0.201
2010	0.920	-0.126	0.387	-9.04	0.244
2011	0.940	-0.035	0.373	-2.06	0.190
2012	0.921	-0.008	0.385	-0.49	0.198

Table 4.4: ENVISAT Statistics 2002-2012.

correlation between satellite data and the simulation is significantly high with CC values between 0.88 (TOPEX satellite - year 1992) and 0.94 (JASON-2 satellite - year 2011). The biases, computed as 'modeled H_S - observed H_S' always appear to be negative with a minimum of -0.008 (ENVISAT satellite - year 2012) except for a positive bias of 0.012 (JASON-2 satellite - year 2018). The $RMSE$ values

Year	CC	BIAS [m]	RMSE [m]	NBI [%]	HH
2008	0.923	-0.037	0.399	-2.37	0.218
2009	0.921	-0.025	0.379	-1.58	0.208
2010	0.924	-0.101	0.371	-7.32	0.233
2011	0.941	-0.022	0.372	-1.31	0.189
2012	0.913	-0.067	0.370	-4.39	0.217
2013	0.922	-0.065	0.375	-4.10	0.209
2014	0.930	-0.034	0.367	-2.31	0.214
2015	0.935	-0.054	0.338	-3.86	0.208
2016	0.940	-0.044	0.351	-3.01	0.203
2017	0.934	-0.047	0.392	-2.74	0.199
2018	0.931	0.012	0.346	0.82	0.199
2019	0.912	-0.009	0.315	-0.64	0.201

Table 4.5: JASON-2 Statistics 2008-2019.

show relatively low values and don't exceed 0.475 m. The normalized bias (NBI) parameters, which serve as indicators of the average component of the error, are always below -10%. Moreover, the Hanna and Heinold (HH) indicators oscillate around 0.2 therefore suggesting good quality of the comparisons. It is worth noting that there is a very low inter-annual variability for all the satellite missions.

Mission	CC	BIAS [m]	RMSE [m]	NBI [%]	HH
TOPEX	0.918 ± 0.015	-0.061 ± 0.026	0.389 ± 0.037	-4.082 ± 1.900	0.221 ± 0.015
ENVISAT	0.925 ± 0.008	-0.057 ± 0.034	0.377 ± 0.012	-3.825 ± 2.397	0.214 ± 0.015
JASON-2	0.927 ± 0.010	-0.041 ± 0.030	0.365 ± 0.024	-2.734 ± 2.082	0.208 ± 0.011

Table 4.6: Statistics related to all the satellite missions: TOPEX (1992-2005), ENVISAT (2002-2012), JASON-2 (2008-2019). Mean values with their corresponding standard deviations are shown.

The statistical parameters were also evaluated for the whole satellite missions, as seen in Table 4.6 and from the scatter plots of Figure 4.6. The overall good performance of the present hindcast when comparing the significant wave heights to the satellite observations is confirmed considering the whole observation periods. Notably, the bias and, consequently the normalized bias, are on average always negative, indicating that the numerical model tends to underestimate the wave height predictions.

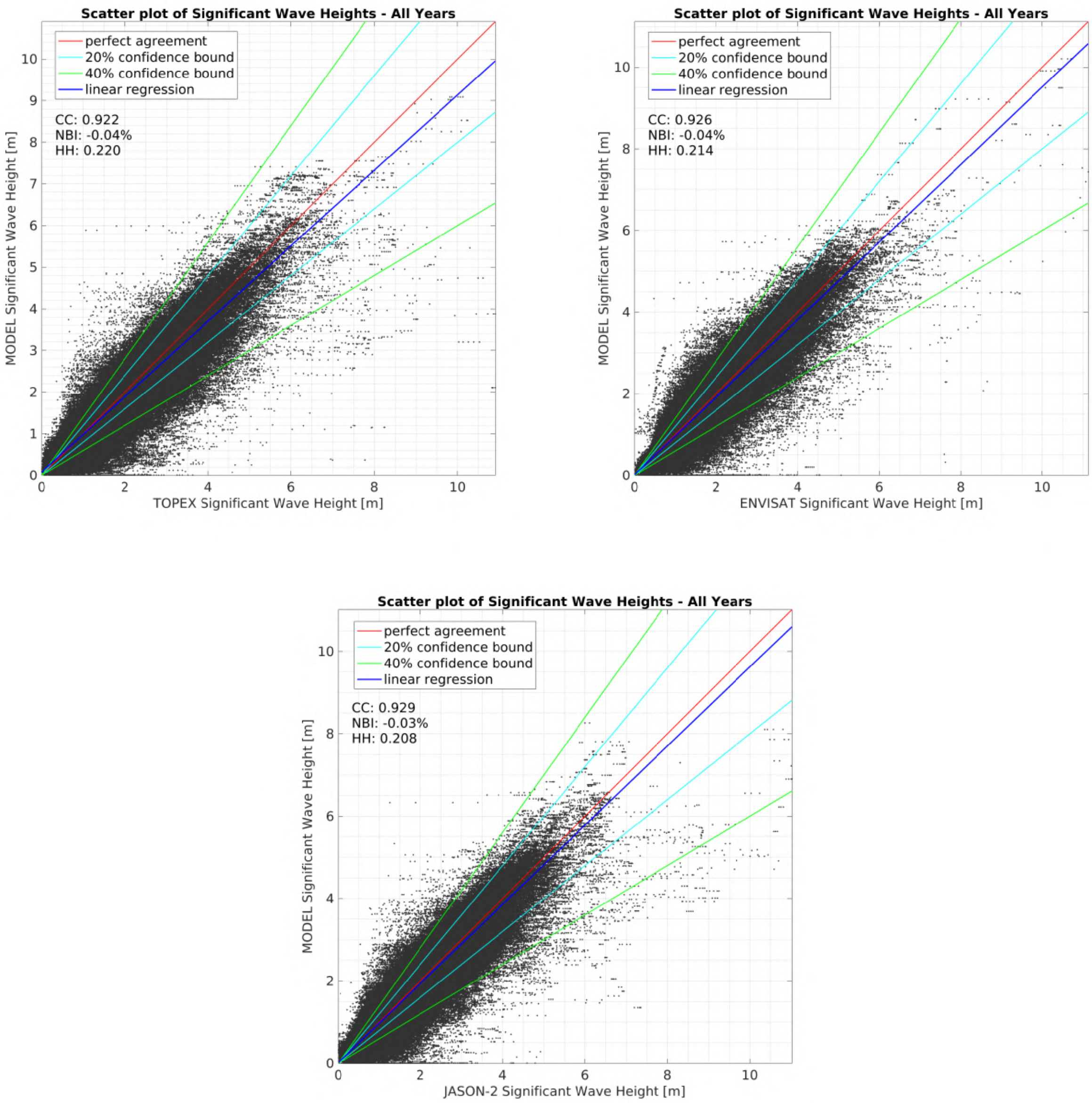

Figure 4.6: Scatter plots of H_S related to the TOPEX (A), ENVISAT (B) and JASON-2 (C) satellite missions.

Regarding the in-situ comparisons at wave stations W1 and W2, the quality assessment was performed by comparing the significant wave height (H_S), peak wave period (T_p) and mean wave direction (D_m).

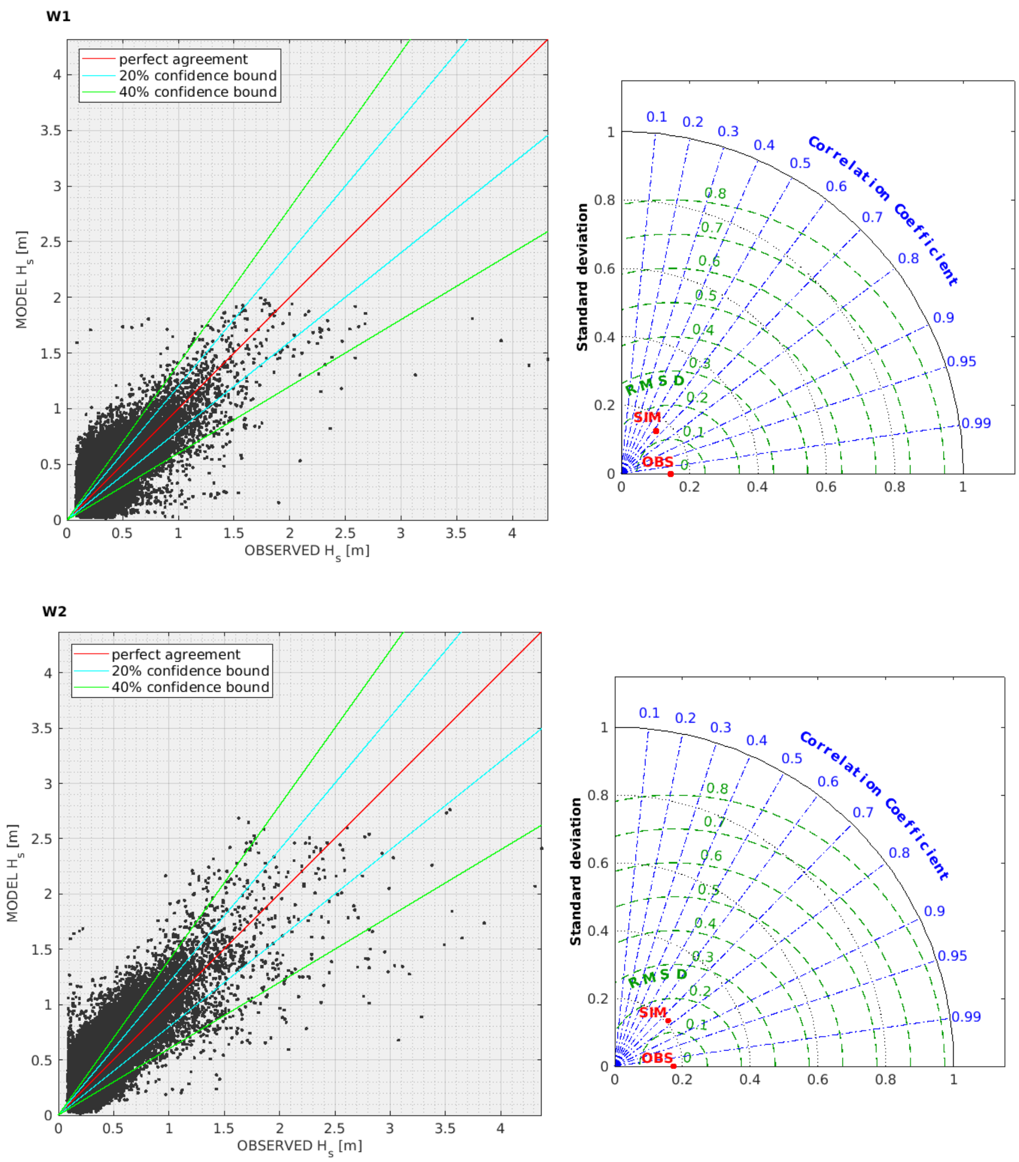

Figure 4.7: Scatter plots and Taylor diagrams related to H_S for W1 (first row) and W2 (second row).

The results for both stations generally show good agreements for H_S values greater than 1 m with only a few outliers. Figure 4.7 shows the scatter plots and the corresponding Taylor diagrams relative to H_S for both W1 and W2. Significant wave heights smaller than 1 m tend to be overestimated by the numerical model. The Taylor diagrams show values of $RMSD$ around 0.15 m and standard deviation around 0.2 m for both stations, whereas the correlation coefficients CC reach values of 0.64 and 0.76 for W1 and W2 respectively. More details can be seen in Table 4.7.

Station ID	**Variable**	**CC**	**BIAS**	**RMSE**	**NBI [%]**	**HH**
W1	H_S	0.637	0.038 m	0.136 m	12.32	0.391
	T_p	0.444	0.049 s	2.218 s	0.83	0.365
W2	H_S	0.761	0.067 m	0.151 m	18.40	0.353
	T_p	0.499	-0.038 s	2.169 s	-0.57	0.318

Table 4.7: Statistics related to significant wave heights and peak wave periods for W1 and W2.

In the same table, the statistical parameters referred to the peak wave periods (T_p) are reported. Correlation values CC for both W1 and W2 are considerably lower than the values obtained for the significant wave heights (H_S). $RMSD$ values are more or less equal to 2 s and the standard deviations of the simulated peak wave periods (T_p) are slightly less than 2 s.

The comparative analysis of mean wave directions (D_m) was conducted using wave roses, as shown in Figure 4.8. As a result of the geographical positioning of the two wave stations, waves originating from the second quadrant (between North and West) are not captured in the simulations. Nevertheless, the observed series of mean wave directions for both stations exhibit the occurrence of minor waves emanating from that sector. This occurrence is likely attributed to the influence of marine traffic within the Hong Kong harbor, including boat wakes, as well as potential errors originating from the wave stations. The analysis reveals that in sta-

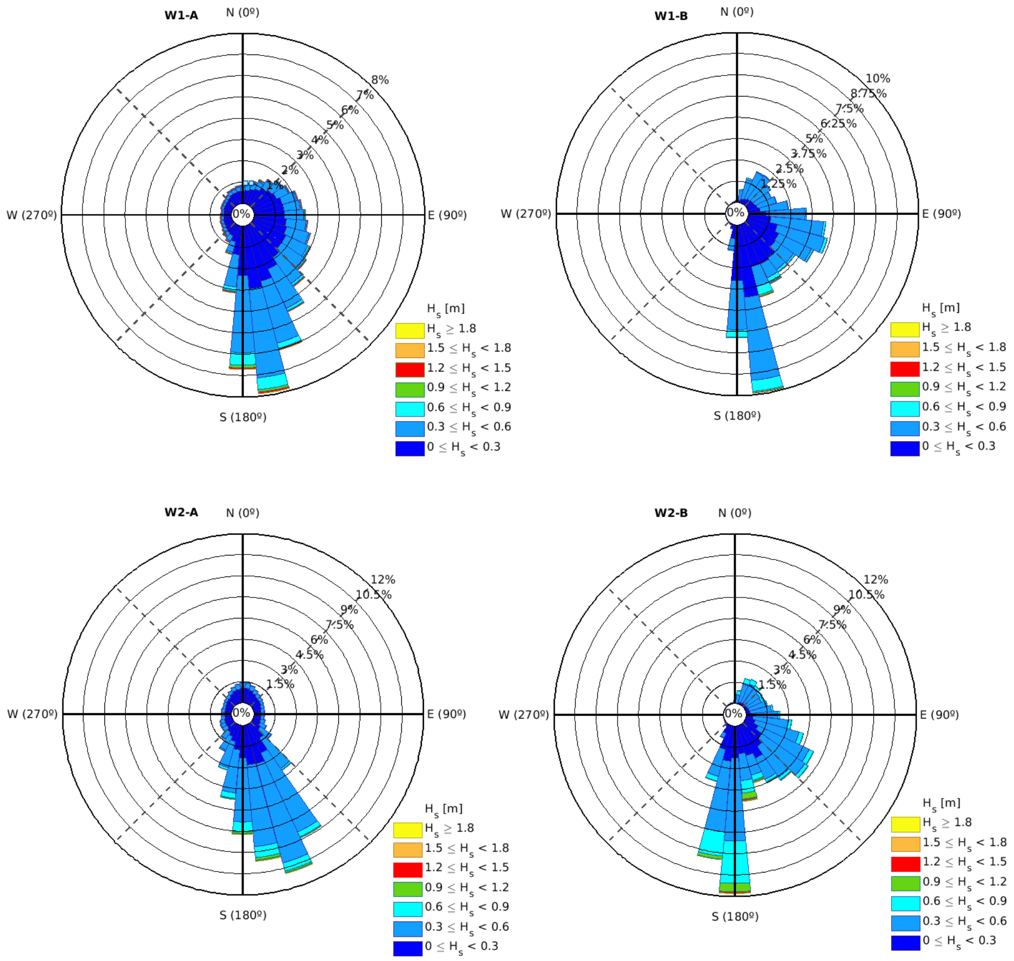

Figure 4.8: Wave roses for both W1 and W2. The plots denoted by A) show the observed D_m and the related H_s while the B) plots are pertinent to the simulations.

tion W1, the most frequently occurring mean wave direction aligns well with the simulated results. However, a relatively poor comparison is found for station W2. In fact, the most frequently observed mean wave direction is South-East, whereas the most frequently simulated mean wave direction tends to be South/South-West. The statistical analysis on the whole dataset for W1 showed a HH_{D_m} value of 0.289 and a NBI_{D_m} equal to 0.250. The W2 station show almost the exact values: HH_{D_m} equal to 0.288 and NBI_{D_m} equal to 0.250. The D_m results show a relatively poor agreement between the outputs of the numerical model and the observations as also highlighted by Kong et al. (2024). Kong et al. (2024) compared the outcomes of the Operational Marine Forecasting System (OMFS) managed by the Hong Kong Observatory to the observations in both W1 and W2, stressing the fact that apparent discrepancies arise due to the inability of the model to properly simulate wave effects in small sea channels.

In order to understand the benefits of deploying a two-way coupling between SCHISM and WWMIII in nearshore areas, the year 2018 had been considered and simulated considering different coupling mechanisms: no coupling, two-way coupling and two one-way coupling scenarios (see Section 2 of the Supplementary Information document). Statistical indicators were evaluated using significant wave height data from stations W1 and W2, as well as water level observations from stations T1, T2, T3, and T4. In addition, nearshore locations in the upper part of the domain had been selected to perform a comparison with satellite data where water depths do not exceed 200 meters, as seen in Figure S1. Considering the statistics at wave stations (Table S1 and Table S2) and tidal stations (Table S4), coupling mechanisms show an increase in both correlation coefficients (between 1% and 4%) and skill parameters (from 3% to about 18%) compared to the uncoupled simulation. Also, the choice of fully coupling SCHISM and WWMIII leads to marginal improvements in terms of correlation coefficients (between 0.1% and 0.7%) and skill values (with a maximum value of 1.1%) compared to both one-way coupling scenarios as seen in Table S4. Similar benefits of fully-coupling versus one-way coupling seem not to appear for the significant wave height statistics as shown in Table S1 and Table S2. From the results obtained in comparison with satellite data, shown in Table S3, no significant changes appear. Statistical parameters show that, in general, a coupling between the hydrodynamic model and the spectral wave model slightly improves the comparisons and reduces the error metrics.

4.4 Simulation of extreme events

The performance of large scale wave hindcasts are known to underperform in the case of extreme events, typically underestimating the significant wave heights (Mentaschi et al. 2023). This tendency is commonly ascribed to the reanalysis of the atmospheric forcing that tend to predict lower winds and atmospheric pressure extremes, typical of tropical storms or typhoons (Schenkel and Hart 2012; Hodges et al. 2017; Campos et al. 2022; Lodise et al. 2024). In particular, several approaches have been showed to effectively reproduce wave and storm surges caused by tropical extreme events (G. J. Holland 1980; Emanuel and Rotunno 2011; J. Yang et al. 2019; J. Wang and P. L.-F. Liu 2021). In the context of extreme events, operational wave models have been observed to underestimate the peak of extreme wave heights, with errors reaching several meters. This phenomenon is frequently observed in comparisons of model forecasts and hindcast to observations during the passage of cyclones (Cardone et al. 1996; Collins et al. 2021). A poor understanding of the physics that govern extreme regimes, the accuracy of wind forcing data, and the challenge of representing the aforementioned dynamics on discrete grids in time and space are often advocated as the main source of discrepancies. These factors lead to the smoothing and underestimation of maximum values, sharp gradients, and overall variability (Cavaleri 2009). This is particularly the case with regard to the area of highest waves, which can be observed in the vicinity of a cyclone's forward motion (Collins et al. 2021).

For all these reasons, in order to optimize peak detection during typhoon events, it was decided to adopt the Holland parametric wind model (G. J. Holland 1980) to simulate part of the typhoons and tropical storms that occurred in the South China Sea during the time frame covered in the present analysis. Details of the model can be found in Section 3.2.1. The same approach was applied by J. Wang and P. L.-F. Liu (2021), for instance, for studying the impact of concurrent storm-tide-tsunami effects in Macau and Hong Kong during Typhoon Hato in 2017 and by N. Wang et al. (2019) to conduct a preliminary analysis of typhoon waves in the Yellow Sea and South China Sea. In a more recent work, Vogt et al. (2024) adopted the Holland parametric wind model to evaluate typhoon induced ocean surge and coastal inundation dynamics around the globe for a series of events. This model is able to satisfactorily reproduce the pressure and wind fields during the passage of typhoons and all the necessary input data for running the parametric model are extracted from the International Best Track Archive for Climate Stewardship IBtrACS (Knapp et al. 2010), the most comprehensive global dataset of historical tropical cyclones activity. Details and procedure on how to generate the pressure and wind fields are well described and documented in J. Yang et al. (2019) and therefore not repeated here.

In the present study, a total of 32 events taken from IBtrACS in the period between 2001 and 2022 were simulated. This is because some events were missing important parameters and typhoon features required by the Holland model tu run. Only events recorded in IBTrACS with complete tropical cyclone parameters for the Holland model were considered. The details of the events and the corresponding tracks are presented in Section 9, Chapter 9.

The following section presents detailed results and a comparison of wave heights between in situ observations and numerical results obtained using the ERA5 and Holland methods for two typhoons occurring in 2009 and 2018, respectively. The information have been collected by the official reports yearly issued by the Hong Kong Observatory (https://www.hko.gov.hk/en/publica/pubtc.htm). We reference the reader to the Supplementary Information document for the results for the rest of the tropical cyclones simulated.

The first event refers to the passage of Typhoon Koppu (0915) in 2009. Koppu developed into a tropical depression over the western North Pacific about 490 km northeast of Manila on 12 September 2009, entered the northern part of the South China Sea with a westerly track on the morning of 13 September 2009 and then turned into a tropical storm. Koppu intensified further into a severe tropical storm on the morning of 14 September 2009 and turned to move northwestwards towards the coast of Guangdong. Koppu reached its peak intensity with estimated maximum winds of 140 km/h near its center in the small hours of 15 September 2009. Koppu weakened into a tropical depression during the early hours of 16 September and then dissipated over Guangxi. The maximum significant wave heights recorded by the wave buoys were about 2.81 m in station W1 and 3.34 m in station W2, see Figure 4.9 and Figure 4.10.

The second period of simulation covered one of the most intense typhoon ever recorded by the wave buoys in the Hong Kong waters, namely the Super Typhoon Mangkhut (1822) between 7 and 17 September 2018. Mangkhut developed into a super typhoon on 11 September, reaching its peak intensity before making landfall over Luzon with an estimated maximum sustained wind of 250 km/h near the

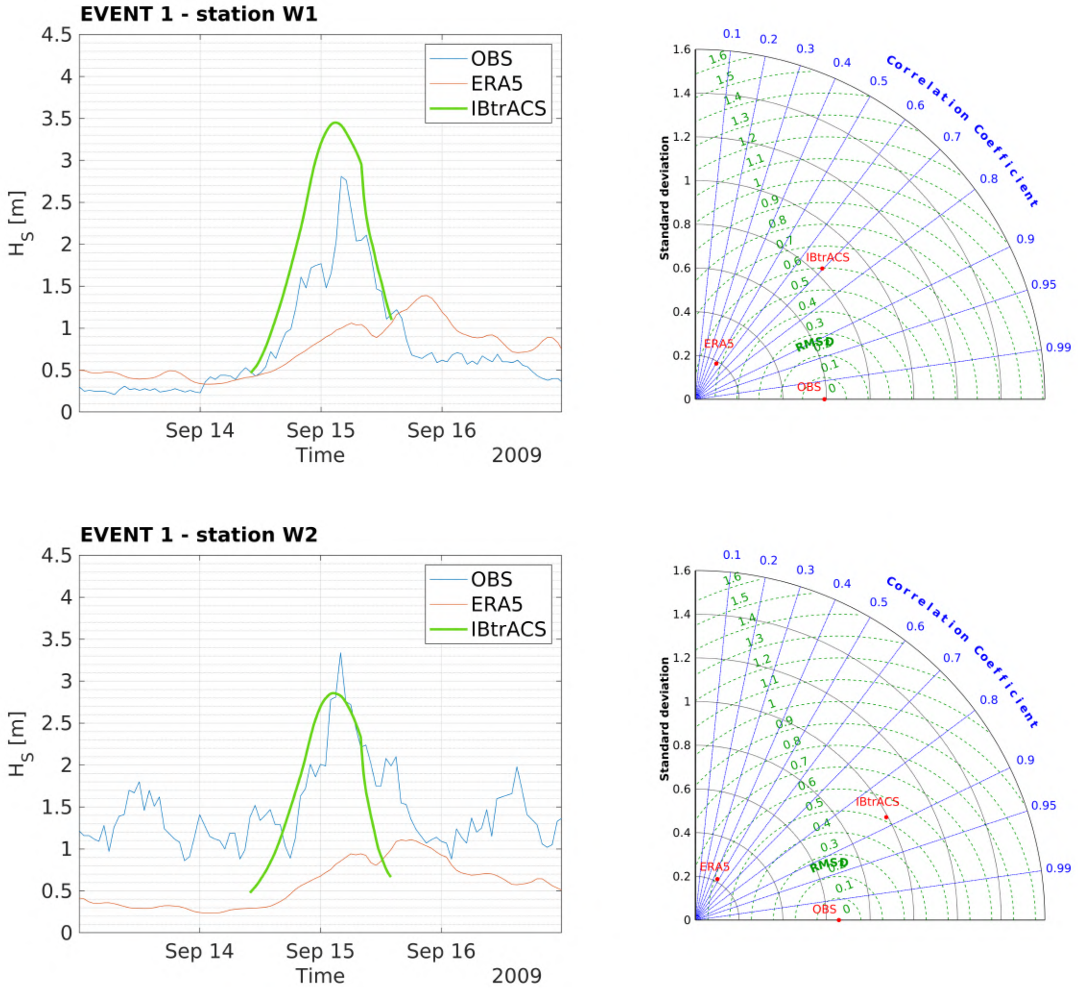

Figure 4.9: H_S plots and Taylor diagrams at stations W1 and W2 related to event 1 (Typhoon Koppu). In the legend: OBS refers to the observed signal, ERA5 refers to the two-way fully coupled signal and IBtrACS refers to the signal obtained with the Holland model.

center. The maximum recorded H_S were 4.37 m at W2 and 4.32 m at W1, see Figure 4.9 and Figure 4.10. Due to its devastating impact, Mangkhut received a lot of attention and several studies have been published both on the analysis of the atmospheric event (J. He et al. 2020; J. He et al. 2022) and on its impact on the

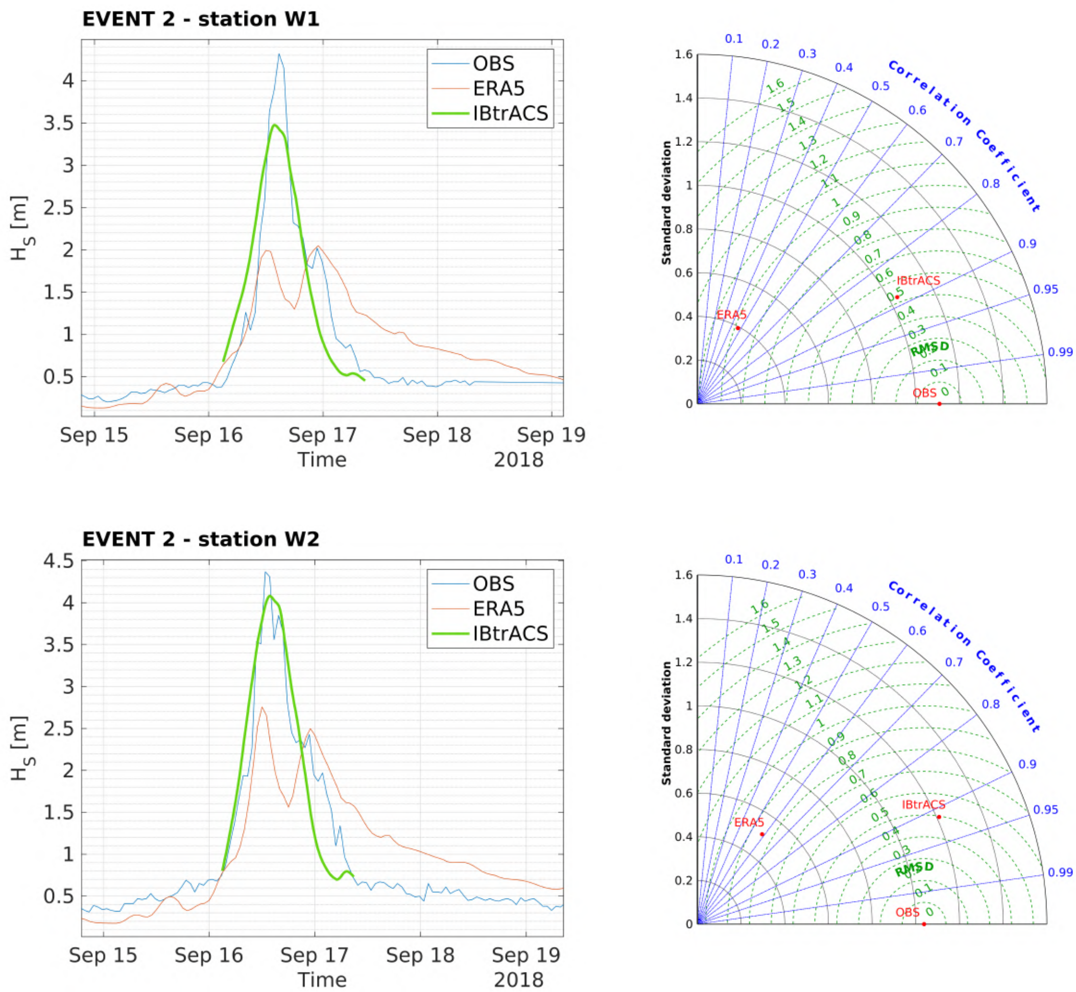

Figure 4.10: H_S plots and Taylor diagrams at stations W1 and W2 related to event 2 (Typhoon Mangkhut). In the legend: OBS refers to the observed signal, ERA5 refers to the two-way fully coupled signal and IBtrACS refers to the signal obtained with the Holland model.

coastal environment and urban areas (J. Yang et al. 2019; Y. He et al. 2020; Zhou et al. 2020).

We compared the outputs of the simulations in terms of significant wave height H_S against the buoy measurements at W1 and W2 and evaluated the model performance using the Taylor diagram. The aim of this analysis is to show the improvements of the Holland parametric model (denoted as IBtrACS) over the two-way coupled simulations based on the ERA5 reanalysis. The results of the analysis are shown in Figure 4.9 and Figure 4.10. For both the events and for both stations, it is clear that the Holland parametric wind model allows a much more improved representation of the typhoon induced significant wave heights. The simulations based on ERA5 were not able to describe properly the passage of the typhoons, leading to severe underestimations of maximum significant wave heights. Regarding event 1, The Holland model brings an increase in the standard deviation from 0.19 m to 0.83 m at station W1 and from 0.2 m to 1 m at station W2. However, the correlation coefficient considerably improves at station W2 from 0.47 to 0.88 and from 0.52 to 0.60 at station W1. $RMSD$ values appear to remain relatively stable. Event 2 shows a similar behavior, with the standard deviation increasing from 0.39 m to 1.04 m at station W1 and from 0.51 m to 1.2 m at station W2. The Holland model induces a 50% reduction in the $RMSD$ values while the correlation coefficients once again significantly increase from 0.47 to 0.88 at station W1 and from 0.58 to 0.91 at station W2.

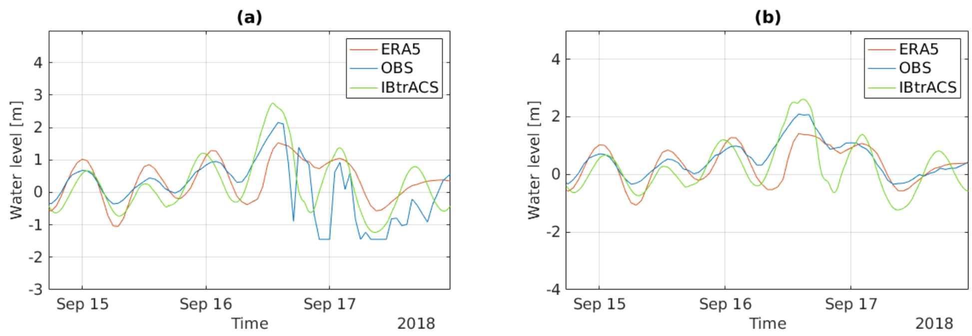

Figure 4.11: Water level signals during event 2 at stations T1 and T3 (panels (a) and (b) respectively). In the legend: OBS refers to the observed signal, ERA5 refers to the two-way fully coupled signal and IBtrACS refers to the signal obtained with the Holland model.

Figure 4.11 presents the time series of water levels (h) at stations T1 and T3 during Typhoon Mangkhut, comparing observations with model simulations forced by ERA5 winds and by the Holland parametric wind model. The Holland-forced simulation provides a visually more faithful depiction of the typhoon-generated storm surge, particularly in terms of the timing and shape of the peak elevation. While the peak water levels are slightly overestimated at both T1 and T3 compared to the observations, the overall surge signature is more realistically captured than in the ERA5-forced case. This comparison illustrates the benefit of incorporating a parametric typhoon wind model for improved representation of extreme storm surge events in the study region.

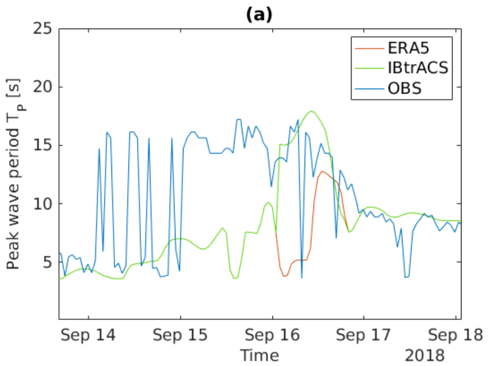

Figure 4.12: Peak wave period signals during event 2 at stations W1 and W2 (panels (a) and (b) respectively). In the legend: OBS refers to the observed signal, ERA5 refers to the two-way fully coupled signal and IBtrACS refers to the signal obtained with the Holland model.

Analogously, Figure 4.12 presents the time series of peak wave period (T_p) at stations W1 and W2 during Typhoon Mangkhut, comparing observations with model simulations forced by ERA5 winds and by the Holland parametric wind model. In the days leading up to the typhoon's approach (approximately 2 days prior), both simulations underestimate the observed peak wave periods. This underestimation is evident in both the ERA5-forced and Holland-forced runs, suggesting that neither wind forcing fully captures the background swell field or the early arrival of longer-period waves associated with the developing typhoon system. The simulation forced by ERA5 winds shows a clear limitation in reproducing the observed wave period evolution, particularly during the typhoon's passage. The peak wave periods are generally underestimated and fail to capture the rapid increase and the timing of the maximum T_p associated with the storm's strongest winds and swell arrival. In contrast, the Holland-forced simulation provides a visually more consistent representation of the peak wave period dynamics. It better captures both the magnitude of the peak T_p and the temporal evolution of the signal during the typhoon event, aligning more closely with the observed behaviour at both stations.

In terms of statistical parameters, the overall performance of the Holland numerical model can be considered satisfactory if compared to the results obtained with the two-way fully coupled simulations based on ERA5. Overall, the performance for extreme events is consistent with previous wave hindcasts using ERA5 (Perez et al. 2017; Shi et al. 2019), with a noted improvement when using the Holland parametrization.

Regarding the prediction of maximum sea levels during tropical cyclones, the results for each event are also presented in table format in Section 9, comparing the outputs from the ERA5 and Holland approaches. It can be observed that the comparison between the simulations and the recorded water levels at different station in Hong Kong significantly improved using the wind and pressure fields computed using the Holland parametrization, especially for very extreme events, such as Koppu (2009), Usagi (2013) and Mangkhut (2018), among others.

The resulting wave–current hindcast is a composite product obtained by merging bias-corrected ERA5 simulations with high-resolution simulations of the 32 selected extreme events forced by the Holland tropical cyclone wind model. At each grid point and time step, the significant wave height (H_S) is taken as the larger of the two values: the bias-corrected ERA5 hindcast or the Holland-forced simulation. An identical maximum-selection procedure is applied to the storm surge/water levels. The corresponding mean wave directions and peak wave periods are those occurring at the instant when the maximum H_S is attained.

Chapter 5

Characterization of significant wave height trends in the South China Sea based on wave hindcast results: a non-stationary extreme value analysis (NEVA)

5.1 Spatial and temporal patterns of significant wave height

Starting from the data provided by the current-wave hindcast (1979-2022), we first characterize the spatial and temporal distributions of significant wave heights within the numerical domain. Shown in Figure 5.1 is the monthly distribution of maximum significant wave heights, while Figure 5.2 shows the seasonal distribution of maximum significant wave heights. The highest maximum wave heights are observed during September and October with a peak equal to 15.90 m in October. The latter is a month during which the typhoon activity is still quite active, and therefore the domain is populated by a larger patch of intense significant wave heights. In contrast, months characterized by lower wave activity are January, February and March with maximum wave heights remaining below approximately 8 m.

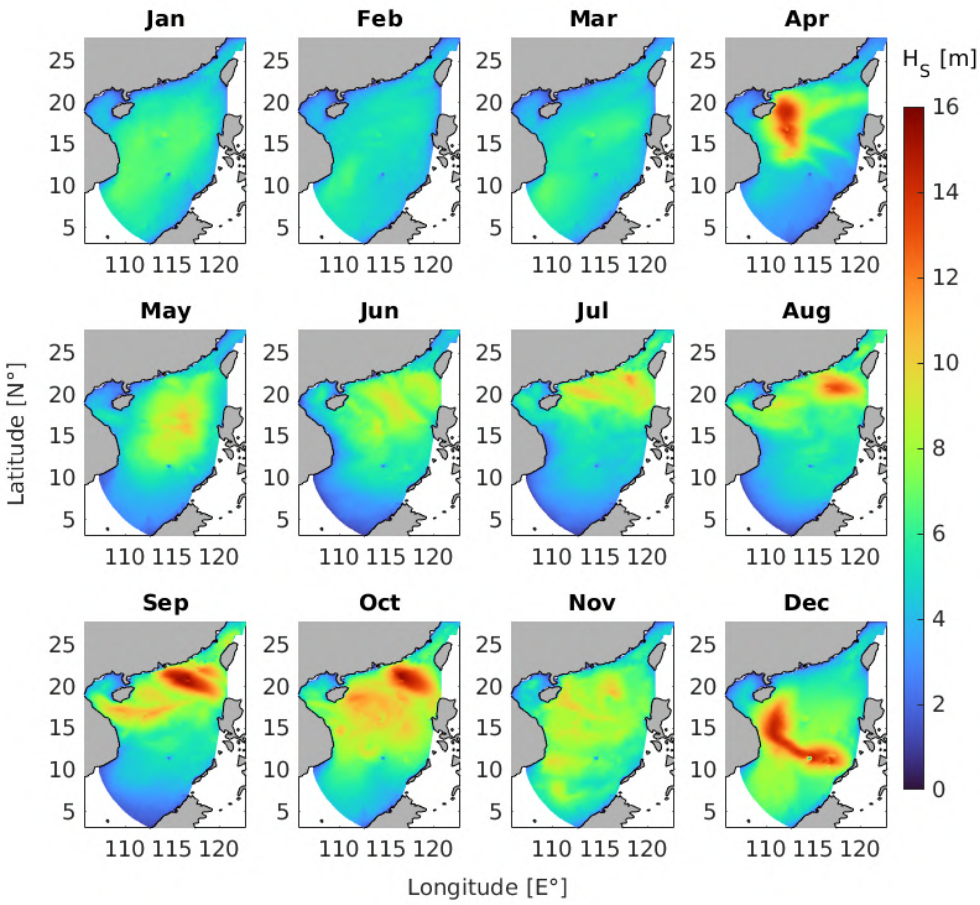

Figure 5.1: Monthly plots of maximum significant wave height.

From Figure 5.2 it is clear that Autumn is the season characterized by the most intense wave activity, especially in the northern part of the domain. From the winter plot it can be observed that the southwestern region is marked by a distinct high-energy zone with peak values of maximum significant wave heights reaching about 14-15 m. The summer season features highest values ($\geq$ 13 m) in the northern part of the basin, especially in the vicinity of the Luzon Strait. Spring months show comparable values of maximum significant wave heights, with the central domain experiencing peaks of 13–14 m. Generally, the highest values occur in open ocean regions, with some localized peaks in the central and southern parts of the domain, identifying areas more prone to extreme wave generation.

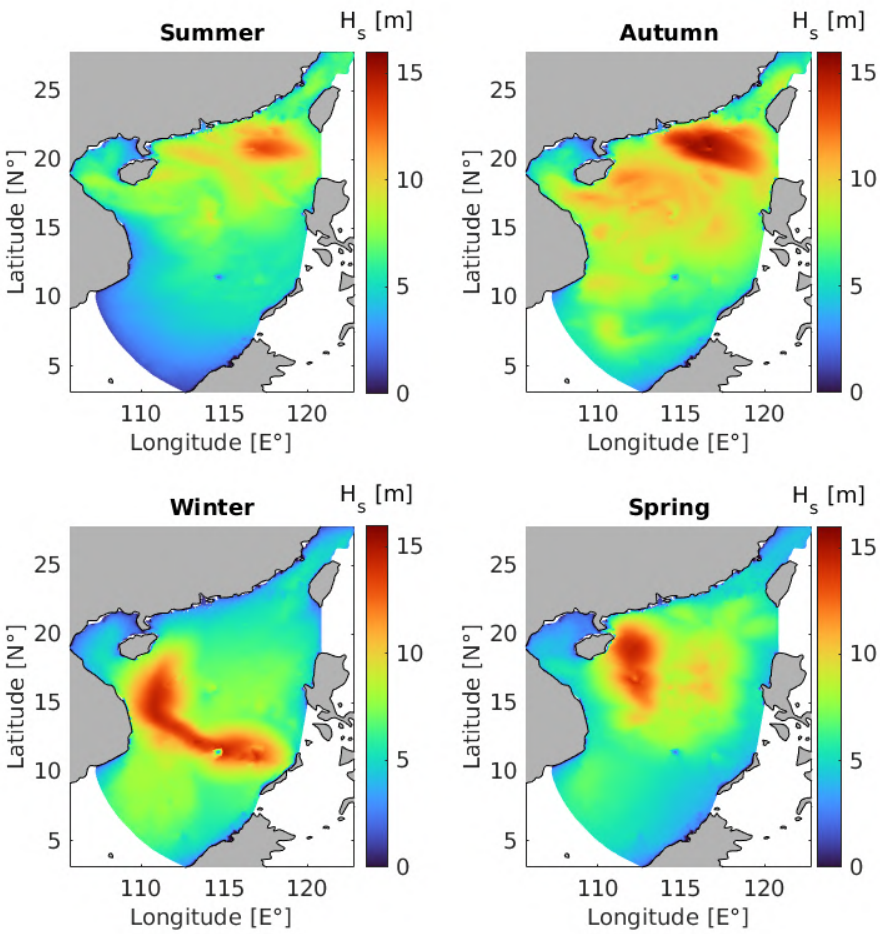

Figure 5.2: Seasonal plots of maximum significant wave height. The months considered for the four seasons are the following: Summer (Jun, Jul, Aug), Autumn (Sep, Oct, Nov), Winter (Dec, Jan, Feb), Spring (Mar, Apr, May).

The fact of not accounting for properly simulated typhoon events, hence by means of the Holland model, implies substantial changes in the significant wave height distributions. Figure 5.3, as opposed to Figure 5.1, shows weaker values of maximum significant wave heights during the months with predominant typhoon activity (August, September and October) and during April and December. As a result, no substantial differences arise in the other months of the year.

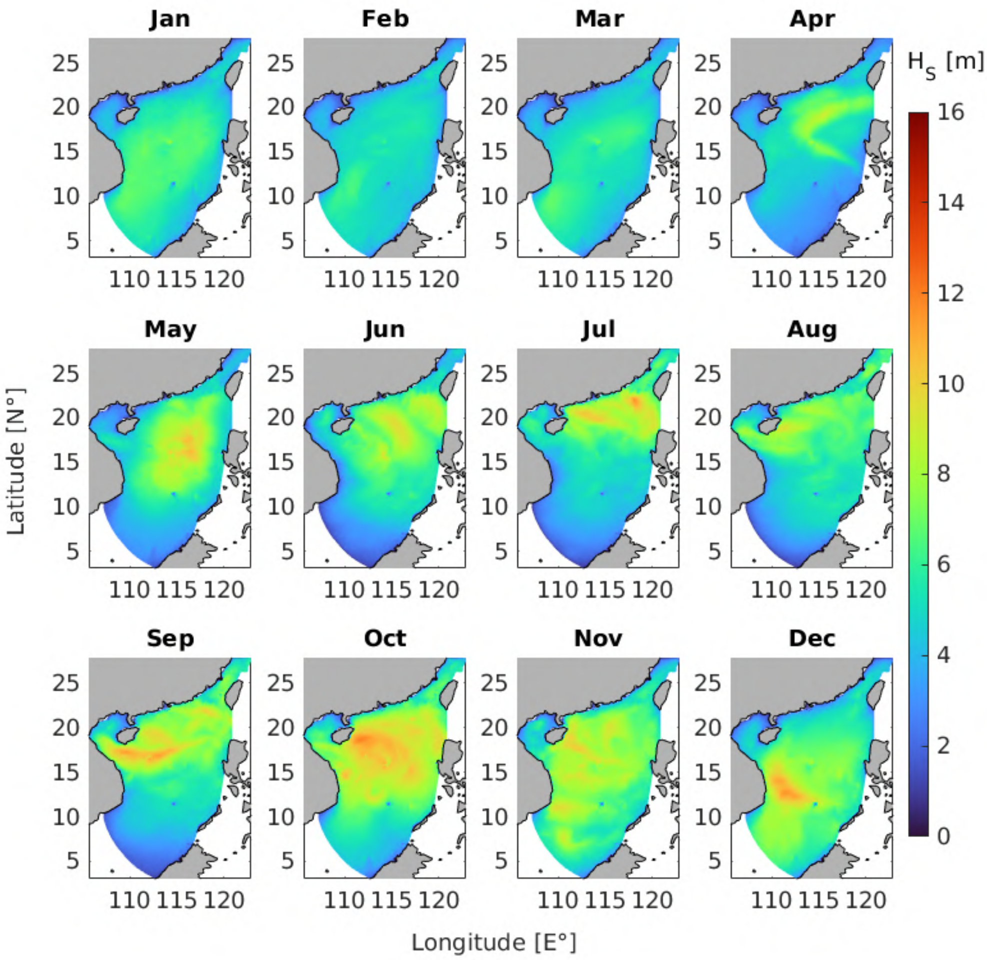

Figure 5.3: Monthly plots of maximum significant wave height in absence of the Holland Model.

Similarly, a comparison between Figure 5.4 and Figure 5.2, shows the latter being characterized by more intense values of seasonal maximum significant wave height, with summer being the season less affected by relevant changes.

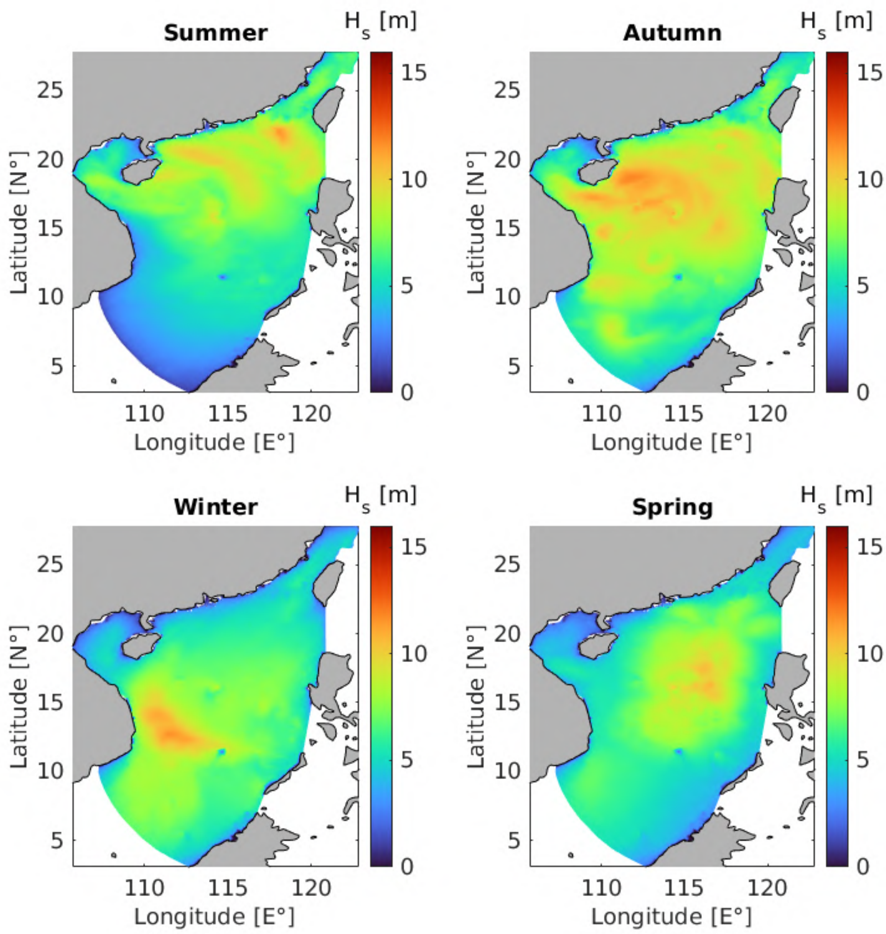

Figure 5.4: Seasonal plots of maximum significant wave height in absence of the Holland Model. The months considered for the four seasons are the following: Summer (Jun, Jul, Aug), Autumn (Sep, Oct, Nov), Winter (Dec, Jan, Feb), Spring (Mar, Apr, May).

5.2 Identification and quantification of trends

The presence of trends and non-stationarities in annual maximum significant wave heights is detected in the NEVA framework by means of the Mann-Kendall test. As described in section 3.5, the test can be carried out for a certain significance level α in order to find statistically significant trends. Figure 5.5 illustrates the results of the Mann-Kendall test for α equal to 5%, 30%, 50%, 80%, 95% and 100%. Figure 5.5 also shows the magnitude of the trend in terms of yearly increment, or decrease, that was calculated through the Theil-Sen estimation (see Section 3.41). As expected from the Mann-Kendall test, the higher the value of α, the more evident the presence of trends. It can be seen that the choice of α = 5% leads to the dominating presence of negative trends around the island of Hainan and in the eastern part of the domain between 12 N° and 25 N° approximately. These negative trends reach maximum values of 0.045 m/year. Some areas characterized by positive trends are located approximately 200 km from the coast of Vietnam (111 E°, 11 N°) with a maximum yearly increment of about 0.019 m/year. As previously mentioned, increasing the value of α results in larger patches characterized by trends. What stands out the most is the extension of the previously found increasing-trend zone (considering α = 5%) in the southern part of the domain. Moreover, more positive trends appear above Taiwan (122 E°, 26 N°) and in some localized areas between the Great Bay Area and the north-western part of the Philippines.

A similar analysis could be conducted on a seasonal basis in order to determine whether the magnitude of the trends changes significantly based on the specific season under consideration. Figure 5.6 shows the MK test and the TS test for the maximum values of significant wave height for all four seasons and only for a α value equal to 100%. It can be observed that summer and autumn are mainly dominated by negative trends except for a part of the domain above Taiwan during autumn. Differently, winter and spring show the presence of more persistent positive trends in the significant wave height distribution. Winter is mainly char-

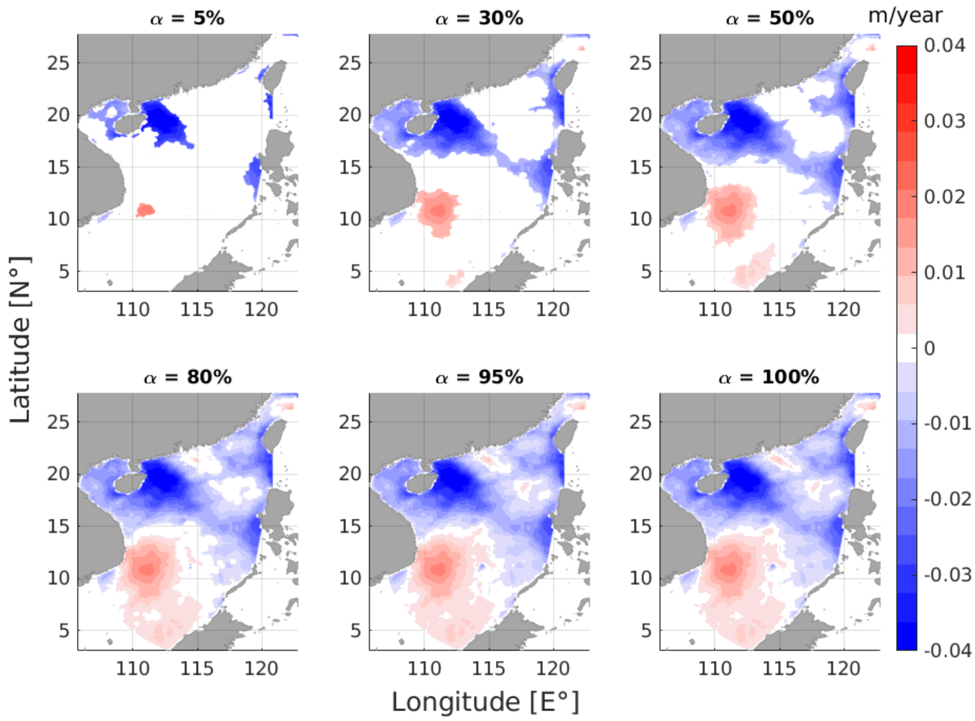

Figure 5.5: Mann-Kendall test and TS slope estimation for different significance levels. Red colors represent positive trends while blue colors refer to negative trends.

acterized by positive trends all over the domain, except for a few nearshore areas along the Chinese coast, around Taiwan, and in the south-western part of the domain next to Vietnam. Spring is characterized by both negative and positive yearly increments; however, more areas characterized by the absence of trends are shown in white. By comparing Figure 5.5 and Figure 5.6, some analogies can be seen in terms of where the positive and negative trends occur. Similarly to Section 5.1, a comparison was made with the results of the MK test and the TS test in absence of the Holland model. As illustrated in Figure 5.7, the positive trends in the southern SCS are less extensive and exhibit lower magnitudes (typically peaking at +0.03 m/year versus +0.04 m/year as shown in Figure 5.5).

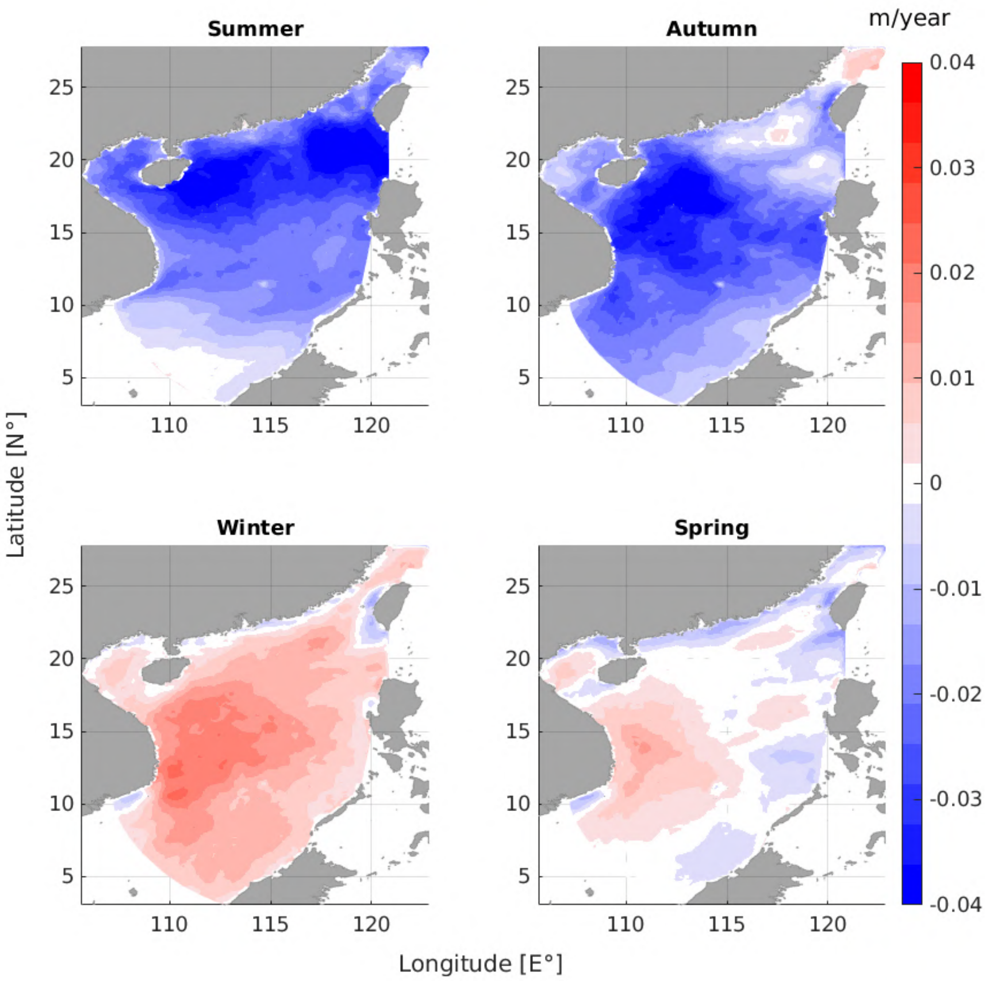

Figure 5.6: Mann-Kendall test and TS slope estimation for a significance level α equal to 100% and for each season. Red colors represent positive trends while blue colors refer to negative trends.

In contrast, negative trends in the northern regions appear more confined and slightly less intense without the model, as the Holland parameterization may enhance resolution of extreme events that influence long-term trends. Additionally, transitional central areas show more insignificance (white regions) at mid-α levels in the hindcast, indicating that the Holland model improves statistical power by refining input forcings, resulting in broader significant trend coverage overall. The main differences between the seasonal results without the Holland model

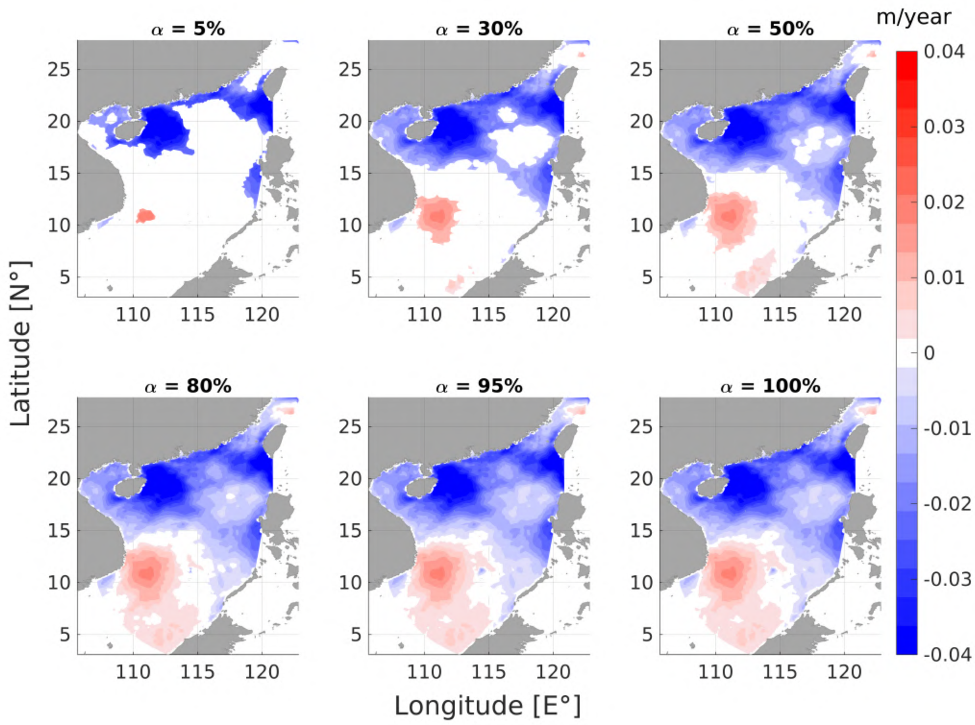

Figure 5.7: Mann-Kendall test and TS slope estimation for different significance levels. Red colors represent positive trends while blue colors refer to negative trends. The plots refer to the hindcast data that does not include the Holland formulation.

(Figure 5.8) and with it (Figure 5.6) are most evident in typhoon-influenced seasons. In Summer and Autumn, Figure 5.8 shows more pronounced negative trends in the north and fewer positive areas in the south compared to the Holland version, where the model likely intensifies positive typhoon-driven trends (expanding red regions by about 20-30% in area). Winter trends in Figure 5.8 are positive but less widespread and intense in the south than in the Holland case, suggesting underestimation of extreme wind effects without the model. Spring patterns are more similar between the two, with minor differences in the extent of transitional zones, implying that non-typhoon seasons are less sensitive to the Holland parameterization.

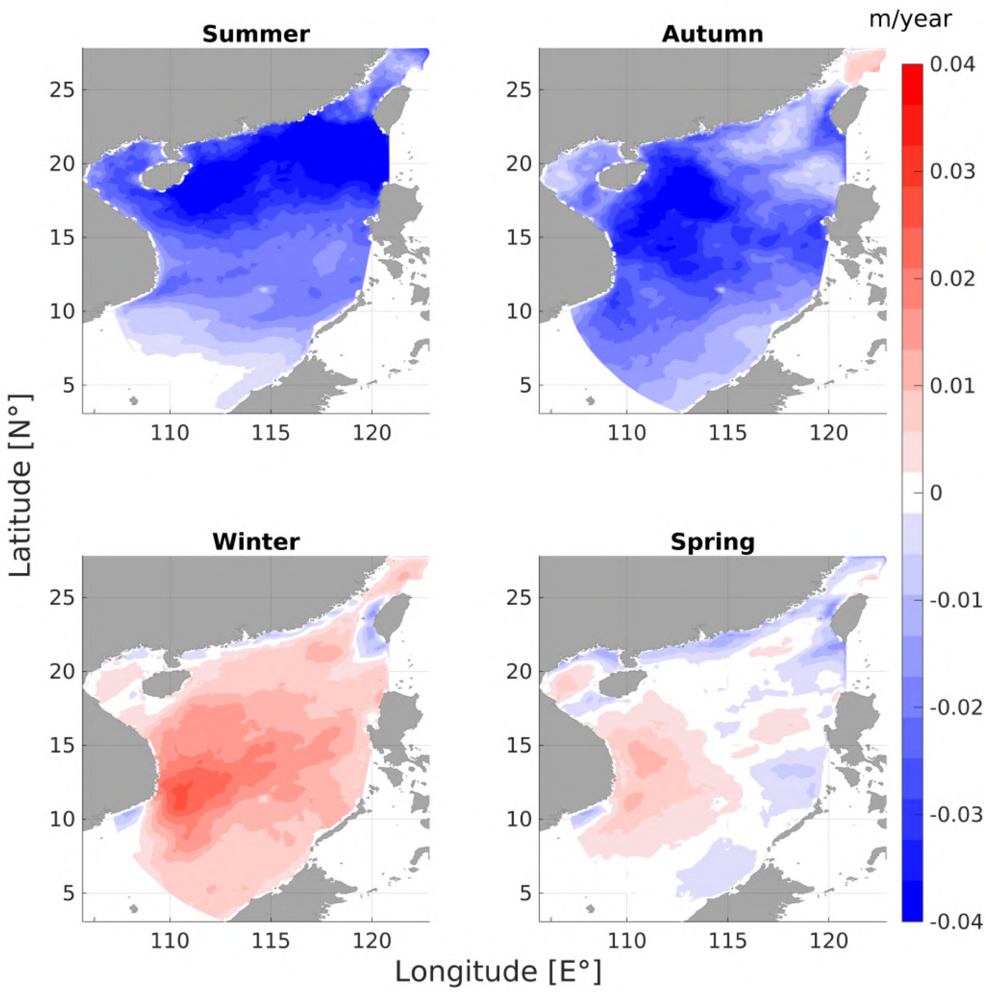

Figure 5.8: Mann-Kendall test and TS slope estimation for a significance level α equal to 100% and for each season. Red colors represent positive trends while blue colors refer to negative trends. The plots refer to the hindcast data that does not include the Holland formulation.

5.3 Return values of significant wave height

After detection of a trend at the chosen significance level, in this case α = 100%, the GEV distribution parameters are estimated under non-stationary assumptions according to the NEVA framework as described in Section 3.5.1.

Figure 5.9 presents spatial distributions of 25-year non-stationary return levels of significant wave height H_S under different estimation approaches and time horizons, providing a comprehensive assessment of present and future extremes. Panel (a) displays the 25-year effective return level computed as the median value over the return distribution in the period 1970-2050, see equations 3.47 and 3.48. It represents a robust central estimate of the extreme wave climate, showing distinct maxima (exceeding 12 m) in the central and northwestern parts of the domain, suggesting persistent exposure to extreme wave events in these regions. Panel (b) shows the standard 25-year return level with design exceedance probability for the whole observation period (1970-2022), calculated as the median while incorporating uncertainty in the model parameters, see equations 3.43 and 3.44. Panel (c) extends the projection into the future 100-year period after the observation window, under the same probabilistic framework as in (b), showing the average future scenario. The spatial distribution remains consistent, though some localized intensification of return levels is observed, particularly near 20 °N, 112 °E, indicating potential future increases in extreme wave risk. Panel (d) instead, shows the projections near the end of the 100-year period, thus emphasizing high-impact scenarios. This results in noticeably higher return levels in high-energy regions, especially along the north-western shelf, and can be useful for critical infrastructure design and coastal hazard planning.

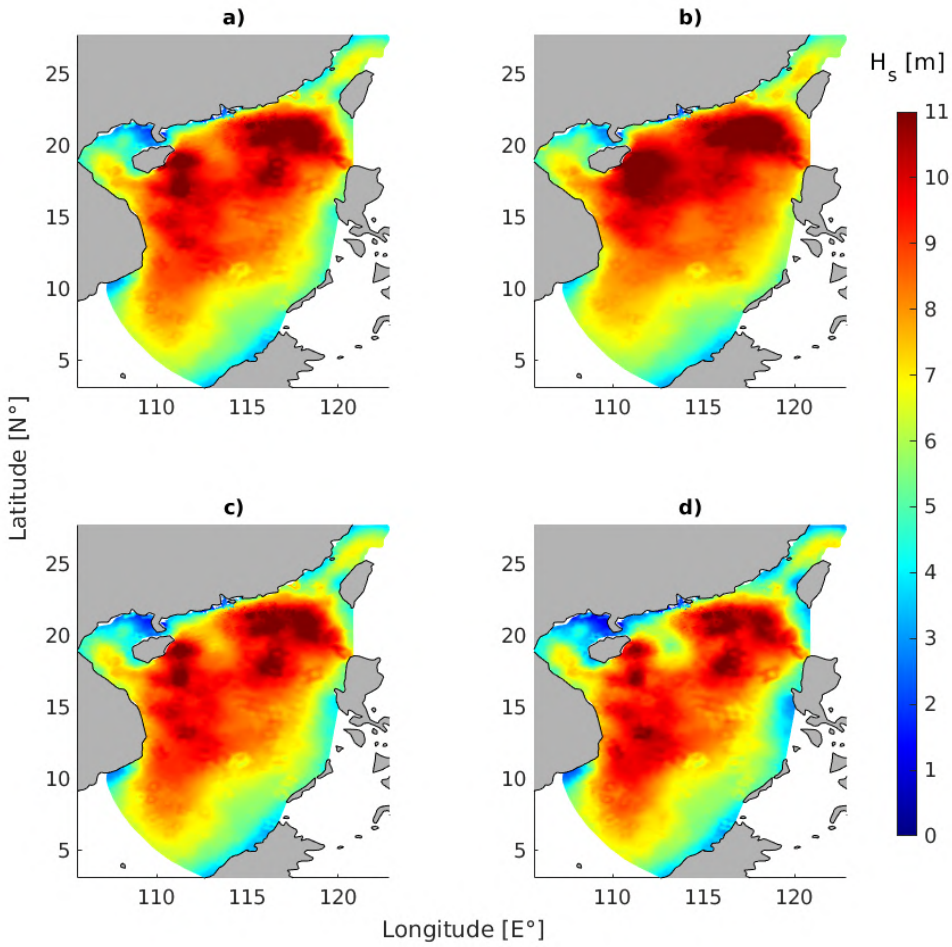

Figure 5.9: Median 25-year non-stationary return level estimates calculated with different approaches. (a): 25-year effective return level during 1970-2050; (b): standard 25-year return level with design exceedance probability during 1970-2022; (c): projected standard 25-year return level with design exceedance probability 100 years after 2022 (average scenario); (d): projected standard 25-year return level with design exceedance probability 100 years after 2022 (scenario near the end of the 100 years).

NEVA also allows users to estimate non-stationary return levels excluding the uncertainties in the parameters of the distribution. In general, including parameter uncertainty (b–d) leads to higher and more spatially extensive return level estimates, which is critical for conservative design and risk management (Serinaldi 2015). Future projections (c–d) indicate possible increases in extreme wave height in the locations characterized by positive trends, which may be associated with climate-induced changes in storm frequency or intensity (Morim et al. 2019; Grossmann-Matheson et al. 2024). The northwestern and central parts of the domain consistently emerge as hotspots for extreme wave activity across all configurations, suggesting that particular attention is needed in coastal planning and offshore infrastructure design.

Now, Figure 5.9 was replicated for the dataset not accounting for the Holland model as presented in Figure 5.10. The spatial distribution of H_S across the SCS shows a central peak with values ranging from 5 to 11 m, similar to the Holland model case but with notable differences. Panels (a) to (d) depict variations in return levels over different time frames and exceedance probabilities, with the highest values concentrated in the central basin, gradually decreasing toward the northern and southern boundaries. Compared to Figure 5.9, the absence of the wind parametric model leads to a more subdued peak in H_S, with maximum values typically reaching 10-11 m versus the slightly higher peaks (up to 11-12 m) observed in Figure 5.9. This suggests that the Holland model, by incorporating asymmetric typhoon wind fields, enhances the estimation of extreme wave heights, particularly in the central region prone to typhoon activity. Additionally, the spatial extent of high H_S values (greater than 9 m) is more confined without the model, indicating that the Holland parameterization extends the area of significant wave impact, likely due to better representation of storm-induced dynamics. The differences are most pronounced in panels (a) and (b), where the Holland model amplifies the effective return levels, reflecting its role in capturing long-term non-stationary trends more effectively.

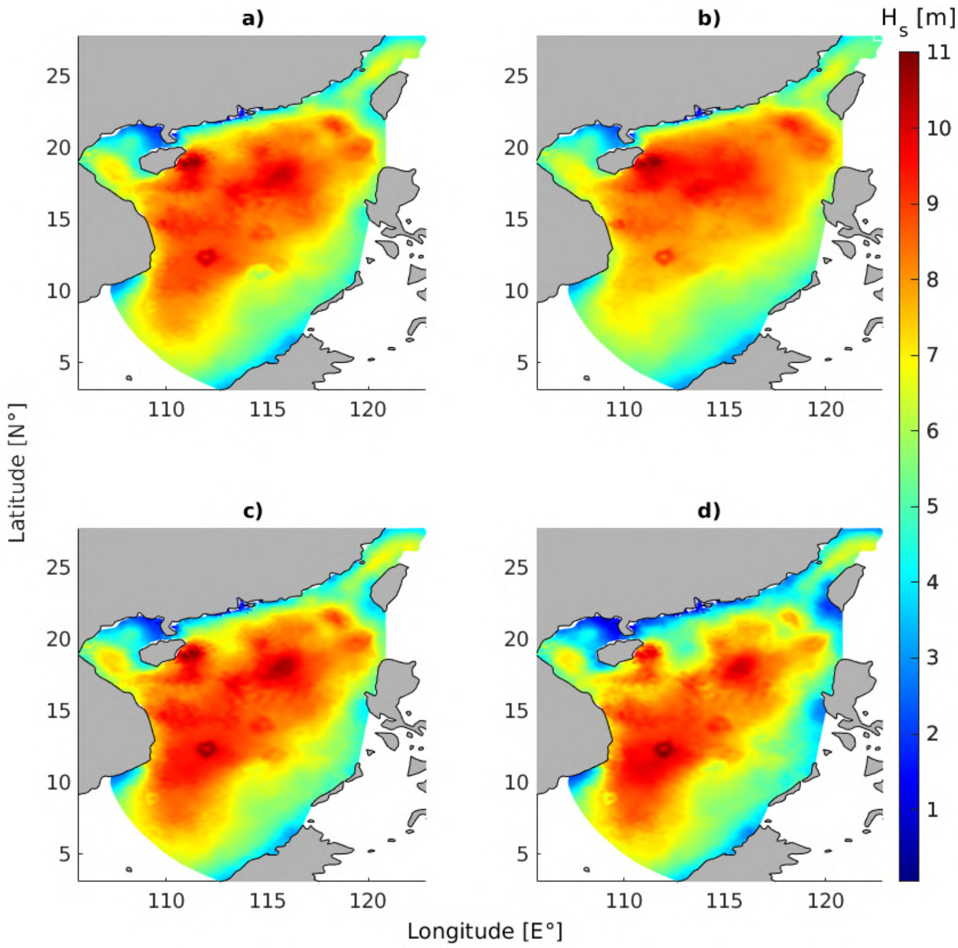

Figure 5.10: Median 25-year non-stationary return level estimates calculated with different approaches. (a): 25-year effective return level during 1970-2050; (b): standard 25-year return level with design exceedance probability during 1970-2022; (c): projected standard 25-year return level with design exceedance probability 100 years after 2022 (average scenario); (d): projected standard 25-year return level with design exceedance probability 100 years after 2022 (scenario near the end of the 100 years). The plots refer to the hindcast data that does not include the Holland formulation.

5.4 Evaluating non-stationary return levels at selected locations: Location A and Location B

In order to further extend the analysis, results and plots related to two specific locations, as shown in Figure 5.11, are provided below. Location A is situated at (118.92 N°, 21.43 E°), while location B is at (114.96 N°, 21.41 E°). Both sites were selected since they reside in a region frequently affected by typhoons and extreme weather events, as seen in Figure 3.1.

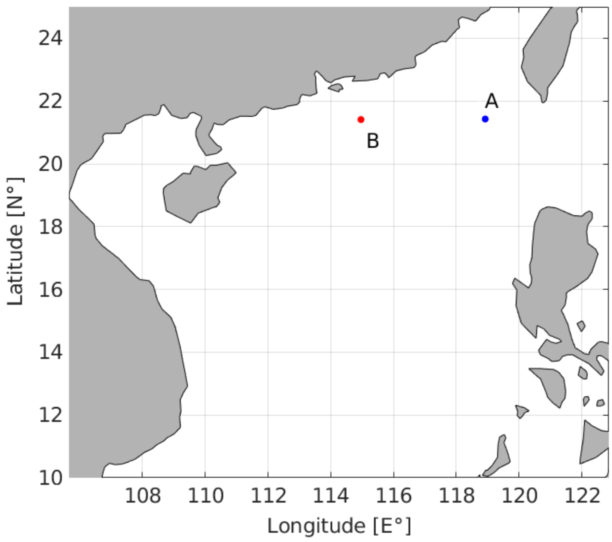

Figure 5.11: Visualization of the two selected locations for the localized return level analysis.

Figures 5.12 and Figure 5.13 show the standard non-stationary return levels with design exceedance probability (Equation 3.43)at location A and B, respectively. Panels (a-c) are calculated in the same way as panels (b-d) in Figure 5.9. For a 100-year return period, the median return level in panel a) is approximately 14.3 m for location A and 12.5 m for location B. If considering the standard return levels projected to the year 2122 in panels b) and c), it is shown that location A is characterized by lower values of 13.3 m and 12.7 m. Differently, the upward trend at location B implies an increase in the 100-year return level estimates up to 12.9 m and 13.1 m in panels b) and c), respectively.

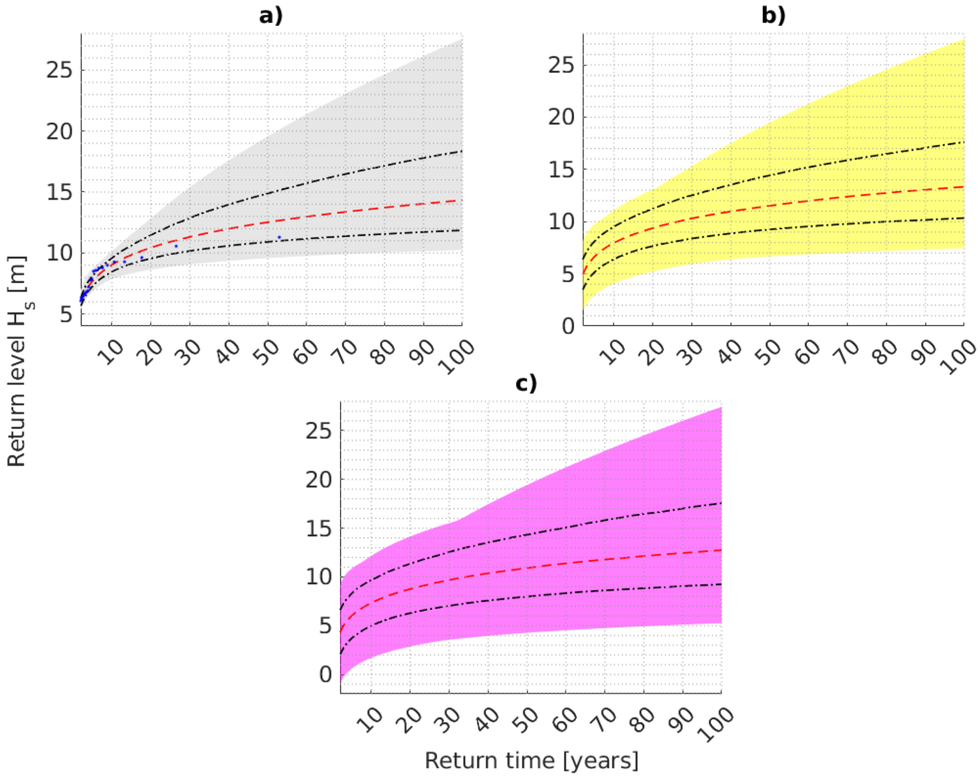

Figure 5.12: Non-stationary return level estimates versus return times for location A. The red dashed line represents the median of the samples while the black lines identify the confidence intervals: 5th (lower line) and 95th (upper line) percentiles of the samples. Blue dots in (a) represent the empirical return levels. The shaded regions (grey, yellow, and magenta) illustrate the ensemble spread of the return level estimates.

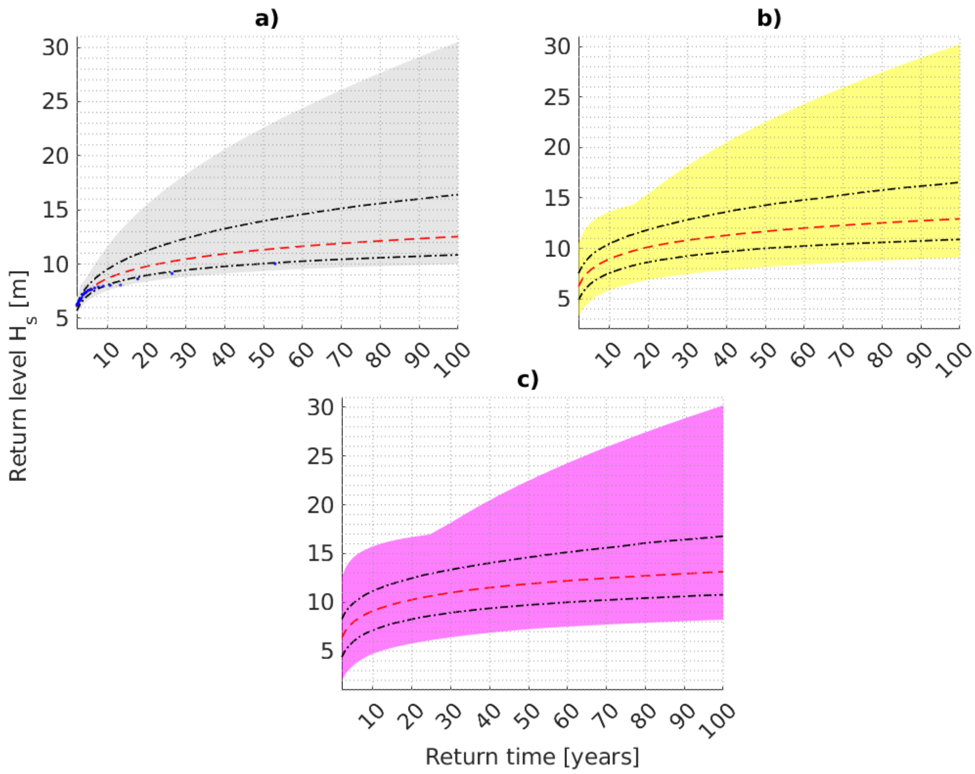

Figure 5.13: Non-stationary return level estimates versus return times for location B. The red dashed line represents the median of the samples while the black lines identify the confidence intervals: 5th (lower lined) and 95th (upper line) percentiles of the samples. Blue dots in (a) represent the empirical return levels. The shaded regions (grey, yellow, and magenta) illustrate the ensemble spread of the return level estimates.

Figures 5.12 and 5.13 were also replicated for the dataset that neglects the Holland model and presented here. The findings are displayed in Figures 5.14 and 5.15. It can be seen that, for a 100-year return period, the median return levels in panel a) are now reduced to about 10.8 m for location A and 9.0 m for location B if compared to those in Figure 5.12 and Figure 5.13. The projections for the year 2122 at location A (Figure 5.14) show values of 8.8 m and 7.7 m for panels

a) and b), respectively. On the other hand, values of 7.8 m and 7.0 m are depicted in Figure 5.15. The non inclusion of maximum H_S values calculated with the Holland model lead to negative trends at both locations, therefore in contrast with the upward trend previously found at location B.

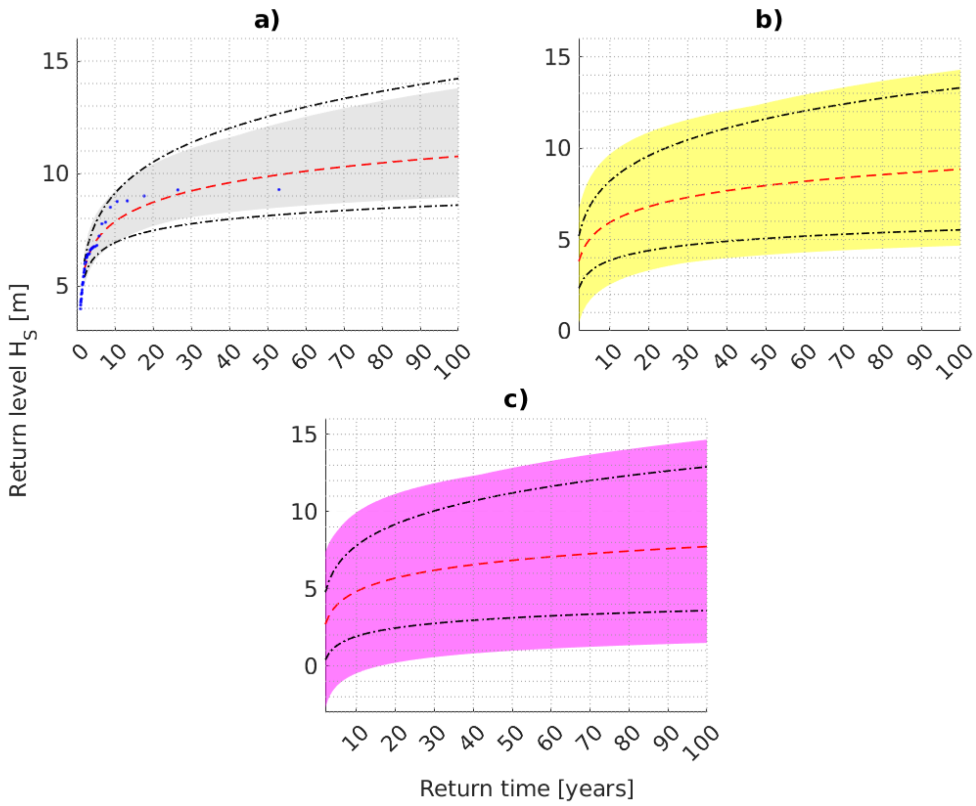

Figure 5.14: Non-stationary return level estimates versus return times for location A. The red dashed line represents the median of the samples while the black lines identify the confidence intervals: 5th (lower line) and 95th (upper line) percentiles of the samples. Blue dots in (a) represent the empirical return levels. The shaded regions (grey, yellow, and magenta) illustrate the ensemble spread of the return level estimates. The plots refer to the hindcast data that does not include the Holland formulation.

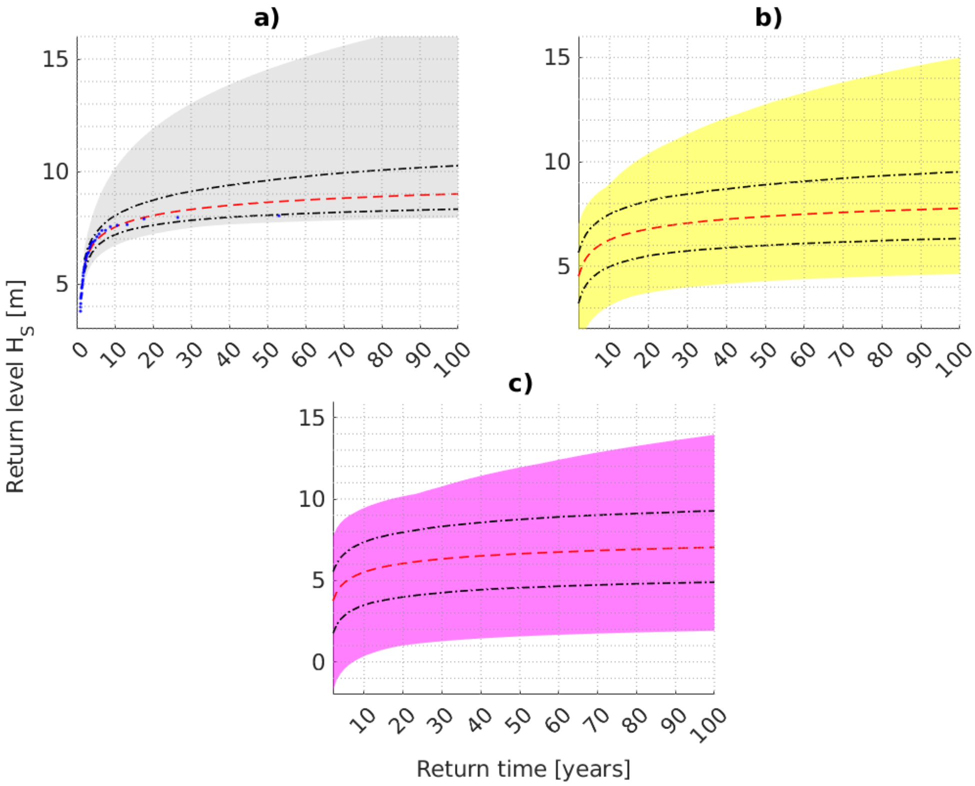

Figure 5.15: Non-stationary return level estimates versus return times for location B. The red dashed line represents the median of the samples while the black lines identify the confidence intervals: 5th (lower lined) and 95th (upper line) percentiles of the samples. Blue dots in (a) represent the empirical return levels. The shaded regions (grey, yellow, and magenta) illustrate the ensemble spread of the return level estimates. The plots refer to the hindcast data that does not include the Holland formulation.

As previously seen in Section 5.2, location A exhibits a negative trend of 1.3 cm/year, while location B shows an increasing trend of 0.97 cm/year. Figure 5.16 and Figure 5.17 show the effective return levels at locations A and B, calculated with Equation 3.47. In the concept of effective return levels, the return levels change over time while ensuring that the probability of occurrence remains constant. The effective return level indicates what return level should be considered for all years to maintain a constant level of risk (Cheng et al. 2014). In particular, they provide curves for 2-, 10-, 25-, 50- and 100-year effective return levels. These figures also show the annual maxima values of H_S for the whole duration of the hindcast and highlight the differences arising when the Holland model is not applied. It is apparent that the effective return levels at location A decrease over time (hence indicating a downward trend) while they slightly increase over time at location B due to the presence of an upward trend. For instance, the effective return level at location A corresponding to a 50-year event (probability of occurrence equal to 0.02) during 1970-1980 (index t on the x axis equal to 11 years) is 12.72 m.The same risk for a 51-year period (1970-2020) would be 12.17 m.

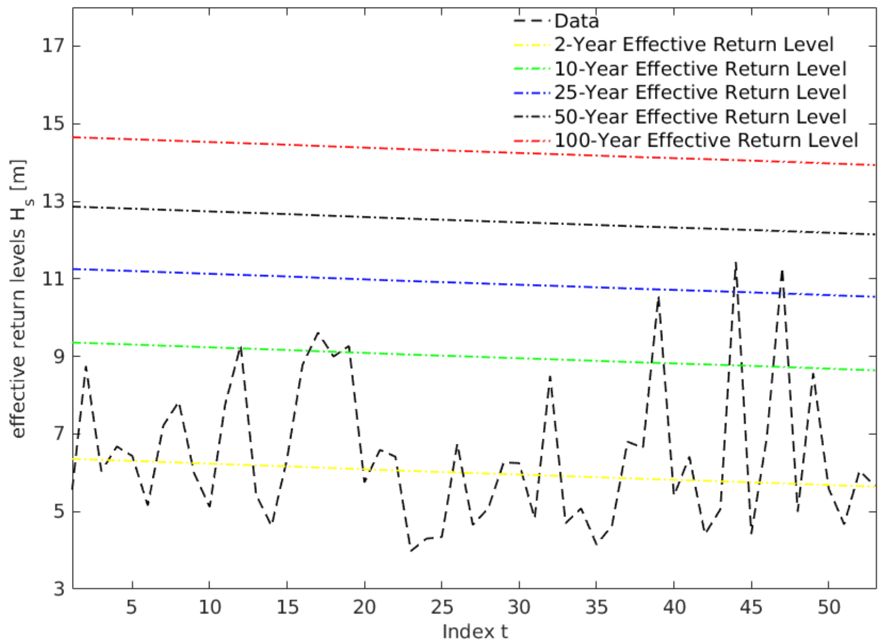

Figure 5.16: Effective return levels at location A. The red dashed line refers to 100-year return levels, black dashed line to 50-year return levels and to annual maxima H_S values, blue dashed line to 25-year return levels, green dashed line to 10-year return levels and yellow dashed lined to 2-year return levels.

The opposite behavior occurs at location B as shown in Figure 5.17, where an increasing trend (albeit weak) in the annual maxima of wave height distribution slightly affects the effective return levels. Locations A and B alone are not particularly significant, as other locations exhibit stronger intensity trends. However, this will be further clarified in Section 5.5.

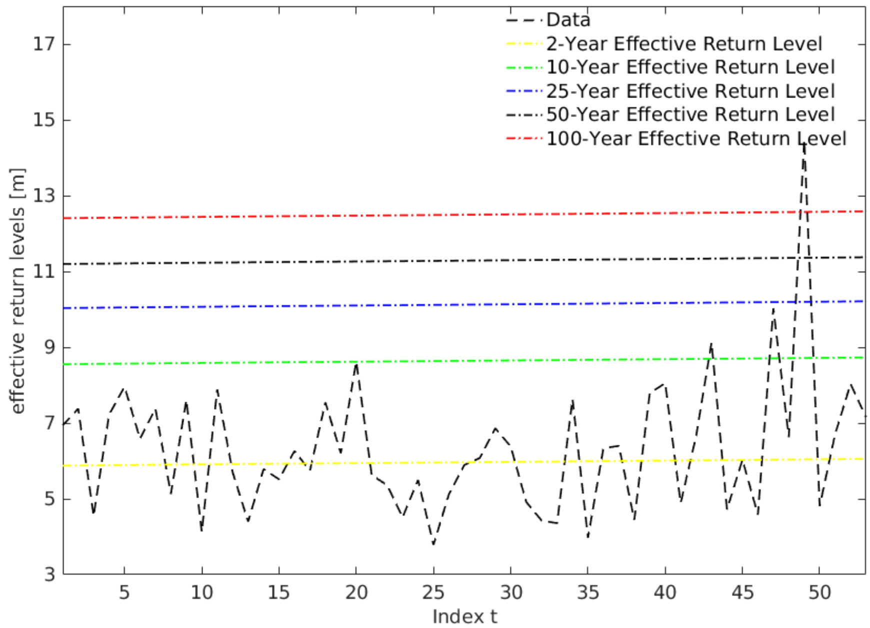

Figure 5.17: Effective return levels at location B. The red dashed line refers to 100-year return levels, black dashed line to 50-year return levels and to annual maxima H_S values, blue dashed line to 25-year return levels, green dashed line to 10-year return levels and yellow dashed lined to 2-year return levels.

The neglection of proper typhoon-simulated events implies a different scenario in terms of effective return levels at locations A and B. Nonetheless, the Holland model allows to better capture the peaks during extreme events, therefore giving rise to higher annual maximum values of H_S. For reference, see Figures 5.18 and 5.19.

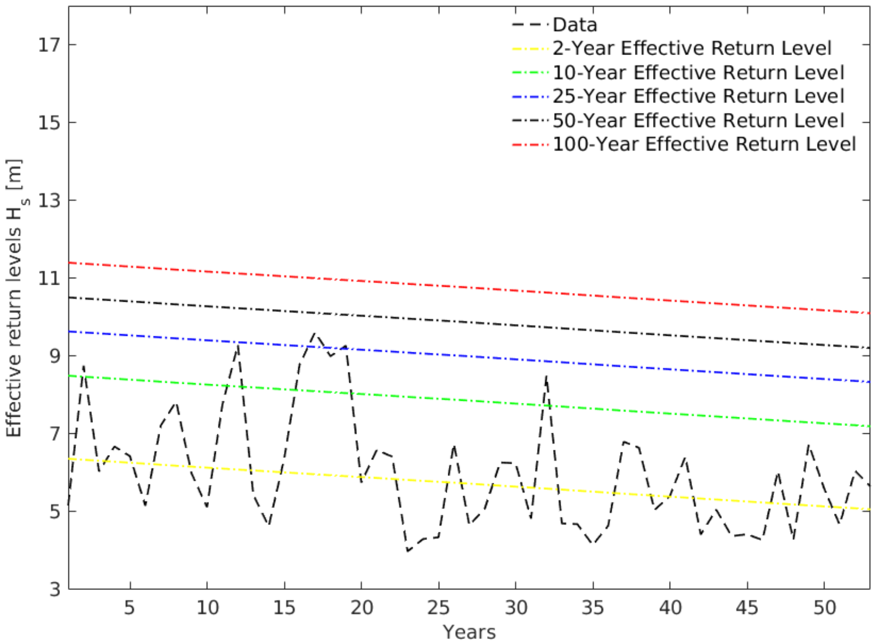

Figure 5.18: Effective return levels at location A. The red dashed line refers to 100-year return levels, black dashed line to 50-year return levels and to annual maxima H_S values, blue dashed line to 25-year return levels, green dashed line to 10-year return levels and yellow dashed lined to 2-year return levels. The plot refers to the hindcast data that does not include the Holland formulation.

The annual maximum values of H_S in Figure 5.18 demonstrate that the omission of the Holland model leads to an underestimation of peak wave heights. This systematic underestimation produces a negative trend with a significantly lower magnitude than the one observed in Figure 5.16.

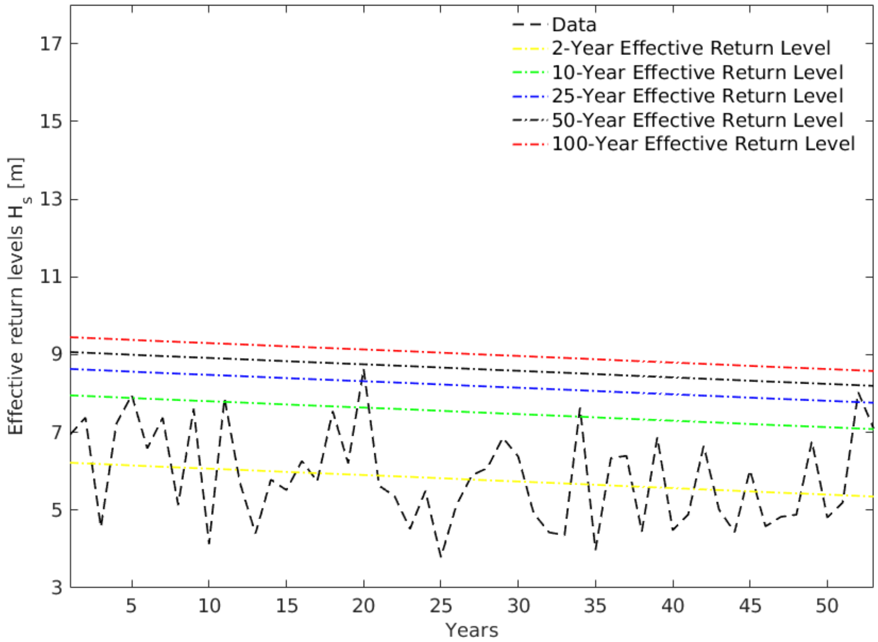

Figure 5.19: Effective return levels at location B. The red dashed line refers to 100-year return levels, black dashed line to 50-year return levels and to annual maxima H_S values, blue dashed line to 25-year return levels, green dashed line to 10-year return levels and yellow dashed lined to 2-year return levels. The plot refers to the hindcast data that does not include the Holland formulation.

The impact at location B is more pronounced. While the Holland model produces a weakly positive trend, its omission results in a negative one, effectively reversing the trend's sign.

5.5 The role of extreme events on wave height trends

A core part of this work is based on the inclusion of extreme events, in this case typhoons, simulated with the Holland parametric model. Since the NEVA framework is applied to annual maxima of significant wave heights, proper simulations of typhoon wind and pressure fields can result in more precise annual maxima values. The inclusion of typhoons results in less pronounced negative trends in the upper region of the domain, specifically in the area between the Philippines, Taiwan, and the Great Bay Area, occasionally giving rise to positive trends when the α value reaches 80%. However, the positive trends observed in the southern part of the domain, longitudes 110 E°- 115 E° and latitudes 3 N°- 14 N°, do not appear to be affected by the application of the Holland model. This is because most of the typhoon tracks considered in the analysis mainly pervade the upper part of the numerical domain (see Figure 3.1 for reference).

As stressed before, the non-stationary return levels proposed in Section 5.3, Figure 5.9, were also replicated for the dataset not accounting for extreme events (CH dataset). Figure 5.20 shows the differences between the return level estimations calculated with the two different datasets just mentioned. The regions colored in red suggest that the inclusion of typhoons induced an increase in the return level estimates, while blue regions indicate a decrease in the return level estimates. Panel a) shows the differences in 25-year effective return levels during the period 1970-2050. It can be seen that the largest positive differences reach about 4.5 to 6 m, especially between 15 N° - 22 N° and 110 E° - 120 E°.

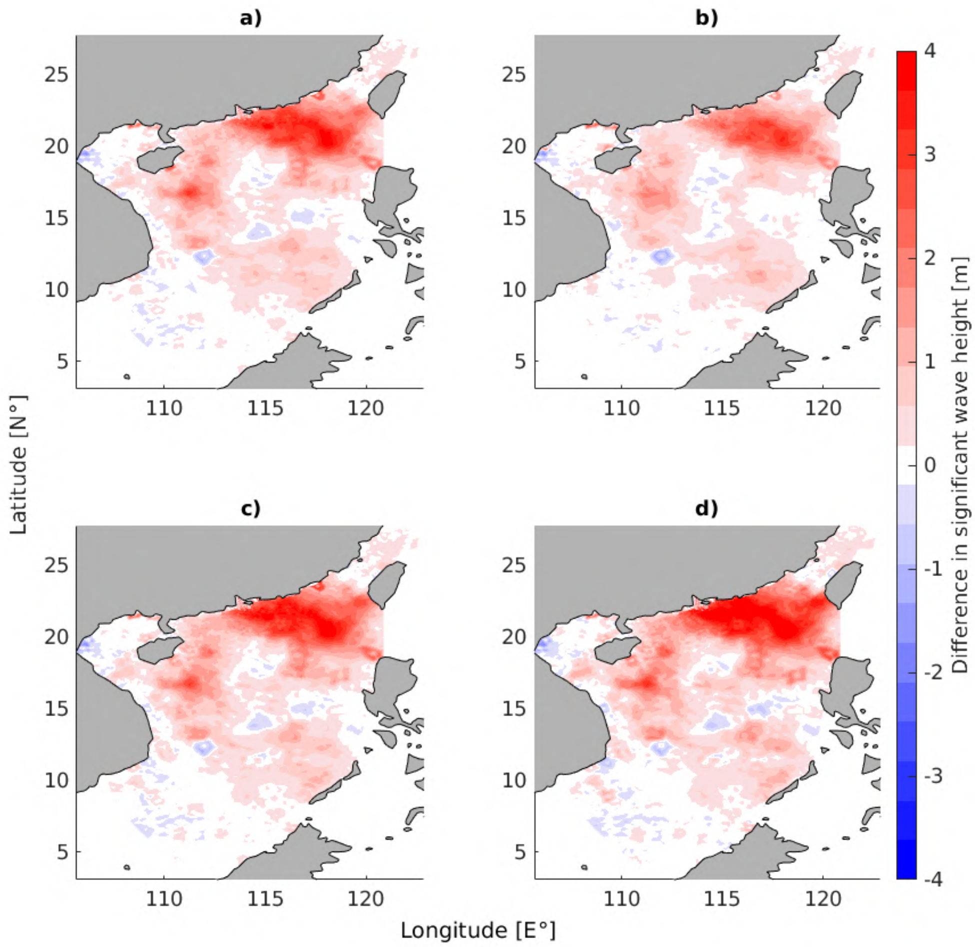

Figure 5.20: Differences between 25-year return level estimates (approaches a–d in Figure 5.9) with and without the inclusion of Holland-simulated typhoons.

Areas in proximity of the Chinese and Vietnamese coasts mostly exhibit positive differences that range between 2 and 4 m. Minimal variations mostly appear in the southwestern part of the SCS, a region characterized by less frequent typhoon activity.

Regarding panel b), it is observed that the spatial patterns of differences present minimal changes compared to those in panel a). However, the magnitude is generally reduced with the largest positive differences in the range 3.5 to 4 m and average increases across the domain of around 1 m. Panels c) and d) show two different future projections of non-stationary 25-year return levels. Here, the incorporation of extreme events lead to differences that exceed values of 6 m in some cases, particularly in the central South China Sea. Panel d) shows some regional differences, compared to panel c), off the coast of Vietnam and in proximity of the Luzon strait.

In general, the implementation of the Holland model results in an increase by up to 2-3 meters in the non-stationary return levels. The region around $\sim$20 N° and $\sim$115 E°, highly influenced by typhoon activities, shows the most significant surge. This is evident in Figure 3.1, which shows the typhoon tracks of the extreme events simulated in this work. The differences arising by the comparison of the two approaches highlight the importance of considering typhoon dynamics when estimating non-stationary return levels. Neglecting a proper inclusion of typhoons could result in severe underestimations (up to 20% - 30%) of significant wave heights used in coastal structure design, especially in regions where typhoon activity is dominant.

We now reconsider the two locations (A and B) to show the differences between the two datasets. As mentioned earlier, location A is characterized by a negative trend of about 1.3 cm/year while location B is characterized by an upward trend of about 0.97 cm/year. If the Holland model was not considered in the analysis, the trends in annual maxima of H_S would be -3.19 cm/year and -2 cm/year (for locations A and B, respectively). As shown in Figure 5.12, the weakening of the negative trend magnitude at location A also resulted in higher non-stationary return levels. The estimates corresponding to the 50-year annual

H_S maxima (ensemble median - red dashed lines) in panels (a-c) were originally 9.87 m, 7.95 m and 6.84 m, respectively. As a result, these estimates have now increased to 12.52 m, 11.51 m, and 10.90 m in Figure 5.12. Similarly to location A, location B also presented enhanced values of non-stationary return levels across all panels in Figure 5.13.

Finally, Figure 5.16 and Figure 5.17 allow to have a complete understanding of the dynamics at locations A and B. In the latter location, the inclusion of typhoons shows that the trend has become positive and therefore, the effective return levels now increase over time, always maintaining a constant probability of occurrence. For instance, if the effective return level corresponding to a 100-year event during 1970-2020 was 8.63 m for the CH dataset, it now becomes 12.57 m in Figure 5.17.

Chapter 6

Multifractal detrended fluctuation analysis of significant wave heights in the SCS

The application of multifractal detrended fluctuation analysis (MF-DFA) to significant wave height time series reveals distinct scaling properties in the wave climate of the South China Sea (SCS), as detailed below. As mentioned in Section 3.6, the analysis focuses on the q-th order fluctuation function $F_q(s)$ (calculated with Equation 3.51), in order to identify knee points and depict typical time scales. In particular, the scaling behavior of the fluctuation functions is determined by analyzing the log-log plot of $F_q(s)$ for $q = 2$ across different time scales s. An example of the resulting fluctuation function at a representative location is shown in Figure 6.1. As illustrated in the figure, three distinct knee points are visually identifiable, each corresponding to dominant temporal scales in the wave height time series: $log(s) \sim$ 2.28 $\sim$ 8 days, $log(s) \sim$ 3.4 $\sim$ 3.5 months, $log(s) \sim$ 4.1 $\sim$

1.5 years.

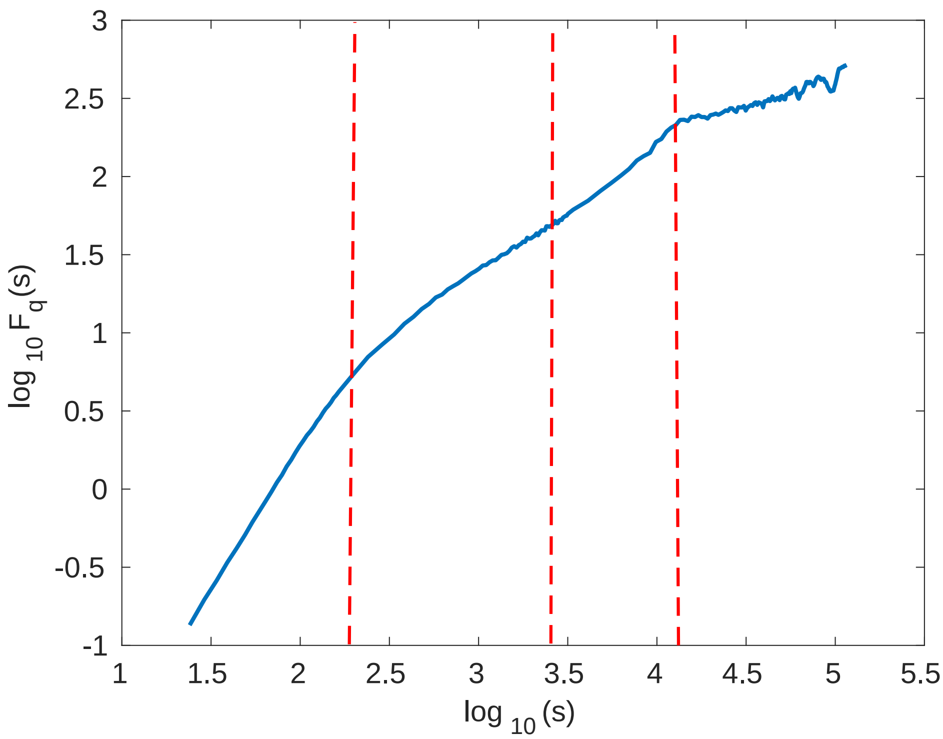

Figure 6.1: Example of a log-log plot of the fluctuation function $F_q(s)$ for $q = 2$ versus time scale s for a generic location.

The behavior shown in Figure 6.1 is representative for the majority of the nodes of the study area: each node generally exhibits three distinct knee points, indicating the presence of multiple scaling regimes: short-term (e.g., diurnal to synoptic), intermediate (e.g., seasonal), and long-term (e.g., interannual).

Figure 6.2 shows the time scales at which the knee points occur. Spatial patterns show higher values in the northern SCS, likely due to greater variability from monsoons and typhoons, while southern areas display lower values, indicating more stable equatorial influences.

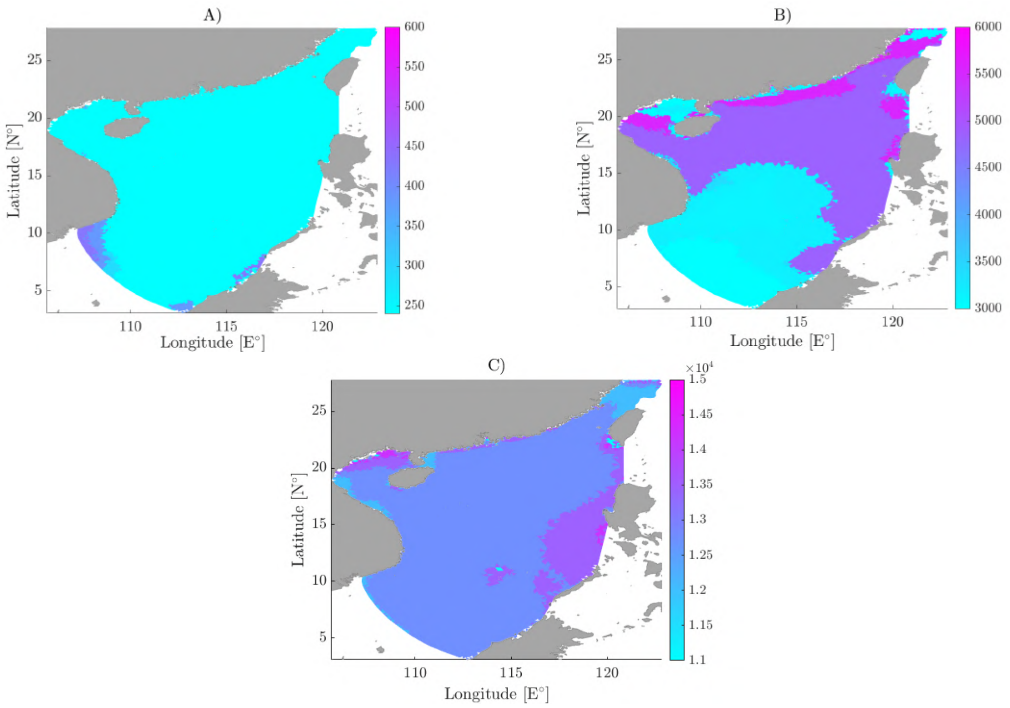

Figure 6.2: Time scales expressed in hours associated with the three knee points for $q = 2$. Panels (A), (B) and (D) show the first, second and third knee point, respectively.

In particular, Panel (A) depicts the shortest identified time scale, with values ranging from approximately 240 hours (dominating time scale) to 500 hours (in a few areas in the southern part of the domain). This scale corresponds to synoptic weather systems, such as frontal passages, short-term storms, or mesoscale atmospheric disturbances, which dominate wave height fluctuations on weekly to biweekly intervals (Ozger 2011). Literature on DFA/MF-DFA of wave heights in the SCS identifies similar crossovers around 4–11 days, where fluctuations transition from Brownian noise-like (integrated random processes) to persistent long-range correlations, aiding in short-term forecasting (Cabrera and Rodríguez 2011).

Intermediate knee points presented in Panel (B) exhibit values corresponding to approximately 4.8 months ($\sim$ 3500 hours) in the southern and central SCS, including the area enclosed by Hainan Island, increasing to 6.8–7.5 months ($\sim$ 5000–5500 hours) in the central and northern portions of the domain. This time scale aligns with seasonal cycles, encompassing the SCS monsoon regimes (northeast winter monsoon, between November and March; southwest summer monsoon, between May and September) and the peak typhoon season (July–October).

Finally, Panel (C) identifies annual to inter-annual variability with longer time scales of about 1.4 to 1.7 years. This longest scale likely captures inter-annual phenomena, suggesting a possible link to El Niño-Southern Oscillation (ENSO) influences or multi-year monsoon shifts, affecting wave climate over 1–2 years (F.-H. Xu and Oey 2015; F. Peng et al. 2024). In the context of MF-DFA, long-term crossovers ($>$ 100 days) often indicate white noise-like randomness, reflecting decoupled processes at extended scales. These knee points highlight the multifractal nature of SCS wave dynamics, influenced by typhoons, monsoons, and bathymetry.

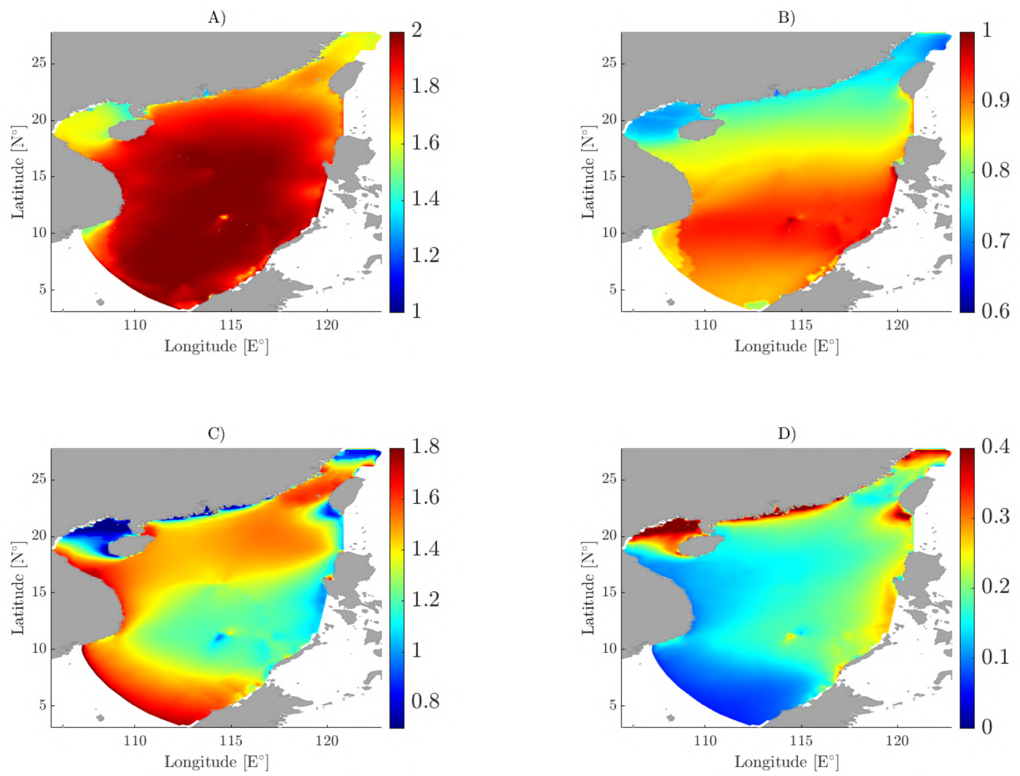

Figure 6.3: Hurst exponents identified from the log-log plots of $F_q(s)$ versus s. Panel (A) refers to the value of H prior to the first knee point; Panel (B) refers to the value of H between the first and the second knee point; Panel (C) refers to the value of H between the second and the third knee point; Panel (D) refers to the value of H after the last knee point.

Following the identification of knee points in the MF-DFA fluctuation functions (as discussed in Section 3.6), the three crossovers divide the log-log plots of $F_q(s)$ versus s into four distinct scaling regimes for each node in the SCS domain. The slope within each regime corresponds to the generalized Hurst exponent $h(q)$ (see Equation 3.54 and Equation 3.51). For the specific case of $q = 2$, this exponent equals the classical Hurst exponent, i.e., $h(2) = H$ (Equation 3.53). As briefly introduced in Section 3.6, higher H values indicate stronger persistence, often linked to structured forcing like monsoons or typhoons, while lower values indicate anti-persistent behavior and point to more random or dissipative processes (H. Liu et al. 2023a).

Figure 6.3 illustrates the spatial distribution of these slopes across the four regimes, revealing pronounced regional variability. Panel (A) shows the predominance of Hurst exponents greater than 1.8 in the majority of the SCS, with the exception of the north-eastern SCS and the waters enclosed by Hainan Island where slopes are milder. These elevated slopes ($H > 1.5$) suggest super-persistent or non-stationary behavior at short time scales (e.g., hours to days, based on the first knee point around 240–500 hours).

Panel (B) shows values of H typically between 0.5 and 1.0 indicating persistent long-range correlations, stronger in the southern SCS.

Panel (C) shows more variety in slopes, with values ranging from about 0.8 (in the northern coastal areas and close to the boundary) to 1.8 (especially in the South, along the Vietnamese coast and between Taiwan and China). Here, H values greater than 0.5 indicate persistent behavior at seasonal to annual scales (up to about 1.4 years), with northern values approaching 1.8 suggesting strong long-range correlations or even non-stationarity.

Finally, Panel (D) shows minimal spatial variation, with only sporadic high values. Slopes are generally low and ranging from around 0.1 in the South to 0.4 in isolated northern patches. $H < 0.5$ imply anti-persistent behavior at inter-annual to decadal scales (> 12,000 hours or > 1.4 years). This could reflect the influence of large-scale climatic oscillations like ENSO or Pacific Decadal Oscillation, which introduce variability but disrupt long-term persistence through regime shifts.

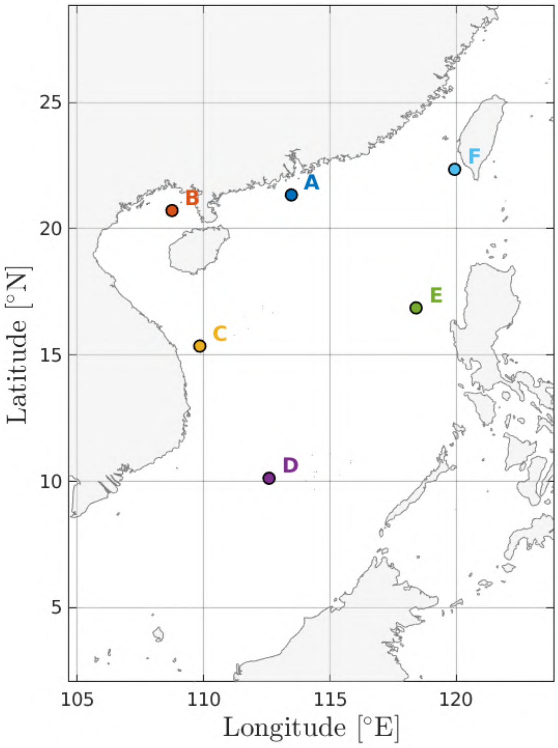

Figure 6.4: Map showing the six different locations considered for the detailed analysis.

The multifractal properties are analyzed at six distinct locations, indicated in Figure 6.4, using distinct multifractal measures: the generalized Hurst exponent $h(q)$ (Equation 3.52), the multifractal scaling exponent $\tau(q)$ (Equation 3.56), the fractal dimension $D(q)$ (Equation 3.57), the singularity spectrum $f(\alpha)$ and the singularity exponent α (Equations 3.58). Firstly, the log-log plots of the q-th order fluctuation functions $F_q(s)$ are shown for all the locations (Figure 6.5) and for q values ranging from -20 to 20. A consistent pattern emerges: curves corresponding to negative q values display markedly higher scatter and noise compared to positive q, as expected in MF-DFA. This behavior arises because negative moments emphasize small-amplitude fluctuations, which are more sensitive to local irregularities and measurement noise in the time series.

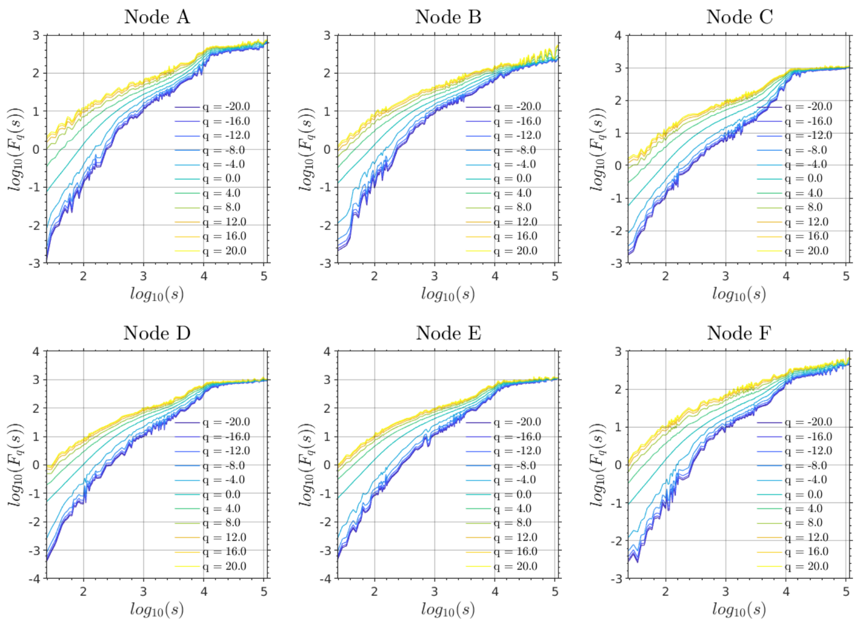

Figure 6.5: Log-log plots of the raw q-th order fluctuation function $F_q(s)$ versus time scale s for the six locations.

Figure 6.6 shows the corresponding linear curve fitting results. Starting from the linear curve fitting of $F_q(s)$, more detailed information are then calculated and shown in Figure 6.7. It can be seen from Panel (B) that the generalized Hurst exponent $h(q)$ decreases monotonically with increasing moment order q (from -20 to 20) for all locations: this dependence on q confirms multifractal scaling, as monofractal series would yield constant $h(q)$. Northern sites (A, B; red/orange curves) show steeper declines and higher $h(q)$ for negative q, suggesting stronger persistence in small-scale variability, possibly linked to frequent synoptic disturbances like cold surges. In contrast, southern locations (E, F; blue/green) exhibit flatter curves, indicating weaker multifractality and more anti-persistent behavior

($h(2) \approx 0.6$–0.8), reflective of stable wind-wave regimes. At $q = 2$, $h(2) = H > 0.5$ across sites implies overall long-range correlations, consistent with typhoon-modulated wave persistence in the SCS.

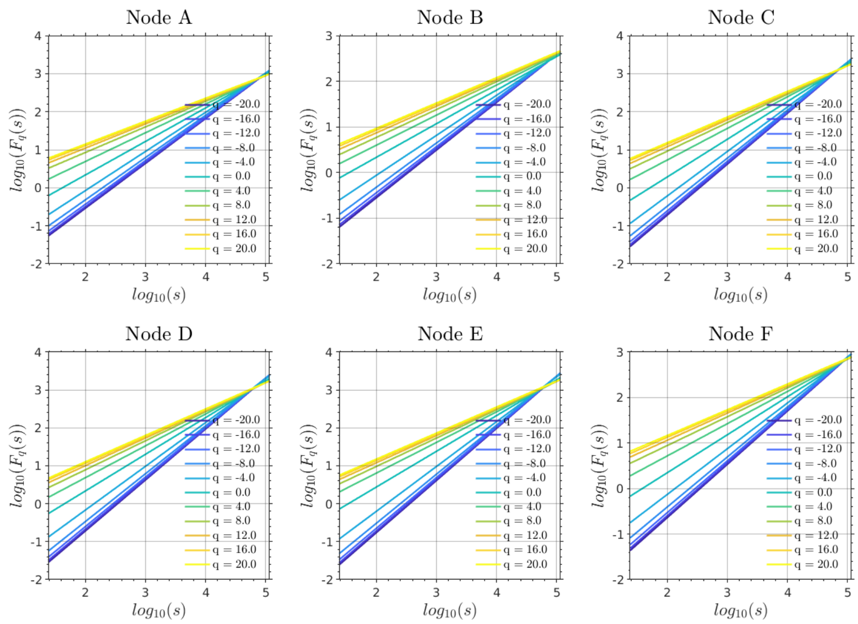

Figure 6.6: Log-log plots of the linear q-th order fluctuation function $F_q(s)$ versus time scale s for the six locations.

The singularity mass exponent $\tau(q)$ in Panel (C) displays a nonlinear, concave behavior, transitioning from negative values at low q to positive at high q. Deviations from linearity underscore multifractality, with the concavity measuring the degree of heterogeneity in scaling (G. Liu et al. 2019). Northern curves (A, B) are more pronounced, indicating greater intermittency in wave height fluctuations, attributable to typhoon-induced extremes that amplify large-q moments. Central and southern sites (C–F) show milder nonlinearity, suggesting homogeneous scaling dominated by regular monsoon patterns.

Panels (D) and (E) show the generalized multifractal dimension $D(q)$ versus

q and $h(q)$, respectively. It can be seen that $D(q)$ shows a bell-shape behaviour with a maximum value of 1 at q=0, with northern locations (A, B) showing the widest spread, where $D(0) \approx 1$ and lower $D(q > 0)$ reflect sparse, typhoon-driven large fluctuations, indicative of multifractal intermittency. Southern sites (E, F) maintain higher, more uniform $D(q)$, suggesting stable regimes. Plotting $D(q)$ against $h(q)$ reveals inverted parabolic curves peaking at $h(q) \approx 0.8$–1.0, with broader arches in the north, highlighting enhanced multifractality and diverse fluctuation strengths tied to extreme wave events.

Finally, Panel (F) displays the singularity spectrum $f(\alpha)$. It is characterized by bell-shaped curves peaking at 1, which is the monofractal limit and spanning α values between 0.6 and 0.8. The width of the bell-curve is identified by $\Delta\alpha = \alpha_{\text{max}} - \alpha_{\text{min}}$ and quantifies multifractality strength. The northern sites (A,B) are characterized by $\Delta\alpha \sim 0.6$ and therefore exhibit narrower spectra if compared to the southern sites (E,F). Broader spectra imply richer multifractal structures, where low α corresponds to smooth, persistent regions, and high α to irregular, extreme-driven singularities.

Overall, these results affirm the multifractal complexity of SCS H_S series, with southern locations displaying stronger multifractality due to climatic extremes, complementing non-stationary EVA findings on wave trends (Luo and Zhu 2019).

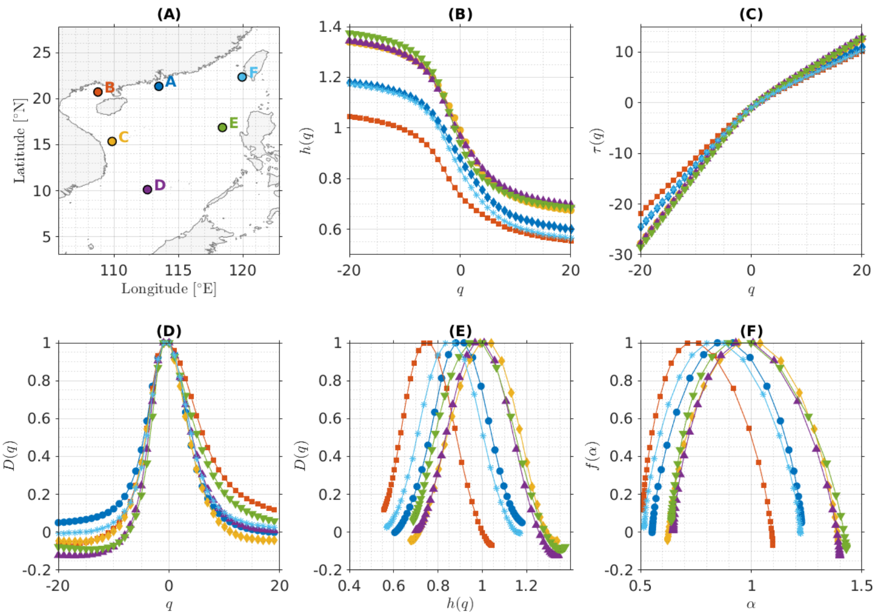

Figure 6.7: The following panels illustrate key MF-DFA outputs: Panel (A) location of the six nodes; Panel (B): generalized Hurst exponent $h(q)$; Panel (C): mass exponent $\tau(q)$; Panels (D) and (E): generalized fractal dimension $D(q)$; Panel (F): singularity spectrum $f(\alpha)$.

Chapter 7

Mangrove-induced wave dissipation in the Mai Po Nature Reserve, Hong Kong

While the preceding chapters focus on basin-scale wave dynamics in the South China Sea — encompassing hindcasting, trend analysis of extreme significant wave heights, and multifractal characterization of wave variability — the present chapter addresses a more localized, site-specific question. Although the wave conditions used in the following analysis are derived from the high-resolution hindcast results presented earlier, this chapter is not intended as a direct continuation of the regional-scale investigations. Instead, it constitutes an independent but complementary exercise aimed at evaluating the potential role of mangrove vegetation in wave dissipation under realistic nearshore conditions in Hong Kong. Specifically, this chapter presents a case study at the Mai Po Nature Reserve, where the SCHISM-WWMIII model is applied to quantify wave height reduction induced by vegetation. The analysis serves as a preliminary assessment of nature-based coastal protection in a subtropical estuarine environment exposed to both regular and extreme (typhoon-driven) wave conditions; the results are related to the scenarios and sets of simulations described in Section 3.7.

Firstly, the water levels have been validated against the tidal level observation at the Tsim Bei Tsui station managed by the Hong Kong Observatory. A signal of about one month has been used for the validation. The comparison between the observed water levels and the modeled one is shown in Figure 7.1

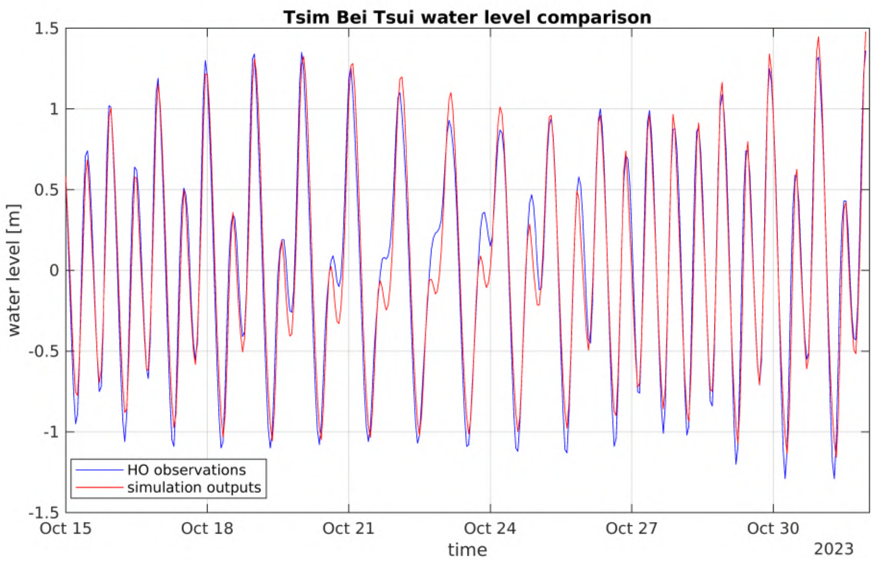

Figure 7.1: Water level validation at Tsim Bei Tsui station: comparison between signals.

The statistics for the quantitative comparison are summarized in the Taylor diagram shown in Figure 7.2. The correlation between the two signals is about 0.97 with a RMSD of about 0.15 m, confirming the good agreement between the model outputs and the observations.

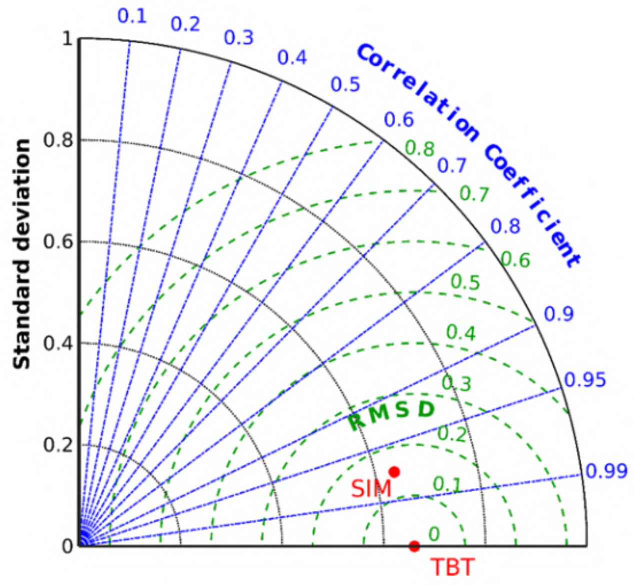

Figure 7.2: Water level validation at Tsim Bei Tsui station: Taylor diagram.

The distributions of the significant wave height for all cases simulated are shown in the following Figures. The results for incident waves with T_r = 10 years for the minimum and maximum drag coefficients are reported in Figure 7 and Figure 10. It can be seen that the effect of increasing resistance is hardly detectable. Another important point is that the waves are rapidly dissipated along the direction of propagation from the inlet of the bay towards the end of the bay. The main effect of attenuation is due to the bottom resistance since, even at high tides, the water conditions remain always extremely shallow. Similar behavior is found for more extreme wave conditions, T_r = 50 years see Figure 8 and Figure 11 or T_r = 100 years (see Figure 9 and Figure 12). Notably, the waves predicted around the Mai Po reserve are of order of a few centimeters, qualitatively in agreement with the observation of the water level gauges.

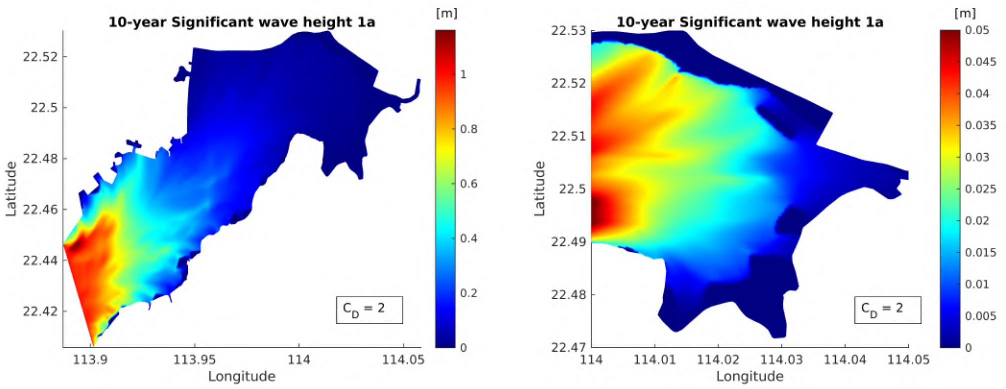

Figure 7.3: Distribution of significant wave height: (left panel) over the entire bay; (right panel) zoom around the Mai Po reserve. Note that the scale in the right panel has been reduced to a maximum of 0.05 m. Simulation parameters: T_r = 10 years and C_{dv} = 2.

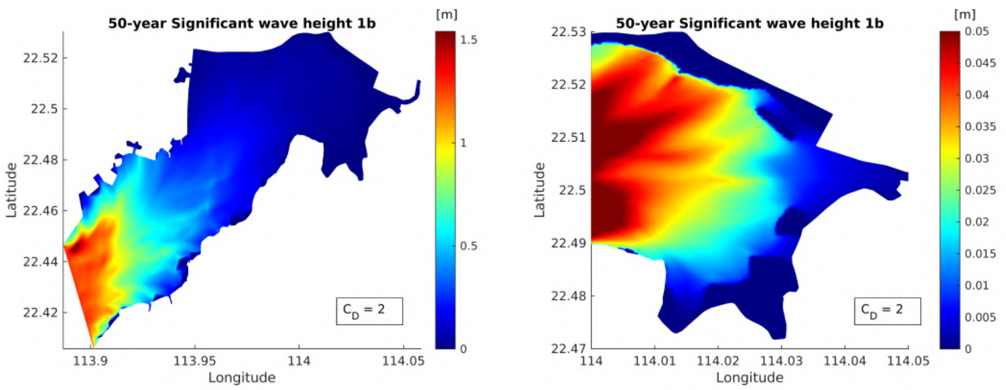

Figure 7.4: Distribution of significant wave height: (left panel) over the entire bay; (right panel) zoom around the Mai Po reserve. Note that the scale in the right panel has been reduced to a maximum of 0.05 m. Simulation parameters: T_r = 50 years and C_{dv} = 2.

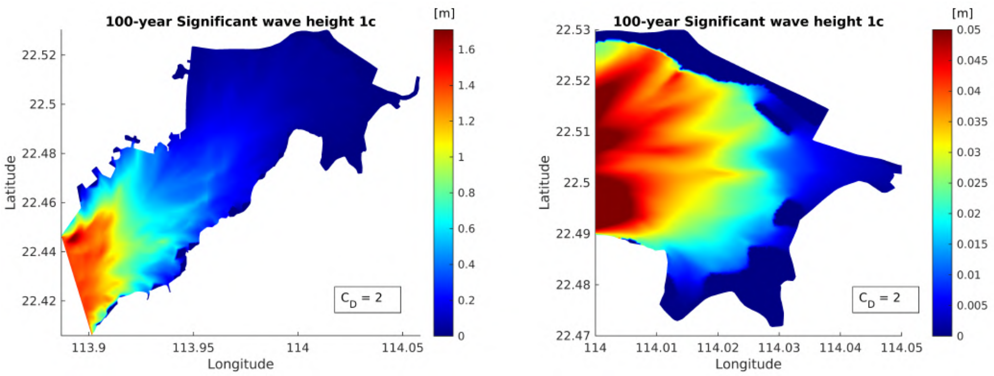

Figure 7.5: Distribution of significant wave height: (left panel) over the entire bay; (right panel) zoom around the Mai Po reserve. Note that the scale in the right panel has been reduced to a maximum of 0.05 m. Simulation parameters: T_r = 100 years and $C_{dv} = 2$.

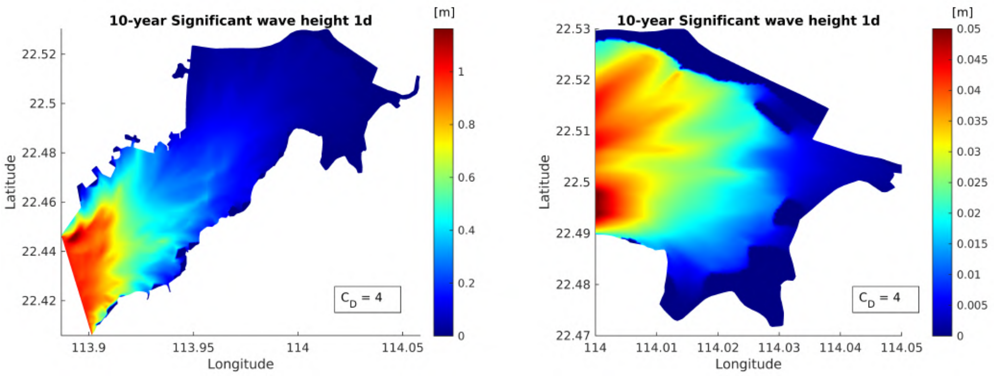

Figure 7.6: Distribution of significant wave height: (left panel) over the entire bay; (right panel) zoom around the Mai Po reserve. Note that the scale in the right panel has been reduced to a maximum of 0.05 m. Simulation parameters: $T_r = 10$ years and $C_{dv} = 4$.

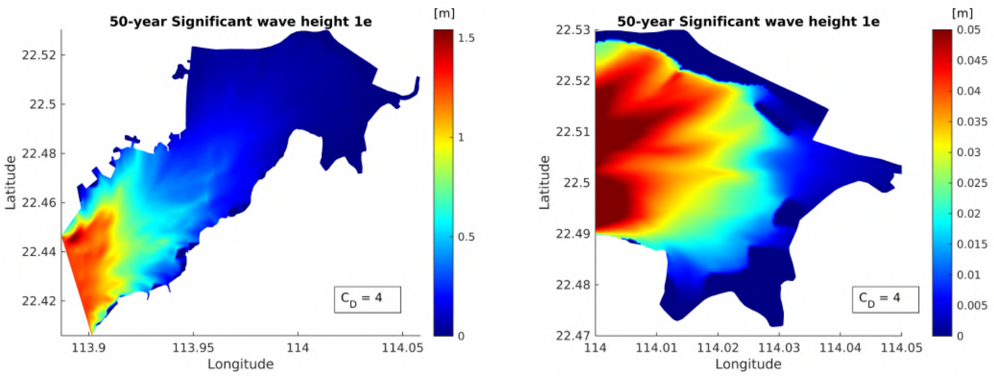

Figure 7.7: Distribution of significant wave height: (left panel) over the entire bay; (right panel) zoom around the Mai Po reserve. Note that the scale in the right panel has been reduced to a maximum of 0.05 m. Simulation parameters: T_r = 50 years and C_{dv} = 4.

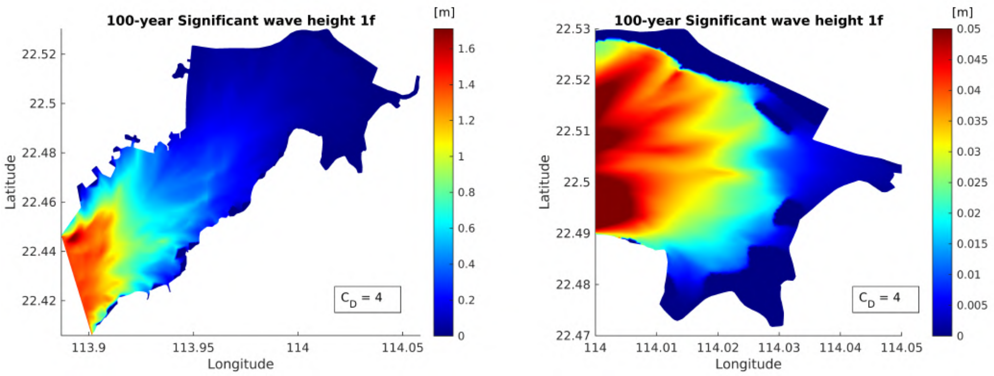

Figure 7.8: Distribution of significant wave height: (left panel) over the entire bay; (right panel) zoom around the Mai Po reserve. Note that the scale in the right panel has been reduced to a maximum of 0.05 m. Simulation parameters: T_r = 100 years and C_{dv} = 4.

To better understand the role of the vegetation, wave height profiles were extracted along two representative transects, as shown in Figure 7.9. Studying the distributions of significant wave height (H_S) along the transects helps in understanding the wave attenuation along two main directions, along the bay and across the bay where the mangroves are located.

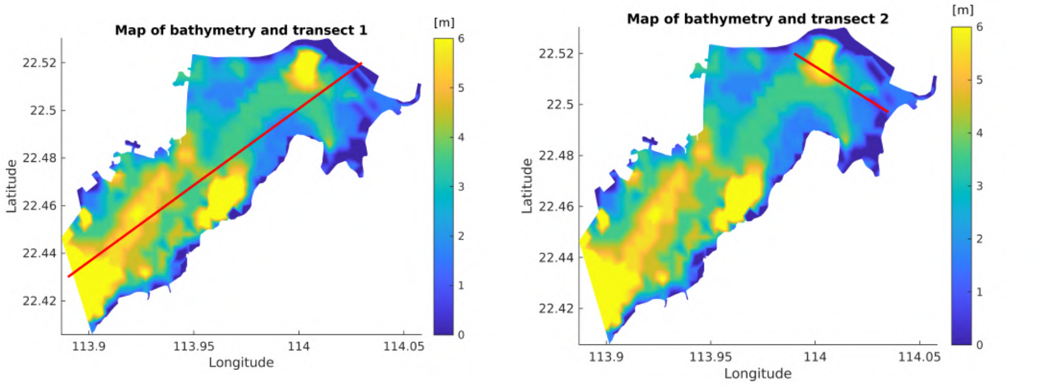

Figure 7.9: Maps showing bathymetry contours and transects. The red lines indicate the position of the transects: (left panel) along the major axis of the bay; (right panel) along the mangrove forest.

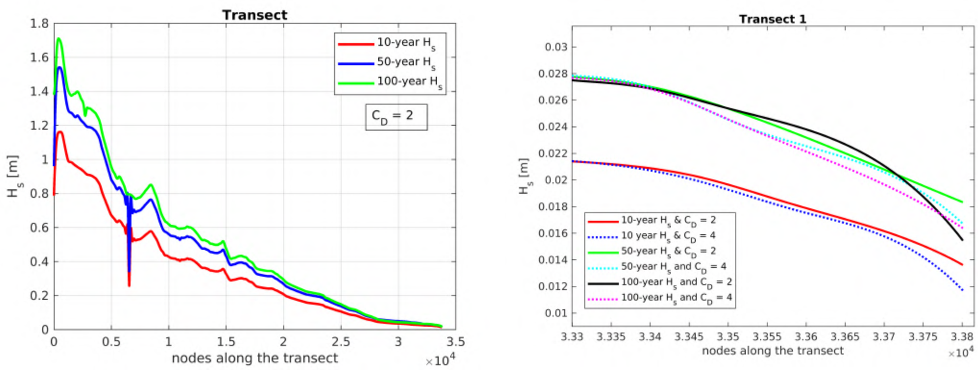

Figure 7.10: significant wave height profiles for the three return periods (10, 50, 100) along transect 1. (left panel) profile along the entire transect. The results shown are for the case $C_{dv} = 2$. The results obtained with higher drag coefficient are indistinguishable at this scale; (left panel) zoom corresponding to the red square of panel (right panel) where the comparison between the two values of the vegetation drags is shown. Solid lines correspond to $C_{dv} = 2$ and dashed lines correspond to $C_{dv} = 4$.

Figure 7.10 shows the comparison among the profiles of H_S for the three return periods along transect 1. Panel (a) shows only the results for the lower drag coefficient since the case with $C_{dv} = 4$ is almost indistinguishable expect for minor differences at the end of the transect. Indeed, panel (b) shows the zoom corresponding to the red square, where the impact of the vegetation coefficient appears clearly. The increased coefficient results in a slightly lower wave height. However, the attenuation generated by the mangrove forest seems to be relatively low compared to the overall attenuation due to the shallowness of the bay. In fact, panel (a) suggests that the bottom friction coefficient is extremely efficient in attenuating the waves, even in the worst scenario of water level corresponding to the highest tide. The wave height is attenuated from about 1.2-1.7 m (depending on the return period) to a few centimeters during its propagation along the bay.

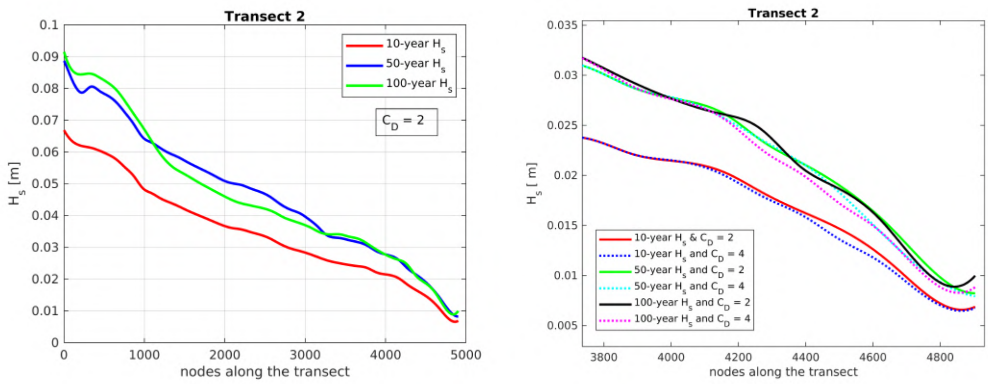

Figure 7.11: significant wave height profiles for the three return periods (10, 50, 100) along transect 2. (left panel) profile along the entire transect. The results shown are for the case C_{dv} = 2. The results obtained with higher drag coefficient are indistinguishable at this scale; (left panel) zoom corresponding to the red square of panel (right panel) where the comparison between the two values of the vegetation drags is shown. Solid lines correspond to C_{dv} = 2 and dashed lines correspond to C_{dv} = 4.

Similar results are recovered along the cross bay transect, shown in Figure 7.11, (left panel) for the whole transect and (right panel) for the zoomed area (red square). Compared to the simulation with no vegetation (C_{dv} = 0) the presence of the mangrove leads to a reduction of the wave height of the order of a few centimeters. Doubling the effect of the mangrove using a higher drag results in an increased attenuation of the order of millimeters. Finally, the particular location and geometry of Deep Bay is the major cause for wave attenuation, the energy dissipation due to bottom friction is the main driver of wave attenuation. However, it is undeniable that the mangrove forest generates a wave attenuation if considered in percentage of the local incident wave, but the absolute reduction is limited to centimeters.

A series of other simulations were devoted to understanding the effect of the vegetation on the propagation of storm surge generated during extreme events. For this matter, the passage of typhoon Hato was chosen as a representative event. The simulations were conducted reproducing the typhoon using the strategy commonly used to numerically simulate extreme events, see for example Vogt et al. (2024), using the analytical approach suggested by G. Holland (2008) who suggested a formula to describe wind and pressure fields starting from the observations of the main characteristics of the typhoons. The computed storm surge has been compared to the water level registered at the Tsim Bei Tsui station. The results are presented through water level plots during the typhoon at different locations along Deep Bay, from the open boundary to the inner part of the bay and within the forest. The locations of the numerical water level gauges are shown in 7.12.

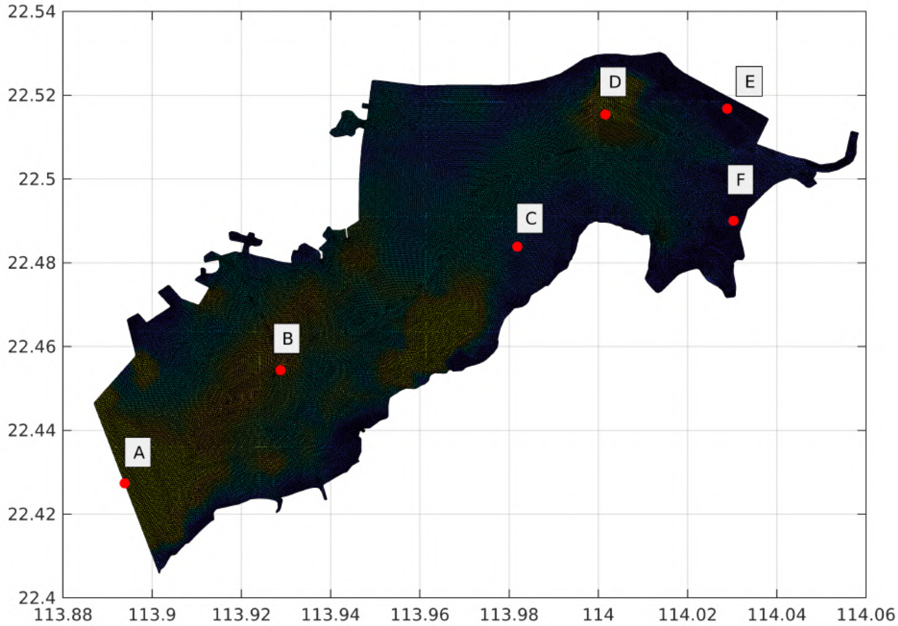

Figure 7.12: Position of the locations considered for the water level analysis.

Figure 7.13 shows the water level signals recorded during the simulations in the six stations (from A to F) for the three simulations. For the first four stations (A, B, C and D) clearly the effect of the mangrove forest is absent. The oscillations in the signals of panels (b, c, d) are merely numerical oscillations. Panel (e) and (f) are the most representative for the present discussion. The results suggest that the presence of the mangrove forest can reduce the water levels during a storm surge event. Indeed, the levels are reduced by about 10-15 cm. Our results seem in contrast to the simulations recently published (De Dominicis et al. 2023) where the authors showed a more effective reduction in water levels. However, the uncertainties of geometrical information (bathymetry) and on the real distribution of mangrove trees can be easily induce a large scatter in the results. The effect of the mangroves in undeniable, but a correct estimation using a numerical model would require a much more detailed collection of data.

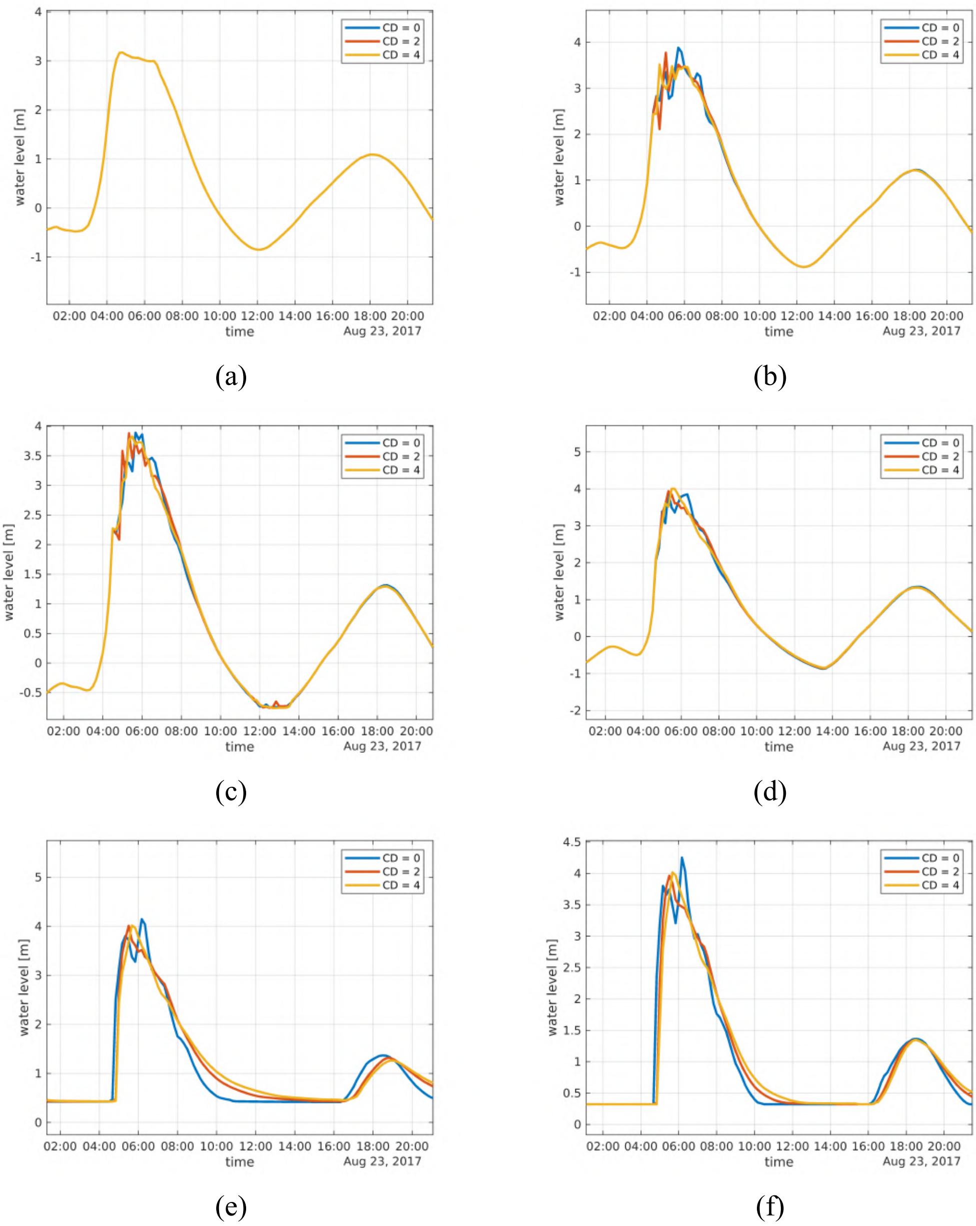

Figure 7.13: Time signals of the water levels recorded in the stations from A to F shown in Figure 7.12, the panel letter corresponds to the station label.

Chapter 8

Final remarks and Conclusions

8.1 Limitations of the study

The multi-scale investigation of waves in the South China Sea (SCS) reveals several limitations across its methodologies and findings. The SCHISM-WWMIII hindcast, despite its high resolution (0.008°), relies on a 2D framework that may inadequately represent complex 3D currents and vertical mixing, potentially skewing nearshore wave predictions, especially during extreme events. ERA5 wind bias corrections, while effective, are constrained by spatial resolution (0.25°) and hourly intervals, leading to potential underestimation of localized wind bursts and typhoon asymmetries, as evidenced by $RMSD$ increases ($\sim$ 1.207 m) at higher velocities. The Holland model, though effective for 32 typhoon events, assumes idealized storm structures, which may not fully capture real-world complexities like irregular track shifts or multiple storm interactions, limiting its accuracy for atypical typhoons. Moreover, not all the typhoons were simulated because of a lack of continuous storm datasets.

Trend analysis via non-stationary extreme value analysis (NEVA) faces challenges from sparse long-term data, with potential biases from incomplete typhoon records pre-2000, and the model's reliance on Holland-derived trends may overestimate positive shifts (20–30%) in typhoon-affected areas. Return level projections to 2122, based on 95th quantile extrapolations, are extremely sensitive to future climate uncertainties and lack validation beyond current datasets, risking over- or under-prediction (2–6 m differences).

Multifractal detrended fluctuation analysis (MF-DFA) is limited by its dependence on H_S time series quality, with northern SCS's richer multifractality ($\Delta\alpha \sim 1$) potentially exaggerated by noise from sparse typhoon data, while southern stability ($\Delta\alpha \sim 0.5$) may reflect data gaps rather than true dynamics.The estimated wave dissipation by mangroves at Mai Po is limited by the use of simplified vegetation parameters (C_{dv} = 2–4) that omit canopy and root complexity. In this environment, shallow bathymetry is the primary driver of attenuation, confining efficacy estimates to a range of millimeters to centimeters. Consequently, these results may not be directly transferable to sites with deeper bathymetry or higher forest density.

8.2 Future research directions

To advance the SCHISM-WWMIII framework, future studies could incorporate 3D hydrodynamic modeling to better capture vertical mixing and stratified flows, particularly in typhoon-prone areas, integrating higher-resolution bathymetry (e.g., < 50 m) for improved nearshore accuracy. Exploring data-driven enhancements, such as machine learning-based rolling predictions for significant wave heights

(H_S), could refine short-term hindcasts by assimilating real-time satellite and buoy data, as demonstrated in recent global wave models. Additionally, extending hindcast durations beyond 2022 with ensemble climate forcings (e.g., CMIP6 scenarios) would enable probabilistic assessments of wave-current interactions under future warming, focusing on SCS-specific phenomena like monsoon intensification. Building on the Holland model's efficacy, research should expand to ensemble simulations of synthetic typhoons under climate change projections, incorporating uncertainties in storm tracks and intensities via stochastic modeling to quantify compound risks (e.g., typhoon-rainfall interactions). Integrating advanced atmospheric reanalyses (e.g., ERA6) with parametric models could address underestimations in wind fields, while coupling with surge-tsunami models would evaluate multi-hazard impacts in vulnerable regions like the Greater Bay Area. Long-term hindcasts of extreme sea levels, as in recent global studies, could incorporate non-stationary frameworks to predict shifts in typhoon frequency, aiding adaptive coastal planning.

To refine non-stationary extreme value analysis (NEVA), future work should integrate multi-model ensembles (e.g., from CMIP7) for robust projections of H_S trends under varying RCP/SSP scenarios, addressing data sparsity by fusing satellite, buoy, and hindcast datasets for extended records (> 100 years). Exploring hybrid statistical-physical models could better account for covariates like ENSO and sea-level rise, enhancing return level estimates with spatial-temporal dependencies via copula methods. Seasonal and directional trend analyses, incorporating wave spectra, would provide granular insights for offshore energy infrastructure, while validating projections against emerging high-resolution reanalyses could mitigate extrapolation uncertainties.

Extending MF-DFA to multivariate applications, such as joint analysis of H_S with wind speed or sea surface temperature, could uncover cross-correlations in scaling behaviors, using advanced variants like multifractal detrended cross-correlation analysis (MF-DCCA) for directional wave data. Integrating MF-DFA with machine learning (e.g., neural networks for anomaly detection) would enable real-time forecasting of multifractal shifts, particularly in northern SCS where typhoon-driven intermittency is pronounced. Future studies could apply MF-DFA to global datasets for comparative analyses, exploring links to climate indices like PDO, and validating against fractal properties in ocean currents or turbulence for holistic wave climate predictions.

To optimize mangrove-based nature-based solutions (NbS), research should employ high-resolution 3D vegetation models (e.g., resolving root and canopy structures) with field-calibrated drag coefficients, integrating LiDAR-derived bathymetry for accurate dissipation estimates under varying tidal and surge conditions. Long-term monitoring of mangrove health under climate stressors (e.g., sea-level rise, acidification) could quantify adaptive capacity, while hybrid NbS designs (mangroves + artificial reefs) should be tested via coupled hydrodynamic-ecological models for enhanced coastal protection. Global comparative studies on mangrove efficacy, incorporating uncertainty quantification, would inform scalable NbS frameworks, emphasizing restoration strategies in degraded SCS sites like Mai Po.

8.3 Conclusions

This thesis has undertaken a comprehensive multi-scale investigation into wave dynamics in the South China Sea (SCS), integrating advanced modeling techniques, statistical analyses, and ecological assessments to enhance our understanding of wave behavior, extreme events, and coastal protection mechanisms. By addressing key research objectives (ranging from hindcast modeling and extreme value analysis to multifractal characterizations and mangrove-induced wave dissipation) this work provides a holistic framework for assessing wave climates in a region increasingly vulnerable to climate change and anthropogenic pressures. The findings underscore the interplay between atmospheric forcings, oceanographic processes, and natural barriers, offering valuable insights for coastal management, disaster risk reduction, and sustainable development in the SCS.

Central to this study is the validation and application of the SCHISM-WWMIII two-way coupled model, which demonstrates robust performance in simulating wave and current interactions, particularly in nearshore environments. The incorporation of the Holland parametric wind model significantly refines representations of typhoons, leading to more accurate peak significant wave height (H_S) detections and storm surge estimations compared to reliance on ERA5 winds alone. This enhancement is evident in improved statistical metrics, such as correlation coefficients (CC) of 0.780–0.845 for water levels and reduced biases in extreme event simulations. These results affirm the model's utility for high-resolution hindcasts, highlighting the necessity of parametric adjustments to capture localized wind asymmetries and typhoon intensities that global reanalyses may underestimate.

The non-stationary extreme value analysis (NEVA) reveals spatially and seasonally varying H_S trends, with negative trends dominating northern and eastern SCS regions (up to -0.045 m/year) and positive trends emerging in the south (up to +0.019 m/year). Seasonal modulations, particularly stronger positives in winter/spring and negatives in summer/autumn, reflect monsoon and typhoon influences. The Holland model's integration expands areas of positive trends by 20–30% during typhoon seasons, enhancing statistical significance and emphasizing the critical role of extreme events in long-term wave climate evolution. Projections of 25-year return levels, reaching approximately 12 m in central-northwestern SCS under median estimates, indicate potential increases northwestward by 2122 based on 95th quantile extrapolations. Critically, neglecting typhoons leads to underestimations of 2–6 m (20–30%), underscoring the imperative for non-stationary frameworks that account for such drivers to inform reliable risk assessments and infrastructure planning.

The multifractal detrended fluctuation analysis (MF-DFA) uncovers distinct scaling regimes in H_S time series, identifying synoptic (10–21 days), seasonal (5–7 months), and inter-annual (1.4–1.7 years) characteristic time scales. Hurst exponents reveal super-persistent behavior at short scales ($H > 1.8$), persistent correlations at intermediate scales ($0.5 < H < 1.0$, stronger in the south), and mixed persistence with anti-persistent tendencies at longer scales. These insights illuminate the complex, non-linear dynamics of wave fields, providing a foundation for predicting regime shifts and enhancing forecast models through fractal-based approaches.

In evaluating mangrove-induced wave dissipation at Mai Po Nature Reserve, the study finds limited attenuation attributable to vegetation, with H_S reductions from 1.2–1.7 m offshore to centimeters inland primarily driven by shallow bathymetry and bottom friction. Drag coefficients ($C_{dv} = 2$–4) contribute minor additional dissipation (millimeters to centimeters), though percentage attenuations are locally higher. During Typhoon Hato, forested areas experienced 10–15 cm water level reductions, suggesting geometry-dependent protective benefits. Model validations, with $CC \sim 0.97$ and $RMSD \sim 0.15$ m, confirm accuracy, but emphasize the need for site-specific factors in optimizing nature-based solutions (NbS).

Collectively, these contributions advance the field by bridging scales—from synoptic events to decadal trends—and integrating physical, statistical, and ecological perspectives. The enhanced modeling framework improves hindcast fidelity, while trend and return level analyses quantify evolving risks, informing adaptive strategies amid rising sea levels and intensified storms. The MF-DFA application introduces a novel lens for characterizing wave intermittency, potentially applicable to other ocean basins. Mangrove assessments highlight the contextual efficacy of NbS, advocating for hybrid approaches in coastal defense.

The central scientific novelty of this thesis is the application of multifractal detrended fluctuation analysis (MF-DFA) to significant wave height time series across the entire South China Sea basin. Unlike most prior studies, which typically apply MF-DFA (or related fractal methods) at only a few isolated locations or buoy sites, this work provides a spatially comprehensive characterization of scaling regimes, characteristic time scales, long-range dependencies, and regional differences in multifractality and persistence. This reveals distinct north-south contrasts in wave dynamics—driven by monsoon-typhoon variability in the north versus greater stability in the south—and lays a novel foundation for fractal-based approaches to wave prediction and regime-shift detection in complex marginal seas.

Despite limitations—such as 2D modeling constraints, data sparsity, and simplified vegetation parameters—this thesis lays groundwork for future refinements, including 3D integrations, ensemble projections, multivariate MF-DFA, and advanced NbS modeling. Ultimately, this research contributes to a resilient SCS framework, supporting policy-making for sustainable coastal ecosystems and communities in the face of global change. By elucidating wave dynamics' multifaceted nature, it paves the way for interdisciplinary collaborations to mitigate climate impacts and foster ocean health.

Chapter 9

References

Abdullah, F., S. Husrin, and H. Bachtiar (2019). “Experimental data analysis of wave attenuation in mangroves”. In: *Journal of Physics: Conference Series*. Vol. 1245. 1. IOP Publishing, p. 012095.

Adytia, D. and S. Husrin (2019). “Numerical simulations of nonbreaking solitary wave attenuation by a parameterized mangrove forest model”. In: *International Journal of Engineering & Technology* 8.1.9, pp. 10–16.

Alday, M. and G. Lavidas (2024). “The ECHOWAVE Hindcast: A 30-years high resolution database for wave energy applications in North Atlantic European waters”. In: *Renewable Energy* 236, p. 121391.

Allan, J. C. and P. D. Komar (2006). “Climate controls on US West Coast erosion processes”. In: *Journal of coastal research* 22.3, pp. 511–529.

Anderson, M. E. and J. Smith (2014). “Wave attenuation by flexible, idealized salt marsh vegetation”. In: *Coastal Engineering* 83, pp. 82–92.

Appendini, C. M., A. Torres-Freyermuth, P. Salles, J. López-González, and E. T. Mendoza (2014). “Wave climate and trends for the Gulf of Mexico: A 30-yr wave hindcast”. In: *Journal of Climate* 27.4, pp. 1619–1632.

Ardhuin, F., M. Hamon, F. Collard, B. Chapron, and P. Queffeulou (2008). “Spectral wave evolution and spectral dissipation based on observations: a global validation of new source functions”. In: *Proc. Fourth Chinese–German Joint Symposium on Coastal and Ocean Engineering*.

Ardhuin, F., B. Chapron, and F. Collard (2009). “Observation of swell dissipation across oceans”. In: *Geophysical Research Letters* 36.6.

Ardhuin, F., J. Hanafin, Y. Quilfen, B. Chapron, P. Queffeulou, M. Obrebski, J. Sienkiewicz, and D. Vandemark (2011). “Calibration of the IOWAGA global wave hindcast (1991–2011) using ECMWF and CFSR winds”. In: *Proceedings of the 2011 International Workshop on Wave Hindcasting and Forecasting and 3rd Coastal Hazard Symposium, Kona, HI, USA*. Vol. 30, p. 375.

Ardhuin, F., T. Herbers, and W. O’Reilly (2001). “A hybrid Eulerian–Lagrangian model for spectral wave evolution with application to bottom friction on the continental shelf”. In: *Journal of physical oceanography* 31.6, pp. 1498–1516.

Ardhuin, F., E. Rogers, A. V. Babanin, J.-F. Filipot, R. Magne, A. Roland, A. Van Der Westhuysen, P. Queffeulou, J.-M. Lefevre, L. Aouf, et al. (2010). “Semiempirical dissipation source functions for ocean waves. Part I: Definition, calibration, and validation”. In: *Journal of Physical Oceanography* 40.9, pp. 1917–1941.

Ardhuin, F., A. Roland, F. Dumas, A.-C. Bennis, A. Sentchev, P. Forget, J. Wolf, F. Girard, P. Osuna, and M. Benoit (2012). “Numerical wave modeling in conditions with strong currents: Dissipation, refraction, and relative wind". In: *Journal of Physical Oceanography* 42.12, pp. 2101–2120.

Aydoğan, B. and B. Ayat (2018). "Spatial variability of long-term trends of significant wave heights in the Black Sea". In: *Applied Ocean Research* 79, pp. 20–35.

Bagnasco, T., A. Stocchino, M. I. Vousdoukas, and J. Wang (2025). "A two-way coupled wave–current high resolution hindcast for the South China Sea". In: *Applied Ocean Research* 161, p. 104672.

Baldan, D., E. Coraci, F. Crosato, M. Ferla, A. Bonometto, and S. Morucci (2022). "Importance of non-stationary analysis for assessing extreme sea levels under sea level rise". In: *Natural Hazards and Earth System Sciences* 22.11, pp. 3663–3677.

Battjes, J. A. and J. Janssen (1978). "Energy loss and set-up due to breaking of random waves". In: *Coastal engineering 1978*, pp. 569–587.

Bauer, E. (2001). "Interannual changes of the ocean wave variability in the North Atlantic and in the North Sea". In: *Climate Research* 18.1-2, pp. 63–69.

Bell-James, J., T. Boardman, and R. Foster (2020). "Can't see the (mangrove) forest for the trees: Trends in the legal and policy recognition of mangrove and coastal wetland ecosystem services in Australia". In: *Ecosystem Services* 45, p. 101148.

Belmonte Rivas, M. and A. Stoffelen (2019). "Characterizing ERA-Interim and ERA5 surface wind biases using ASCAT". In: *Ocean Science* 15.3, pp. 831–852.

Benetazzo, A., S. Davison, F. Barbariol, P. Mercogliano, C. Favaretto, and M. Sclavo (2022). *Correction of ERA5 Wind for Regional Climate Projections of Sea Waves, Water, 14, 1590*.

Benoit, M., F. Marcos, and F. Becq (1997). "Development of a third generation shallow-water wave model with unstructured spatial meshing". In: *Coastal Engineering 1996*, pp. 465–478.

Bentamy, A., A. Elyouncha, B. Chapron, F. Desbiolles, et al. (2017). "Homogenization of scatterometer wind retrievals". In: *International Journal of Climatology* 37.2, pp. 870–889.

Bentamy, A. and D. C. Fillon (2012). "Gridded surface wind fields from Metop/ASCAT measurements". In: *International journal of remote sensing* 33.6, pp. 1729–1754.

Bentamy, A., A. Mouche, A. Grouazel, A. Moujane, and A. A. Mohamed (2019). "Using sentinel-1A SAR wind retrievals for enhancing scatterometer and radiometer regional wind analyses". In: *International Journal of Remote Sensing* 40.3, pp. 1120–1147.

Bertin, X., E. Prouteau, and C. Letetrel (2013). "A significant increase in wave height in the North Atlantic Ocean over the 20th century". In: *Global and Planetary Change* 106, pp. 77–83.

Best, Ü. S., M. van der Wegen, J. Dijkstra, J. Reyns, B. C. van Prooijen, and D. Roelvink (2022). "Wave attenuation potential, sediment properties and mangrove growth dynamics data over Guyana's intertidal mudflats: assessing the potential of mangrove restoration works". In: *Earth system science data discussions* 2022, pp. 1–24.

Bidlot, J., S. Abdalla, and P. Janssen (2005). "A revised formulation for ocean wave dissipation in CY25R1". In: *Internal memorandum research department* 60.

Blesić, S., S. Milošević, D. Stratimirović, and M. Ljubisavljević (1999). "Detrended fluctuation analysis of time series of a firing fusimotor neuron". In: *Physica A: Statistical Mechanics and its Applications* 268.3-4, pp. 275–282.

Blumberg, A. F. and G. L. Mellor (1987). "A description of a three-dimensional coastal ocean circulation model". In: *Three-dimensional coastal ocean models* 4, pp. 1–16.

Booij, N., R. C. Ris, and L. H. Holthuijsen (1999). "A third-generation wave model for coastal regions: 1. Model description and validation". In: *Journal of geophysical research: Oceans* 104.C4, pp. 7649–7666.

Boumis, G., H. R. Moftakhari, and H. Moradkhani (2023). "Coevolution of extreme sea levels and sea-level rise under global warming". In: *Earth's Future* 11.7, e2023EF003649.

Bouws, E. and G. Komen (1983). "On the balance between growth and dissipation in an extreme depth-limited wind-sea in the southern North Sea". In: *Journal of physical oceanography* 13.9, pp. 1653–1658.

Braak, C. J. T. (2006). "A Markov Chain Monte Carlo version of the genetic algorithm Differential Evolution: easy Bayesian computing for real parameter spaces". In: *Statistics and Computing* 16, pp. 239–249.

Buldyrev, S., N. Dokholyan, A. Goldberger, S. Havlin, C.-K. Peng, H. Stanley, and G. Viswanathan (1998). "Analysis of DNA sequences using methods of statistical physics". In: *Physica A: Statistical Mechanics and its Applications* 249.1-4, pp. 430–438.

Cabrera, L. and G. Rodríguez (2011). “Detrended fluctuation analysis of significant wave height time series”. In: *WIT Transactions on Ecology and the Environment* 149, pp. 333–341.

Caloiero, T., F. Aristodemo, and D. Algieri Ferraro (2019). “Trend analysis of significant wave height and energy period in southern Italy”. In: *Theoretical and Applied Climatology* 138, pp. 917–930.

Campos, R. M., C. B. Gramcianinov, R. de Camargo, and P. L. da Silva Dias (2022). “Assessment and calibration of ERA5 severe winds in the atlantic ocean using satellite data”. In: *Remote Sensing* 14.19, p. 4918.

Cañellas, B., A. Orfila, F. J. Méndez, M. Menéndez, L. Gómez-Pujol, and J. Tintoré (2024). “Application of a POT model to estimate the extreme significant wave height levels around the Balearic Sea (Western Mediterranean)”. In: *Journal of Coastal Research* 50.sp1, pp. 329–333.

Cardone, V. J., R. E. Jensen, D. T. Resio, V. R. Swail, and A. T. Cox (1996). “Evaluation of contemporary ocean wave models in rare extreme events: The “Halloween Storm” of October 1991 and the “Storm of the Century” of March 1993”. In: *Journal of Atmospheric and Oceanic Technology* 13.1, pp. 198–230.

Carrere, L., F. Lyard, M. Cancet, and A. Guillot (2015). “FES 2014, a new tidal model on the global ocean with enhanced accuracy in shallow seas and in the Arctic region”. In: *EGU general assembly conference abstracts*, p. 5481.

Castelle, B., G. Dodet, G. Masselink, and T. Scott (2018). “Increased winter-mean wave height, variability, and periodicity in the Northeast Atlantic over 1949–2017”. In: *Geophysical Research Letters* 45.8, pp. 3586–3596.

Cavaleri, L. (2009). “Wave modeling—Missing the peaks”. In: *Journal of Physical Oceanography* 39.11, pp. 2757–2778.

Chalikov, D. and M. Y. Belevich (1993). “One-dimensional theory of the wave boundary layer”. In: *Boundary-Layer Meteorology* 63, pp. 65–96.

Chang, Y., Y. Chen, and Y. P. Wang (2020). “Field measurements of tidal flows affected by mangrove seedlings in a restored mangrove swamp, Southern China”. In: *Estuarine, Coastal and Shelf Science* 235, p. 106561.

Change, I. P. O. C. (2007). “Climate change 2007: the physical science basis”. In: *Agenda* 6.07, p. 333.

Chen, C., H. Liu, and R. C. Beardsley (2003). “An unstructured grid, finite-volume, three-dimensional, primitive equations ocean model: application to coastal ocean and estuaries”. In: *Journal of atmospheric and oceanic technology* 20.1, pp. 159–186.

Chen, Y. and O. W. H. Wai (2005). “Wave-current actions on the transport of sediment in Deep Bay, Hong Kong”. In: *31st IAHR Congress 2005: Water Engineering for the Future, Choices and Challenges*. Korea Water Resources Association, pp. 4099–4108.

Chen, Z., B. Dong, Q. Pei, and Z. Zhang (2022). “The impacts of urban vitality and urban density on innovation: Evidence from China’s Greater Bay Area”. In: *Habitat International* 119, p. 102490.

Cheng, L., A. AghaKouchak, E. Gilleland, and R. W. Katz (2014). “Non-stationary extreme value analysis in a changing climate”. In: *Climatic change* 127, pp. 353–369.

Chervenkov, H. and K. Slavov (2017). “Theil-sen estimator for the parameters of the generalized extreme value distributions: Demonstration for meteorological applications”. In: *Comptes rendus de l’Académie bulgare des Sciences* 70.12, pp. 1701–1708.

Coles, S., J. Bawa, L. Trenner, and P. Dorazio (2001). *An introduction to statistical modeling of extreme values*. Vol. 208. Springer.

Collins, C., T. Hesser, P. Rogowski, and S. Merrifield (2021). "Altimeter observations of tropical cyclone-generated sea states: Spatial analysis and operational hindcast evaluation". In: *Journal of Marine Science and Engineering* 9.2, p. 216.

Cooley, D. (2009). "Extreme value analysis and the study of climate change: A commentary on Wigley 1988". In: *Climatic change* 97.1, pp. 77–83.

— (2012). "Return periods and return levels under climate change". In: *Extremes in a changing climate: Detection, analysis and uncertainty*. Springer, pp. 97–114.

Courant, R., K. Friedrichs, and H. Lewy (1928). "Über die partiellen Differenzengleichungen der mathematischen Physik". In: *Mathematische annalen* 100.1, pp. 32–74.

De Dominicis, M., J. Wolf, R. van Hespen, P. Zheng, and Z. Hu (2023). "Mangrove forests can be an effective coastal defence in the Pearl River Delta, China". In: *Communications Earth & Environment* 4.1, p. 13.

De Leo, F., G. Besio, and L. Mentaschi (2021). "Trends and variability of ocean waves under RCP8. 5 emission scenario in the Mediterranean Sea". In: *Ocean Dynamics* 71.1, pp. 97–117.

De Leo, F., A. De Leo, G. Besio, and R. Briganti (2020). "Detection and quantification of trends in time series of significant wave heights: An application in the Mediterranean Sea". In: *Ocean Engineering* 202, p. 107155.

Desbiolles, F., A. Bentamy, B. Blanke, C. Roy, A. M. Mestas-Nuñez, S. A. Grodsky, S. Herbette, G. Cambon, and C. Maes (2017). "Two decades [1992–2012] of surface wind analyses based on satellite scatterometer observations". In: *Journal of Marine Systems* 168, pp. 38–56.

Dietrich, J., M. Zijlema, J. Westerink, L. Holthuijsen, C. Dawson, R. Luettich Jr, R. Jensen, J. Smith, G. Stelling, and G. Stone (2011). "Modeling hurricane waves and storm surge using integrally-coupled, scalable computations". In: *Coastal Engineering* 58.1, pp. 45–65.

Dodet, G., X. Bertin, and R. Taborda (2010). "Wave climate variability in the North-East Atlantic Ocean over the last six decades". In: *Ocean modelling* 31.3-4, pp. 120–131.

Dodet, G., J.-F. Piolle, Y. Quilfen, S. Abdalla, M. Accensi, F. Ardhuin, E. Ash, J.-R. Bidlot, C. Gommenginger, G. Marechal, et al. (2020). "The Sea State CCI dataset v1: towards a sea state climate data record based on satellite observations". In: *Earth System Science Data* 12.3, pp. 1929–1951.

Donelan, M. A., F. W. Dobson, S. D. Smith, and R. J. Anderson (1993). "On the dependence of sea surface roughness on wave development". In: *Journal of physical Oceanography* 23.9, pp. 2143–2149.

Du, W., X. Zhang, H. Shi, G. Li, Z. Zhou, Z. You, and K. Zhang (2024). "Long-term extreme wave characteristics in the water adjacent to china based on era5 reanalysis data". In: *Journal of Ocean University of China* 23.1, pp. 1–10.

Durrant, T., D. Greenslade, M. Hemer, and C. Trenham (2014). *A global wave hindcast focussed on the Central and South Pacific*. Vol. 40. 9. Citeseer.

Eldeberky, Y. (1997). "Nonlinear transformation of wave spectra in the nearshore zone". In: *Oceanographic Literature Review* 4.44, p. 297.

Elshinnawy, A. I., M. Menéndez, and R. Medina (2024). “A parameterization for the correction of ERA5 severe winds for extreme ocean wave modelling”. In: *Ocean Engineering* 312, p. 119048.

Emanuel, K. and R. Rotunno (2011). “Self-stratification of tropical cyclone outflow. Part I: Implications for storm structure”. In: *Journal of the Atmospheric Sciences* 68.10, pp. 2236–2249.

Federico, I., N. Pinardi, G. Coppini, P. Oddo, R. Lecci, and M. Mossa (2017). “Coastal ocean forecasting with an unstructured grid model in the southern Adriatic and northern Ionian seas”. In: *Natural Hazards and Earth System Sciences* 17.1, pp. 45–59.

Fernandes, R. and S. G. Leblanc (2005). “Parametric (modified least squares) and non-parametric (Theil–Sen) linear regressions for predicting biophysical parameters in the presence of measurement errors”. In: *Remote Sensing of Environment* 95.3, pp. 303–316.

Frisch, U. (1985). “On the singularity structure of fully developed turbulence”. In: *Turbulence and predictability in geophysical fluid dynamics and climate dynamics*.

Galiatsatou, P., C. Makris, Y. Krestenitis, and P. Prinos (2021). “Nonstationary extreme value analysis of nearshore sea-state parameters under the effects of climate change: Application to the Greek coastal zone and port structures”. In: *Journal of Marine Science and Engineering* 9.8, p. 817.

Galland, J.-C., N. Goutal, and J.-M. Hervouet (1991). “TELEMAC: A new numerical model for solving shallow water equations”. In: *Advances in water resources* 14.3, pp. 138–148.

Gao, J., R. Luettich, and J. Fleming (2013). “Development and initial evaluation of a generalized asymmetric tropical cyclone vortex model in ADCIRC”. In: *Proceedings of the ADCIRC Users Group Meeting, Vicksburg, MS, USA*. Vol. 16.

Gao, J. (2018). “On the surface wind stress for storm surge modeling”. PhD thesis. The University of North Carolina at Chapel Hill.

Garzon, J. L., M. Maza, C. Ferreira, J. Lara, and I. Losada (2019). “Wave attenuation by Spartina saltmarshes in the Chesapeake Bay under storm surge conditions”. In: *Journal of Geophysical Research: Oceans* 124.7, pp. 5220–5243.

Gaylord, B., M. W. Denny, and M. Koehl (2008). “Flow forces on seaweeds: field evidence for roles of wave impingement and organism inertia”. In: *The Biological Bulletin* 215.3, pp. 295–308.

Gilleland, E. and R. W. Katz (2011). “New software to analyze how extremes change over time”. In: *Eos, Transactions American Geophysical Union* 92.2, pp. 13–14.

Glenny, R. W., H. T. Robertson, S. Yamashiro, and J. B. Bassingthwaighte (1991). “Applications of fractal analysis to physiology”. In: *Journal of Applied Physiology* 70.6, pp. 2351–2367.

Grossmann-Matheson, G., I. R. Young, A. Meucci, and J.-H. Alves (2024). “Global changes in extreme tropical cyclone wave heights under projected future climate conditions”. In: *Scientific Reports* 14.1, p. 31797.

Group, T. W. (1988). “The WAM model—A third generation ocean wave prediction model”. In: *Journal of physical oceanography* 18.12, pp. 1775–1810.

Hanna, S. R. and D. W. Heinold (1985). *Development and application of a simple method for evaluating air quality models*. 4409. American Petroleum Institute.

Hashim, A. M. and S. M. P. Catherine (2013). “A laboratory study on wave reduction by mangrove forests”. In: *APCBEE procedia* 5, pp. 27–32.

Hasselmann, K. (1974). “On the spectral dissipation of ocean waves due to white capping”. In: *Boundary-Layer Meteorology* 6, pp. 107–127.

Hasselmann, K., T. P. Barnett, E. Bouws, H. Carlson, D. E. Cartwright, K. Enke, J. Ewing, A. Gienapp, D. Hasselmann, P. Kruseman, et al. (1973). “Measurements of wind-wave growth and swell decay during the Joint North Sea Wave Project (JONSWAP).” In: *Ergaenzungsheft zur Deutschen Hydrographischen Zeitschrift, Reihe A*.

Hasselmann, S. (1985). “Computations and parametrizations of the nonlinear energy transfer in a gravity wave spectrum. Part I: a new method for efficient computations of the exact nonlinear transfer integral”. In: *Journal of physical oceanography*, pp. 1369–1377.

He, C., Z.-Y. Yin, A. Stocchino, O. W. H. Wai, and S. Li (2022). “The coastal macro-vortices dynamics in Hong Kong waters and its impact on water quality”. In: *Ocean Modelling* 175, p. 102034.

He, J., P. Chan, Q. Li, L. Li, L. Zhang, and H. Yang (2022). “Observations of wind and turbulence structures of Super Typhoons Hato and Mangkhut over land from a 356 m high meteorological tower”. In: *Atmospheric Research* 265, p. 105910.

He, J., Y. He, Q. Li, P. Chan, L. Zhang, H. Yang, and L. Li (2020). “Observational study of wind characteristics, wind speed and turbulence profiles during Super Typhoon Mangkhut”. In: *Journal of Wind Engineering and Industrial Aerodynamics* 206, p. 104362.

He, Y., J. He, W. Chen, P. Chan, J. Fu, and Q. Li (2020). “Insights from Super Typhoon Mangkhut (1822) for wind engineering practices”. In: *Journal of Wind Engineering and Industrial Aerodynamics* 203, p. 104238.

Hemer, M. A., J. Katzfey, and C. E. Trenham (2013). “Global dynamical projections of surface ocean wave climate for a future high greenhouse gas emission scenario”. In: *Ocean Modelling* 70, pp. 221–245.

Hersbach, H., B. Bell, P. Berrisford, G. Biavati, A. Horányi, J. M. Sabater, J. Nicolas, C. Peubey, R. Radu, I. Rozum, et al. (2023). “ERA5 hourly data on single levels from 1940 to present.,(2023)”. In: *Copernicus Climate Change Service (C3S) Climate Data Store (CDS)< date-in-citation content-type=” access-date” iso-8601-date*, pp. 10–26.

Hodges, K., A. Cobb, and P. L. Vidale (2017). “How well are tropical cyclones represented in reanalysis datasets?” In: *Journal of Climate* 30.14, pp. 5243–5264.

Holland, G. (2008). “A revised hurricane pressure–wind model”. In: *Monthly Weather Review* 136.9, pp. 3432–3445.

Holland, G. J. (1980). “An analytic model of the wind and pressure profiles in hurricanes”. In.

Hu, K., P. C. Ivanov, Z. Chen, P. Carpena, and H. E. Stanley (2001). “Effect of trends on detrended fluctuation analysis”. In: *Physical Review E* 64.1, p. 011114.

Hu, Z., T. Suzuki, T. Zitman, W. Uittewaal, and M. Stive (2014). “Laboratory study on wave dissipation by vegetation in combined current–wave flow”. In: *Coastal Engineering* 88, pp. 131–142.

Huang, W., Y. J. Zhang, Z. Wang, F. Ye, S. Moghimi, E. Myers, and H. Yu (2022). “Tidal simulation revisited”. In: *Ocean Dynamics* 72.3, pp. 187–205.

Iimura, K. and N. Tanaka (2012). “Numerical simulation estimating effects of tree density distribution in coastal forest on tsunami mitigation”. In: *Ocean Engineering* 54, pp. 223–232.

Janssen, P., J.-R. Bidlot, S. Abdalla, and H. Hersbach (2005). *Progress in ocean wave forecasting at ECMWF*. ECMWF Reading, UK.

Jiang, B., G. Wu, J. Ding, C. Ma, Y. Fang, and X. Wang (2019). “Assessment of the wave energy resource in the South China Sea”. In: *Proceedings of the Institution of Civil Engineers-Maritime Engineering*. Vol. 172. 1. Thomas Telford Ltd, pp. 23–33.

Kamil, E. A., H. Takaijudin, and A. M. Hashim (2021). “Mangroves as coastal bio-shield: a review of mangroves performance in wave attenuation”. In: *Civil Engineering Journal* 7.11, pp. 1964–1981.

Kantelhardt, J. W., E. Koscielny-Bunde, H. H. Rego, S. Havlin, and A. Bunde (2001). “Detecting long-range correlations with detrended fluctuation analysis”. In: *Physica A: Statistical Mechanics and its Applications* 295.3-4, pp. 441–454.

Kantelhardt, J. W., S. A. Zschiegner, E. Koscielny-Bunde, S. Havlin, A. Bunde, and H. E. Stanley (2002). “Multifractal detrended fluctuation analysis of nonstationary time series”. In: *Physica A: Statistical Mechanics and its Applications* 316.1-4, pp. 87–114.

Katz, R. W. (2010). “Statistics of extremes in climate change”. In: *Climatic change* 100.1, pp. 71–76.

Katz, R. W., M. B. Parlange, and P. Naveau (2002). “Statistics of extremes in hydrology”. In: *Advances in water resources* 25.8-12, pp. 1287–1304.

Keller, J. B. (1958). "Surface waves on water of non-uniform depth". In: *Journal of Fluid Mechanics* 4.6, pp. 607–614.

Kendall, M. G. (1948). "Rank correlation methods." In.

Khan, M. A. (1999). "NATURE RESERVE, HONG KONG". In: *The Mangrove Ecosystem of Deep Bay and the Mai Po Marshes, Hong Kong: Proceedings of the International Workshop on the Mangrove Ecosystem of Deep Bay and the Mai Po Marshes, Hong Kong, 3-20 September 1993*. Kent State University Press, p. 83.

Knapp, K. R., M. C. Kruk, D. H. Levinson, H. J. Diamond, and C. J. Neumann (2010). "The international best track archive for climate stewardship (IBTrACS) unifying tropical cyclone data". In: *Bulletin of the American Meteorological Society* 91.3, pp. 363–376.

Komen, G., S. Hasselmann, and K. Hasselmann (1984). "On the existence of a fully developed wind-sea spectrum". In: *Journal of physical oceanography* 14, pp. 1271–1285.

Kong, W., C. Lam, D. Lau, C. Chow, S. Chong, P. Chan, and N. Leung (2024). "Model Validation and Applications of Wave and Current Forecasts from the Hong Kong Observatory's Operational Marine Forecasting System". In: *Ocean Modelling*, p. 102393.

Koscielny-Bunde, E., A. Bunde, S. Havlin, H. E. Roman, Y. Goldreich, and H.-J. Schellnhuber (1998). "Indication of a universal persistence law governing atmospheric variability". In: *Physical Review Letters* 81.3, p. 729.

Kristiyanto, A., H. Armono, et al. (2013). "KEMAMPUAN HUTAN MANGROVE RUMPUN RHIZHOPHORA SP DAN AVICENNIA SP DALAM MEREDAM GELOMBANG LAUT". In: *Jurnal Pendidikan Fisika Indonesia* 9.2.

Kumar, N., G. Voulgaris, J. C. Warner, and M. Olabarrieta (2012). “Implementation of the vortex force formalism in the coupled ocean-atmosphere-wave-sediment transport (COAWST) modeling system for inner shelf and surf zone applications”. In: *Ocean Modelling* 47, pp. 65–95.

Laface, V., G. Malara, A. Romolo, and F. Arena (2016). “Peak over threshold vis-à-vis equivalent triangular storm: Return value sensitivity to storm threshold”. In: *Coastal Engineering* 116, pp. 220–235.

Lee, W. K., S. H. Tay, S. K. Ooi, and D. A. Friess (2021). “Potential short wave attenuation function of disturbed mangroves”. In: *Estuarine, Coastal and Shelf Science* 248, p. 106747.

Li, A., S. Guan, D. Mo, Y. Hou, X. Hong, and Z. Liu (2020). “Modeling wave effects on storm surge from different typhoon intensities and sizes in the South China Sea”. In: *Estuarine, Coastal and Shelf Science* 235, p. 106551.

Li, Q., F. K. K. Wong, and T. Fung (2019). “Classification of mangrove species using combined WordView-3 and LiDAR data in Mai Po nature reserve, Hong Kong”. In: *Remote Sensing* 11.18, p. 2114.

— (2021). “Mapping multi-layered mangroves from multispectral, hyperspectral, and LiDAR data”. In: *Remote Sensing of Environment* 258, p. 112403.

Liang, B., X. Liu, H. Li, Y. Wu, and D. Lee (2016). “Wave climate hindcasts for the Bohai sea, Yellow sea, and East China sea”. In: *Journal of Coastal Research* 32.1, pp. 172–180.

Liang, B., Z. Shao, H. Li, M. Shao, and D. Lee (2019). “An automated threshold selection method based on the characteristic of extrapolated significant wave heights”. In: *Coastal Engineering* 144, pp. 22–32.

Liu, G., B. Chen, L. Wang, S. Zhang, K. Zhang, and X. Lei (2019). "Wave height statistical characteristic analysis". In: *Journal of oceanology and limnology* 37.2, pp. 448–460.

Liu, H., F. Yang, and H. Wang (2023a). "Research on Multifractal Scale Characteristics of Significant Wave Height Time Series". In: *International Conference on Asian and Pacific Coasts*. Springer, pp. 35–48.

— (2023b). "Research on threshold selection method in wave extreme value analysis". In: *Water* 15.20, p. 3648.

Lodise, J., S. Merrifield, C. Collins, J. Behrens, and E. Terrill (2024). "Performance of ERA5 wind speed and significant wave height within Extratropical cyclones using collocated satellite radar altimeter measurements". In: *Coastal Engineering Journal* 66.1, pp. 89–114.

López Avila, P. (2020). "Análisis multifractal del oleaje usando la metodología de Análisis Multifractal sin Tendencia (MF-DFA)". In.

Luettich, R. A., J. J. Westerink, N. W. Scheffner, et al. (1992). "ADCIRC: an advanced three-dimensional circulation model for shelves, coasts, and estuaries. Report 1, Theory and methodology of ADCIRC-2DD1 and ADCIRC-3DL". In.

Luo, Y. and L. Zhu (2019). "Investigation of trends in extreme significant wave heights in the South China Sea". In: *Aquatic Ecosystem Health & Management* 22.1, pp. 53–64.

Lynch, D. R., J. T. Ip, C. E. Naimie, and F. E. Werner (1996). "Comprehensive coastal circulation model with application to the Gulf of Maine". In: *Continental Shelf Research* 16.7, pp. 875–906.

Ma, M., W. Huang, S. Jung, C. Oslon, K. Yin, and S. Xu (2024). "Evaluating vegetation effects on wave attenuation and dune erosion during hurricane". In: *Journal of Marine Science and Engineering* 12.8, p. 1326.

Mann, H. B. (1945). "Nonparametric tests against trend". In: *Econometrica: Journal of the econometric society*, pp. 245–259.

Martucci, G., S. Carniel, J. Chiggiato, M. Sclavo, P. Lionello, and M. Galati (2010). "Statistical trend analysis and extreme distribution of significant wave height from 1958 to 1999–an application to the Italian Seas". In: *Ocean Science* 6.2, pp. 525–538.

Mclvor, A., I. Moller, T. Spencer, and M. Spalding (2012). "Reduction of wind and swel l waves by mangroves, Natural Coastal Protection Series: Report 1". In: *Cambridge Coastal Research Unit Working Paper* 40.

Mendez, F. J. and I. J. Losada (2004). "An empirical model to estimate the propagation of random breaking and nonbreaking waves over vegetation fields". In: *Coastal Engineering* 51.2, pp. 103–118.

Menéndez, M. and P. L. Woodworth (2010). "Changes in extreme high water levels based on a quasi-global tide-gauge data set". In: *Journal of Geophysical Research: Oceans* 115.C10.

Mentaschi, L., G. Besio, F. Cassola, and A. Mazzino (2013a). "Problems in RMSE-based wave model validations". In: *Ocean Modelling* 72, pp. 53–58.

Mentaschi, L., G. Besio, F. Cassola, and A. Mazzino (2013b). "Developing and validating a forecast/hindcast system for the Mediterranean Sea". In: *Journal of Coastal Research* 65, pp. 1551–1556.

— (2015). "Performance evaluation of Wavewatch III in the Mediterranean Sea". In: *Ocean Modelling* 90, pp. 82–94.

Mentaschi, L., M. Vousdoukas, E. Voukouvalas, L. Sartini, L. Feyen, G. Besio, and L. Alfieri (2016). "The transformed-stationary approach: a generic and simplified methodology for non-stationary extreme value analysis". In: *Hydrology and Earth System Sciences* 20.9, pp. 3527–3547.

Mentaschi, L., M. I. Vousdoukas, G. García-Sánchez, T. Fernández-Montblanc, A. Roland, E. Voukouvalas, I. Federico, A. Abdolali, Y. J. Zhang, and L. Feyen (2023). "A global unstructured, coupled, high-resolution hindcast of waves and storm surge". In: *Frontiers in Marine Science* 10, p. 1233679.

Miles, J. W. (1957). "On the generation of surface waves by shear flows". In: *Journal of Fluid Mechanics* 3.2, pp. 185–204.

Milly, P. C., J. Betancourt, M. Falkenmark, R. M. Hirsch, Z. W. Kundzewicz, D. P. Lettenmaier, and R. J. Stouffer (2008). "Stationarity is dead: Whither water management?" In: *Science* 319.5863, pp. 573–574.

Mirzaei, A., F. Tangang, L. Juneng, M. A. Mustapha, M. L. Husain, and M. F. Akhir (2013). "Wave climate simulation for southern region of the South China Sea". In: *Ocean Dynamics* 63, pp. 961–977.

Morim, J., M. Hemer, X. L. Wang, N. Cartwright, C. Trenham, A. Semedo, I. Young, L. Bricheno, P. Camus, M. Casas-Prat, et al. (2019). "Robustness and uncertainties in global multivariate wind-wave climate projections". In: *Nature Climate Change* 9.9, pp. 711–718.

Murphy, A. H. (1988). "Skill scores based on the mean square error and their relationships to the correlation coefficient". In: *Monthly weather review* 116.12, pp. 2417–2424.

Nehru, P. and P. Balasubramanian (2018). "Mangrove species diversity and composition in the successional habitats of Nicobar Islands, India: A post-tsunami and subsidence scenario”. In: *Forest Ecology and Management* 427, pp. 70–77.

Nepf, H. M. and E. Vivoni (2000). “Flow structure in depth-limited, vegetated flow”. In: *Journal of Geophysical Research: Oceans* 105.C12, pp. 28547–28557.

Nguyen, H. M., S. Ouillon, and V. D. Vu (2022). “Sea level variation and trend analysis by comparing Mann–Kendall test and innovative trend analysis in front of the Red River Delta, Vietnam (1961–2020)”. In: *Water* 14.11, p. 1709.

Owen, R. B. and R. Lee (2004). “Human impacts on organic matter sedimentation in a proximal shelf setting, Hong Kong”. In: *Continental shelf research* 24.4-5, pp. 583–602.

Ozger, M. (2011). “Scaling characteristics of ocean wave height time series”. In: *Physica A: Statistical Mechanics and its Applications* 390.6, pp. 981–989.

Pasha, G. A. and N. Tanaka (2016). “Energy loss and drag in a steady flow through emergent vegetation”. In: *Proceedings of 12th ICHE Conference*, pp. 1–6.

— (2017). “Undular hydraulic jump formation and energy loss in a flow through emergent vegetation of varying thickness and density”. In: *Ocean Engineering* 141, pp. 308–325.

Peng, C.-K., S. V. Buldyrev, S. Havlin, M. Simons, H. E. Stanley, and A. L. Goldberger (1994). “Mosaic organization of DNA nucleotides”. In: *Physical review e* 49.2, p. 1685.

Peng, F., X. Deng, and Y. Shen (2024). “Wave contributions to sea levels along the coast of northern South China Sea over 2002–2022”. In: *Advances in Space Research* 73.9, pp. 4584–4596.

Perez, J., M. Menendez, and I. J. Losada (2017). "GOW2: A global wave hindcast for coastal applications". In: *Coastal Engineering* 124, pp. 1–11.

Pham, D. T., A. D. Switzer, G. Huerta, A. J. Meltzner, H. M. Nguyen, and E. M. Hill (2019). "Spatiotemporal variations of extreme sea levels around the South China Sea: assessing the influence of tropical cyclones, monsoons and major climate modes". In: *Natural Hazards* 98, pp. 969–1001.

Phan, K., M. Stive, M. Zijlema, H. Truong, and S. Aarninkhof (2019). "The effects of wave non-linearity on wave attenuation by vegetation". In: *Coastal Engineering* 147, pp. 63–74.

Phillips, O. (1985). "Spectral and statistical properties of the equilibrium range in wind-generated gravity waves". In: *Journal of Fluid Mechanics* 156, pp. 505–531.

Pickands III, J. (1975). "Statistical inference using extreme order statistics". In: *the Annals of Statistics*, pp. 119–131.

Pilar, P., C. G. Soares, and J. Carretero (2008). "44-year wave hindcast for the North East Atlantic European coast". In: *Coastal Engineering* 55.11, pp. 861–871.

Piollé, J.-F., G. Dodet, and Y. Quilfen (2020). "ESA Sea State Climate Change Initiative(Sea_State_cci): Global remote sensing merged multi-mission monthly gridded significant wave height, L4 product, version 1.1., Centre for Environmental Data Analysis". In: *Centre for Environmental Data Analysis*.

Pomaro, A., L. Cavaleri, and P. Lionello (2017). "Climatology and trends of the Adriatic Sea wind waves: analysis of a 37-year long instrumental data set". In: *International Journal of Climatology* 37.12, pp. 4237–4250.

Pond, S. and G. L. Pickard (1983). *Introductory dynamical oceanography*. Gulf Professional Publishing.

Punchihewa, N. and S. Krishnarajah (2019). "Factors influencing the distribution of Mysids (Crustacea: Mysida) in the Negombo lagoon, Sri Lanka". In: *Ceylon Journal of Science* 48.4.

Qian, C., H. Jiang, X. Wang, and G. Chen (2020). "Climatology of wind-seas and swells in the China seas from wave hindcast". In: *Journal of Ocean University of China* 19, pp. 90–100.

Radfar, S., P. Galiatsatou, and T. Wahl (2023). "Application of nonstationary extreme value analysis in the coastal environment–A systematic literature review". In: *Weather and Climate Extremes* 41, p. 100575.

Rasmeemasmuang, T. and J. Sasaki (2015). "Wave reduction in mangrove forests: General information and case study in Thailand". In: *Handbook of Coastal Disaster Mitigation for Engineers and Planners*. Elsevier, pp. 511–535.

Renard, B., X. Sun, and M. Lang (2012). "Bayesian methods for non-stationary extreme value analysis". In: *Extremes in a changing climate: Detection, analysis and uncertainty*. Springer, pp. 39–95.

Roland, A. et al. (2008). "Development of WWM II: Spectral wave modelling on unstructured meshes". PhD thesis. Ph. D. thesis, Technische Universität Darmstadt, Institute of Hydraulic and …

Roland, A., A. Cucco, C. Ferrarin, T.-W. Hsu, J.-M. Liau, S.-H. Ou, G. Umgiesser, and U. Zanke (2009). "On the development and verification of a 2-D coupled wave-current model on unstructured meshes". In: *Journal of Marine Systems* 78, S244–S254.

Roland, A., Y. J. Zhang, H. V. Wang, Y. Meng, Y.-C. Teng, V. Maderich, I. Brovchenko, M. Dutour-Sikiric, and U. Zanke (2012). "A fully coupled 3D wave-current interaction model on unstructured grids". In: *Journal of Geophysical Research: Oceans* 117.C11.

Ruggiero, P., P. D. Komar, and J. C. Allan (2010). "Increasing wave heights and extreme value projections: The wave climate of the US Pacific Northwest". In: *Coastal Engineering* 57.5, pp. 539–552.

Salas, J. D. and J. Obeysekera (2014). "Revisiting the concepts of return period and risk for nonstationary hydrologic extreme events". In: *Journal of hydrologic engineering* 19.3, pp. 554–568.

Schenkel, B. A. and R. E. Hart (2012). "An examination of tropical cyclone position, intensity, and intensity life cycle within atmospheric reanalysis datasets". In: *Journal of Climate* 25.10, pp. 3453–3475.

Sen, P. K. (1968). "Estimates of the regression coefficient based on Kendall's tau". In: *Journal of the American statistical association* 63.324, pp. 1379–1389.

Serinaldi, F. (2015). "Dismissing return periods!" In: *Stochastic environmental research and risk assessment* 29.4, pp. 1179–1189.

Shanas, P. and V. Sanil Kumar (2014). "Temporal variations in the wind and wave climate at a location in the eastern Arabian Sea based on ERA-Interim reanalysis data". In: *Natural hazards and earth system sciences* 14.5, pp. 1371–1381.

Shi, J., A. Joly, J. Zheng, J. Zhang, T. Chen, and G. Chen (2017). "Development of a sea-state database in the northwest Pacific Ocean by long-term numerical hindcast modelling". In: *International Conference on Nuclear Engineering*. Vol. 57823. American Society of Mechanical Engineers, V004T14A008.

Shi, J., J. Zheng, C. Zhang, A. Joly, W. Zhang, P. Xu, T. Sui, and T. Chen (2019). "A 39-year high resolution wave hindcast for the Chinese coast: Model validation and wave climate analysis". In: *Ocean Engineering* 183, pp. 224–235.

Sørensen, O. R., H. Kofoed-Hansen, M. Rugbjerg, and L. S. Sørensen (2005). "A third-generation spectral wave model using an unstructured finite volume technique". In: *Coastal Engineering 2004: (In 4 Volumes)*. World Scientific, pp. 894–906.

Soulsby, R. (1997). "Dynamics of marine sands". In.

Stanley, H. E. and R. N. Mantegna (2000). *An introduction to econophysics*. Cambridge University Press, Cambridge.

Stopa, J. E., F. Ardhuin, E. Stutzmann, and T. Lecocq (2019). "Sea state trends and variability: Consistency between models, altimeters, buoys, and seismic data (1979–2016)". In: *Journal of Geophysical Research: Oceans* 124.6, pp. 3923–3940.

Strusińska-Correia, A., S. Husrin, and H. Oumeraci (2013). "Tsunami damping by mangrove forest: a laboratory study using parameterized trees". In: *Natural Hazards and Earth System Sciences* 13.2, pp. 483–503.

Sun, Z., H. Zhang, D. Xu, X. Liu, and J. Ding (2020). "Assessment of wave power in the South China Sea based on 26-year high-resolution hindcast data". In: *Energy* 197, p. 117218.

Talkner, P. and R. O. Weber (2000). "Power spectrum and detrended fluctuation analysis: Application to daily temperatures". In: *Physical Review E* 62.1, p. 150.

Tanino, Y. and H. M. Nepf (2008). "Laboratory investigation of mean drag in a random array of rigid, emergent cylinders". In: *Journal of Hydraulic Engineering* 134.1, pp. 34–41.

Tank, A., F. Zwiers, and X. Zhang (2009). "Guidelines on analysis of extremes in a changing climate in support of informed decisions for adaptation. Climate Data and Monitoring WCDMP-No. 72". In: *World Meteorological Organization, WMO-TD* 1500.

Taylor, K. E. (2001). "Summarizing multiple aspects of model performance in a single diagram". In: *Journal of geophysical research: atmospheres* 106.D7, pp. 7183–7192.

Teh, S. Y., H. L. Koh, P. L.-.-F. Liu, A. I. M. Ismail, and H. L. Lee (2009). "Analytical and numerical simulation of tsunami mitigation by mangroves in Penang, Malaysia". In: *Journal of Asian Earth Sciences* 36.1, pp. 38–46.

Ter Braak, C. J. and J. A. Vrugt (2008). "Differential evolution Markov chain with snooker updater and fewer chains". In: *Statistics and Computing* 18, pp. 435–446.

Theil, H. (1992). "A rank-invariant method of linear and polynomial regression analysis". In: *Henri Theil's contributions to economics and econometrics: Econometric theory and methodology*. Springer, pp. 345–381.

Toimil, A., P. Camus, I. J. Losada, and M. Alvarez-Cuesta (2021). "Visualising the uncertainty cascade in multi-ensemble probabilistic coastal erosion projections". In: *Frontiers in Marine Science* 8, p. 683535.

Tolman, H. L. (1991). "A third-generation model for wind waves on slowly varying, unsteady, and inhomogeneous depths and currents". In: *Journal of Physical Oceanography* 21.6, pp. 782–797.

Tolman, H. L. and D. Chalikov (1996). “Source terms in a third-generation wind wave model”. In: *Journal of Physical Oceanography* 26.11, pp. 2497–2518.

Umgiesser, G., D. M. Canu, A. Cucco, and C. Solidoro (2004). “A finite element model for the Venice Lagoon. Development, set up, calibration and validation”. In: *Journal of Marine Systems* 51.1-4, pp. 123–145.

Van Rooijen, A., J. Van Thiel de Vries, R. McCall, A. Van Dongeren, J. Roelvink, A. Reniers, et al. (2015). “Modeling of wave attenuation by vegetation with XBeach”. In: *E-proceedings of the 36th IAHR World Congress*. Vol. 28. IAHR Netherlands.

Vanem, E. (2015). “Non-stationary extreme value models to account for trends and shifts in the extreme wave climate due to climate change”. In: *Applied Ocean Research* 52, pp. 201–211.

Vanem, E. and S.-E. Walker (2013). “Identifying trends in the ocean wave climate by time series analyses of significant wave heightdata”. In: *Ocean engineering* 61, pp. 148–160.

Vogt, T., S. Treu, M. Mengel, K. Frieler, and C. Otto (2024). “Modeling surge dynamics improves coastal flood estimates in a global set of tropical cyclones”. In: *Communications Earth & Environment* 5.1, p. 529.

Vrugt, J. A., C. J. ter Braak, C. G. Diks, B. A. Robinson, J. M. Hyman, and D. Higdon (2009). “Accelerating Markov chain Monte Carlo simulation by differential evolution with self-adaptive randomized subspace sampling”. In: *International journal of nonlinear sciences and numerical simulation* 10.3, pp. 273–290.

Wang, H., Y. Yang, B. Sun, and Y. Shi (2017). "Improvements to the statistical theoretical model for wave breaking based on the ratio of breaking wave kinetic and potential energy". In: *Science China Earth Sciences* 60, pp. 180–187.

Wang, J., J. Liu, Y. Wang, Z. Liao, and P. Sun (2021). "Spatiotemporal variations and extreme value analysis of significant wave height in the South China Sea based on 71-year long ERA5 wave reanalysis". In: *Applied Ocean Research* 113, p. 102750.

Wang, J. and P. L.-F. Liu (2021). "Numerical study on impacts of a concurrent storm-tide-tsunami event in Macau and Hong Kong". In: *Coastal Engineering* 170, p. 104000.

Wang, N., Y. Hou, S. Li, and R. Li (2019). "Numerical simulation and preliminary analysis of typhoon waves during three typhoons in the Yellow Sea and East China Sea". In: *Journal of Oceanology and Limnology* 37.6, pp. 1805–1816.

Wang, Z., C. Duan, and S. Dong (2018). "Long-term wind and wave energy resource assessment in the South China sea based on 30-year hindcast data". In: *Ocean Engineering* 163, pp. 58–75.

Weatherall, P., K. M. Marks, M. Jakobsson, T. Schmitt, S. Tani, J. E. Arndt, M. Rovere, D. Chayes, V. Ferrini, and R. Wigley (2015). "A new digital bathymetric model of the world's oceans". In: *Earth and space Science* 2.8, pp. 331–345.

Wikramanayake, E., C. Or, F. Costa, X. Wen, F. Cheung, and A. Shapiro (2020). "A climate adaptation strategy for Mai Po Inner Deep Bay Ramsar site: steppingstone to climate proofing the East Asian-Australasian Flyway". In: *Plos one* 15.10, e0239945.

Wu, Z.-y., C.-b. Jiang, B. Deng, J. Chen, Y.-g. Cao, and L.-j. Li (2018). "Evaluation of numerical wave model for typhoon wave simulation in South China Sea". In: *Water Science and Engineering* 11.3, pp. 229–235.

Xie, J., N. Wei, and Q. Gao (2024). "Assessing spatiotemporal population density dynamics from 2000 to 2020 in megacities using urban and rural morphologies". In: *Scientific Reports* 14.1, p. 14166.

Xu, F.-H. and L.-Y. Oey (2015). "Seasonal SSH variability of the northern South China Sea". In: *Journal of Physical Oceanography* 45.6, pp. 1595–1609.

Xu, Y., H. He, J. Song, Y. Hou, and F. Li (2017). "Observations and modeling of typhoon waves in the South China Sea". In: *Journal of Physical Oceanography* 47.6, pp. 1307–1324.

Yang, J., L. Li, K. Zhao, P. Wang, D. Wang, I. M. Sou, Z. Yang, J. Hu, X. Tang, K. M. Mok, et al. (2019). "A comparative study of Typhoon Hato (2017) and Typhoon Mangkhut (2018)—Their impacts on coastal inundation in Macau". In: *Journal of Geophysical Research: Oceans* 124.12, pp. 9590–9619.

Yang, S., L. Fan, S. Duan, C. Zheng, X. Li, H. Li, and J. Xu (2020). "Long-term assessment of wave energy in the China Sea using 30-year hindcast data". In: *Energy Exploration & Exploitation* 38.1, pp. 37–56.

Yang, S., Y. Hou, and Y. Liu (2015). "Observed typhoon wave spectrum in northern South China Sea". In: *Chinese journal of oceanology and limnology* 33.5, pp. 1286–1294.

Yin, K., S. Xu, S. Gong, J. Chen, Y. Wang, and M. Li (2022). "Modeling wave attenuation by submerged flexible vegetation with XBeach phase-averaged model". In: *Ocean Engineering* 257, p. 111646.

Yin, K., S. Xu, W. Huang, S. Liu, and M. Li (2021). “Numerical investigation of wave attenuation by coupled flexible vegetation dynamic model and XBeach wave model”. In: *Ocean Engineering* 235, p. 109357.

Young, I. R. and A. V. Babanin (2006). “Spectral distribution of energy dissipation of wind-generated waves due to dominant wave breaking”. In: *Journal of physical Oceanography* 36.3, pp. 376–394.

Zeng, X., M. Zhao, and R. E. Dickinson (1998). “Intercomparison of bulk aerodynamic algorithms for the computation of sea surface fluxes using TOGA COARE and TAO data”. In: *Journal of Climate* 11.10, pp. 2628–2644.

Zhai, R., C. Huang, W. Yang, L. Tang, and W. Zhang (2023). “Applicability evaluation of ERA5 wind and wave reanalysis data in the South China Sea”. In: *Journal of Oceanology and Limnology* 41.2, pp. 495–517.

Zhang, Y. J., T. Fernandez-Montblanc, W. Pringle, H.-C. Yu, L. Cui, and S. Moghimi (2023). “Global seamless tidal simulation using a 3D unstructured-grid model (SCHISM v5. 10.0)”. In: *Geoscientific Model Development* 16.9, pp. 2565–2581.

Zhang, Y. and A. M. Baptista (2008). “SELFE: A semi-implicit Eulerian–Lagrangian finite-element model for cross-scale ocean circulation”. In: *Ocean modelling* 21.3-4, pp. 71–96.

Zhang, Y. J., F. Ye, E. V. Stanev, and S. Grashorn (2016). “Seamless cross-scale modeling with SCHISM”. In: *Ocean Modelling* 102, pp. 64–81.

Zhou, K., Q.-S. Li, and X. Li (2020). “Dynamic behavior of supertall building with active control system during Super Typhoon Mangkhut”. In: *Journal of Structural Engineering* 146.5, p. 04020077.

Zu, T., J. Gan, and S. Y. Erofeeva (2008). “Numerical study of the tide and tidal dynamics in the South China Sea”. In: *Deep Sea Research Part I: Oceanographic Research Papers* 55.2, pp. 137–154.

Appendices

Appendix 1: Mean annual bias from 1992 to 2020

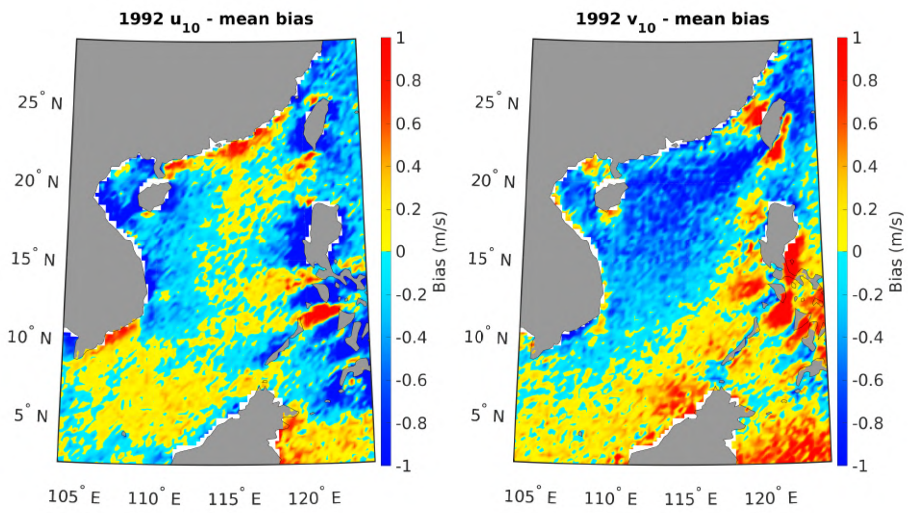

Figure 9.1: Mean annual bias in 1992 for both eastward and northward wind velocity components.

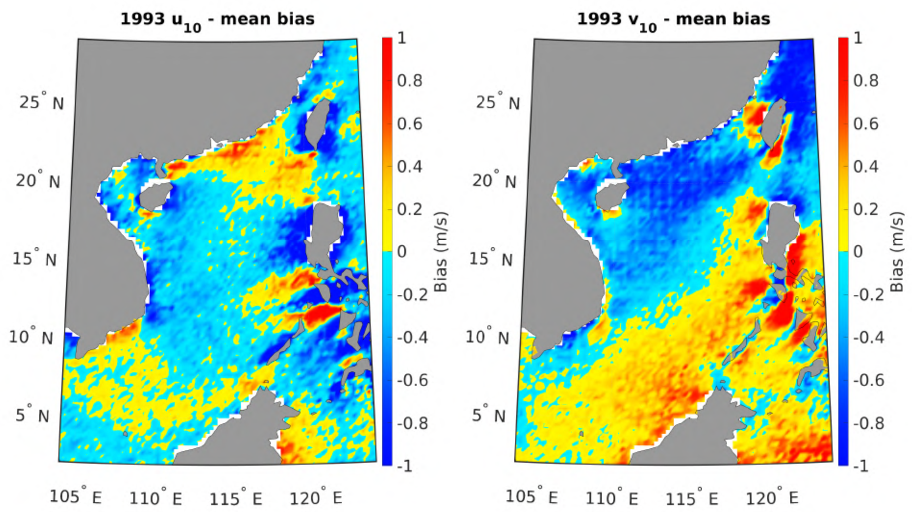

Figure 9.2: Mean annual bias in 1993 for both eastward and northward wind velocity components.

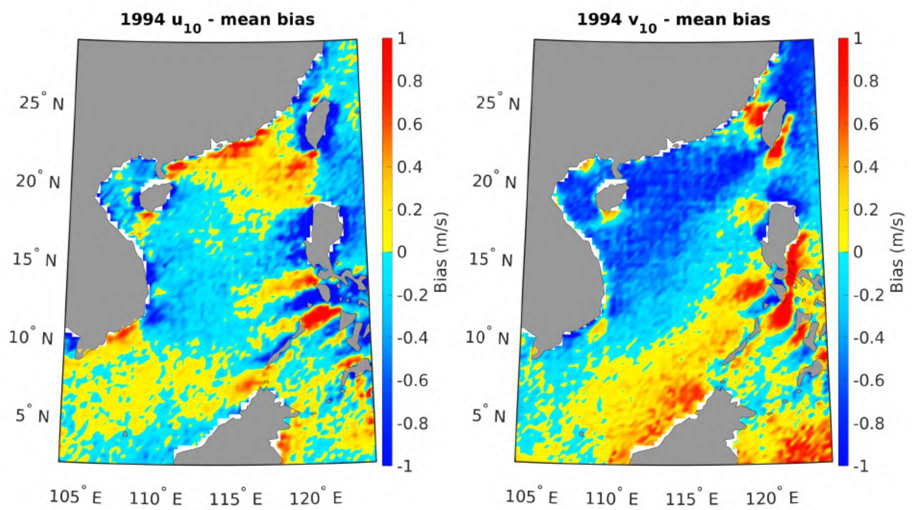

Figure 9.3: Mean annual bias in 1994 for both eastward and northward wind velocity components.

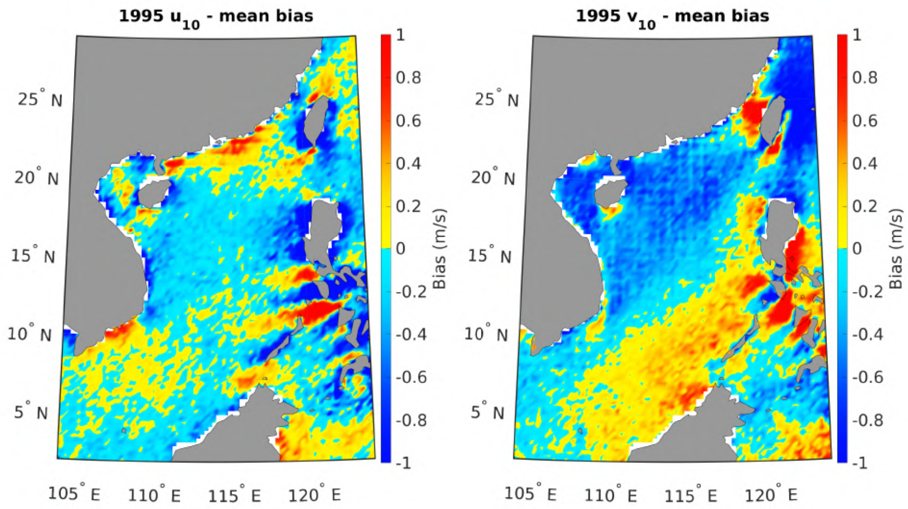

Figure 9.4: Mean annual bias in 1995 for both eastward and northward wind velocity components.

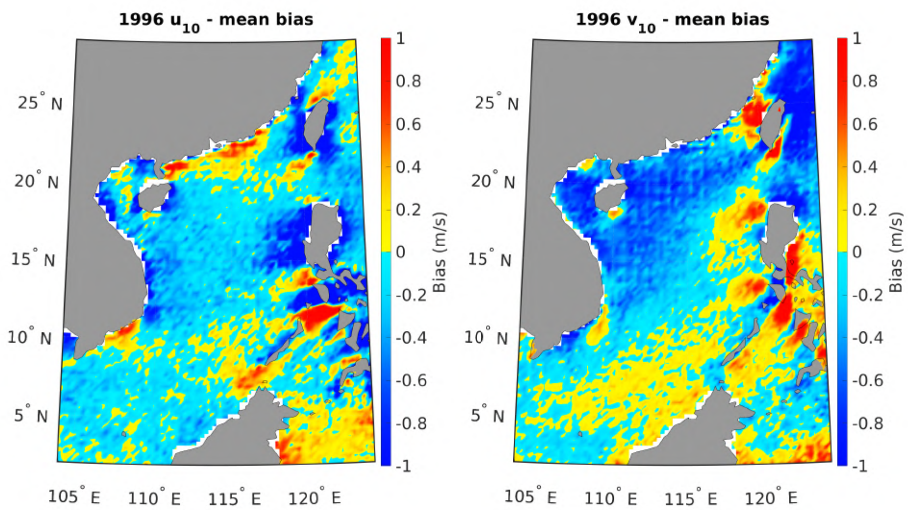

Figure 9.5: Mean annual bias in 1996 for both eastward and northward wind velocity components.

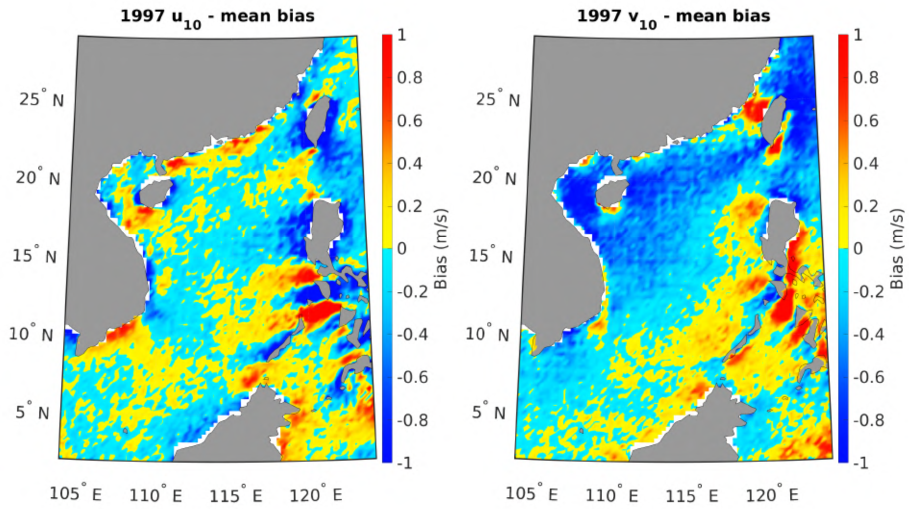

Figure 9.6: Mean annual bias in 1997 for both eastward and northward wind velocity components.

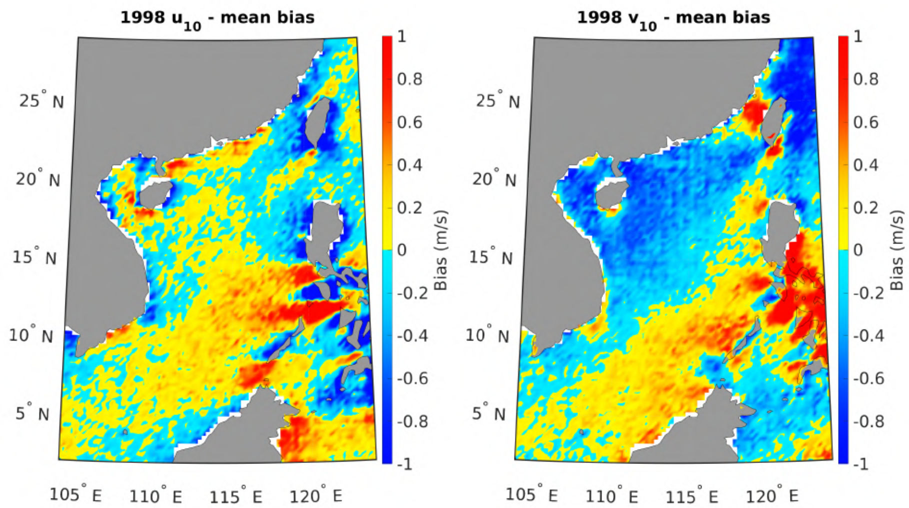

Figure 9.7: Mean annual bias in 1998 for both eastward and northward wind velocity components.

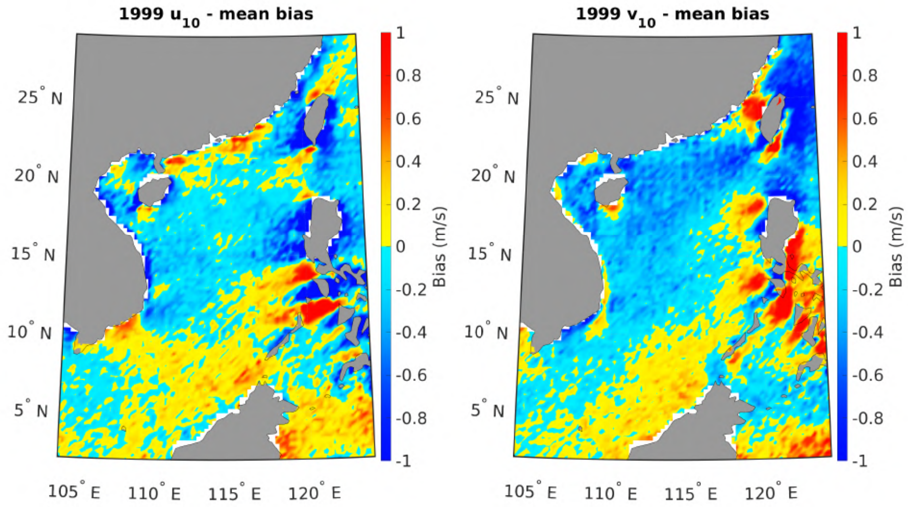

Figure 9.8: Mean annual bias in 1999 for both eastward and northward wind velocity components.

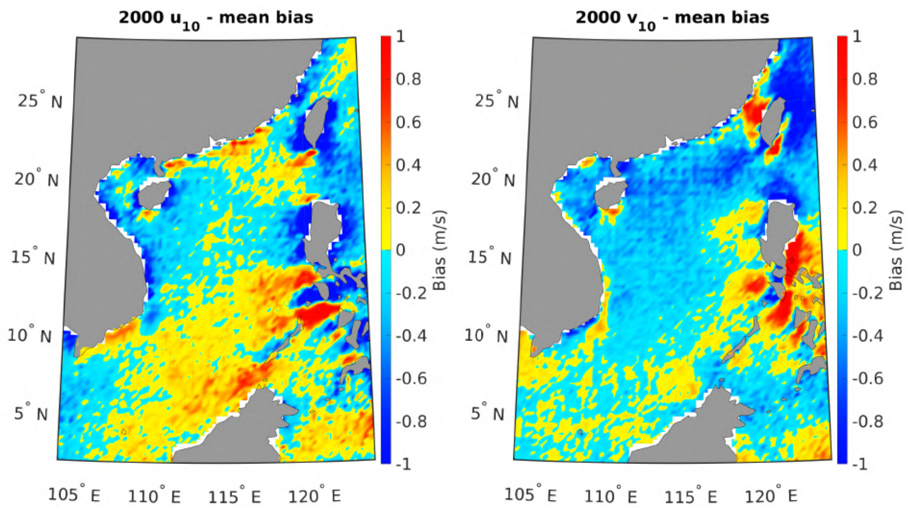

Figure 9.9: Mean annual bias in 2000 for both eastward and northward wind velocity components.

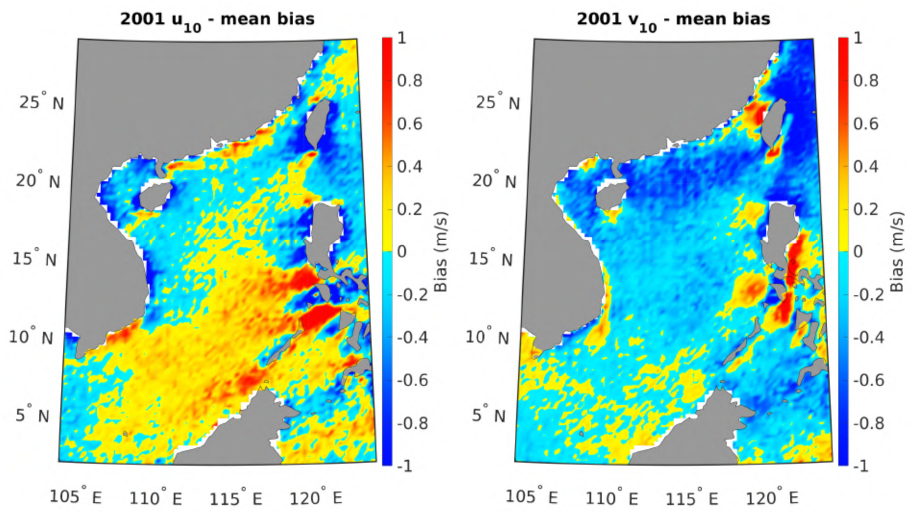

Figure 9.10: Mean annual bias in 2001 for both eastward and northward wind velocity components.

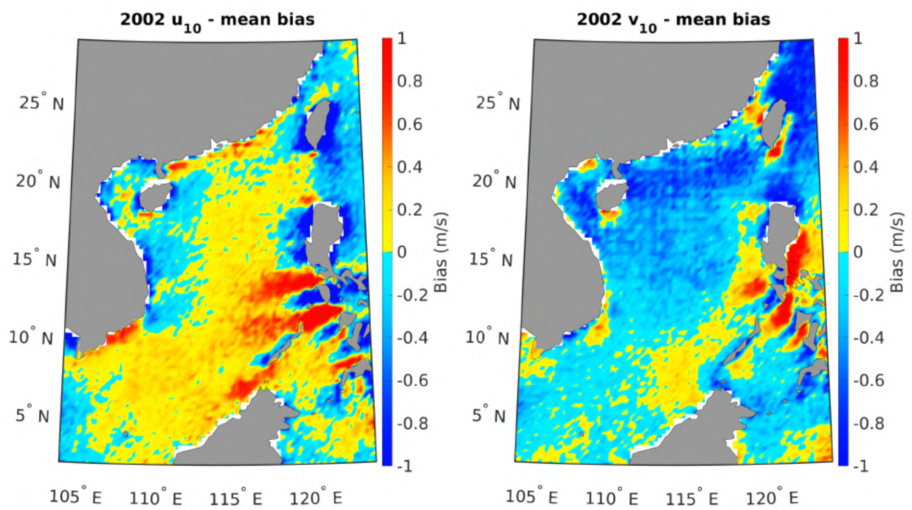

Figure 9.11: Mean annual bias in 2002 for both eastward and northward wind velocity components.

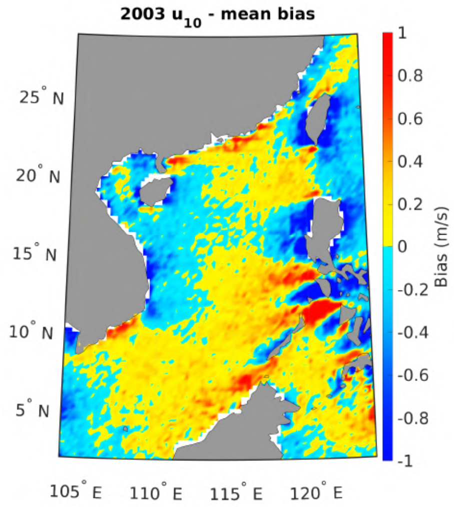

Figure 9.12: Mean annual bias in 2003 for both eastward and northward wind velocity components.

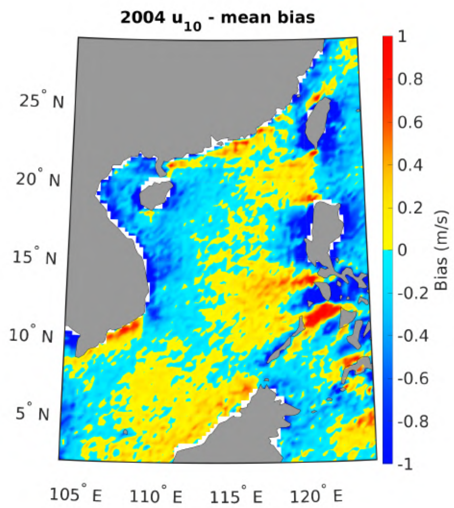

Figure 9.13: Mean annual bias in 2004 for both eastward and northward wind velocity components.

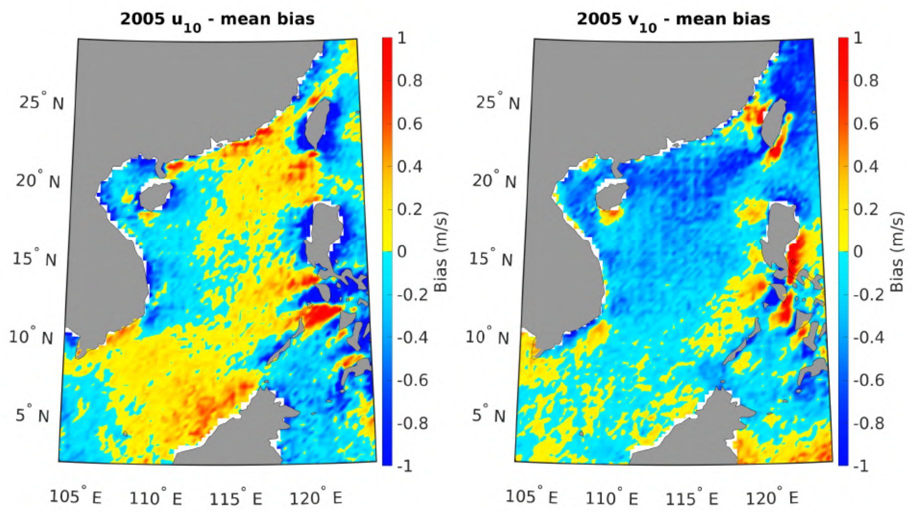

Figure 9.14: Mean annual bias in 2005 for both eastward and northward wind velocity components.

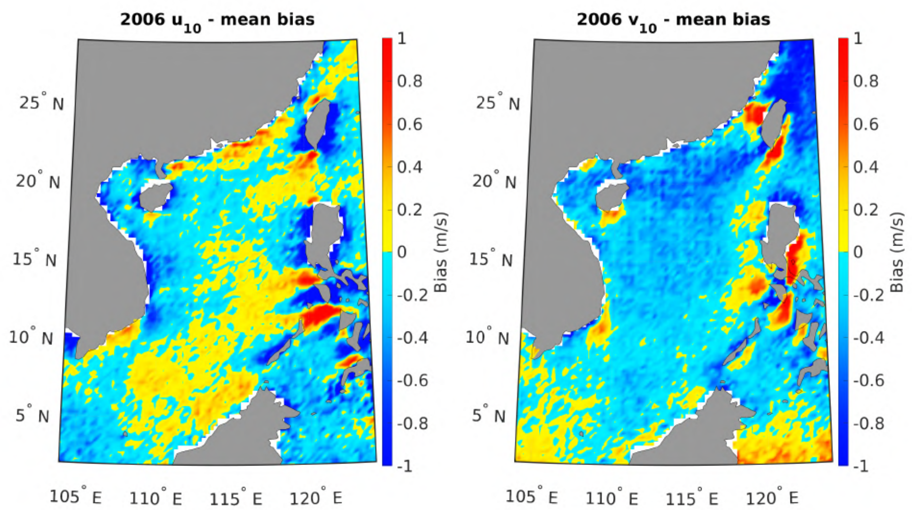

Figure 9.15: Mean annual bias in 2006 for both eastward and northward wind velocity components.

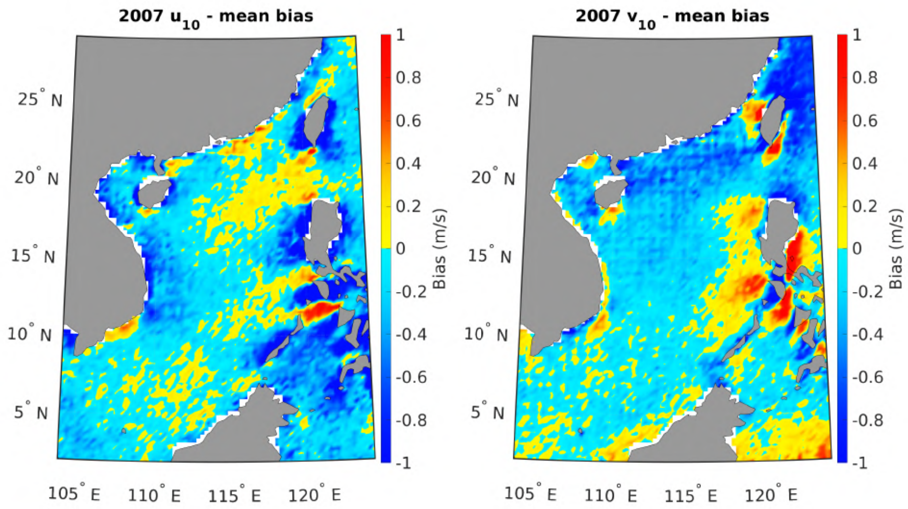

Figure 9.16: Mean annual bias in 2007 for both eastward and northward wind velocity components.

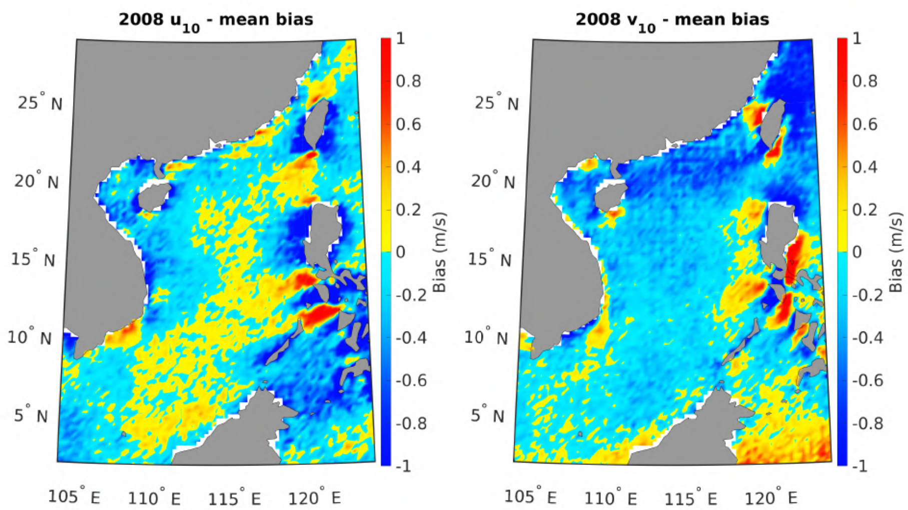

Figure 9.17: Mean annual bias in 2008 for both eastward and northward wind velocity components.

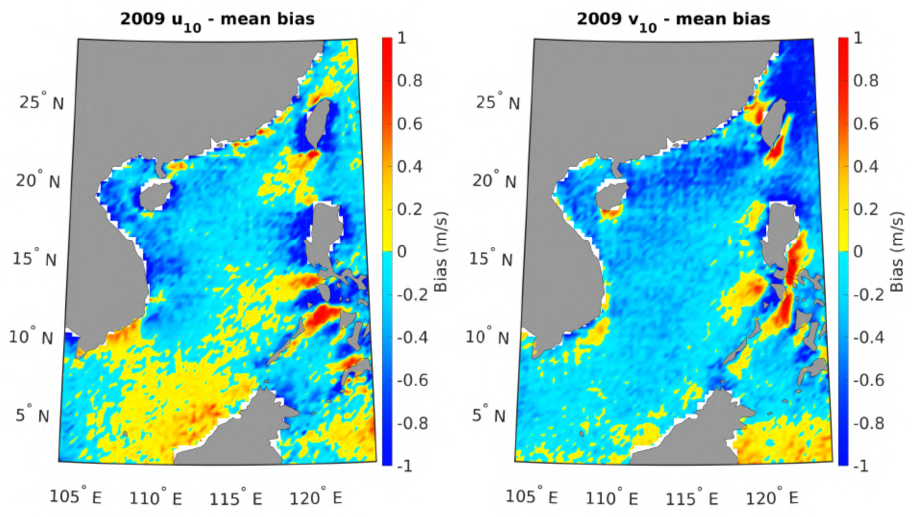

Figure 9.18: Mean annual bias in 2009 for both eastward and northward wind velocity components.

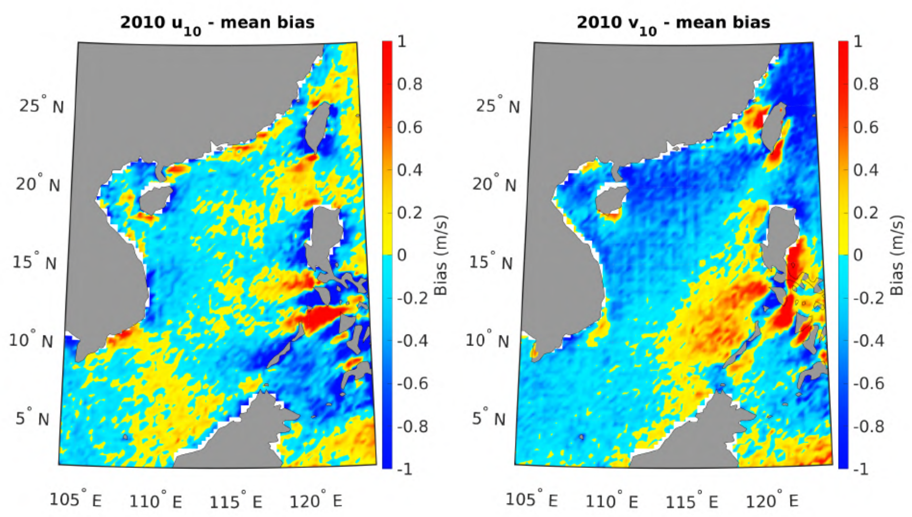

Figure 9.19: Mean annual bias in 2010 for both eastward and northward wind velocity components.

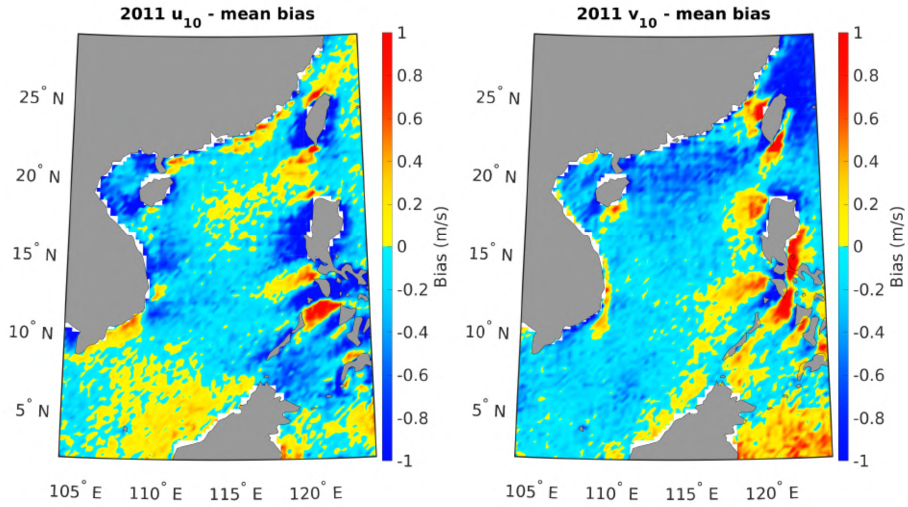

Figure 9.20: Mean annual bias in 2011 for both eastward and northward wind velocity components.

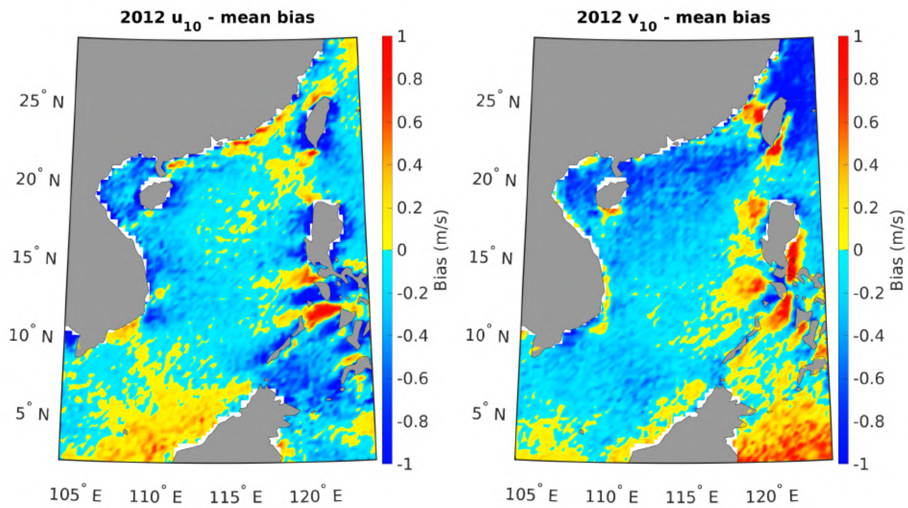

Figure 9.21: Mean annual bias in 2012 for both eastward and northward wind velocity components.

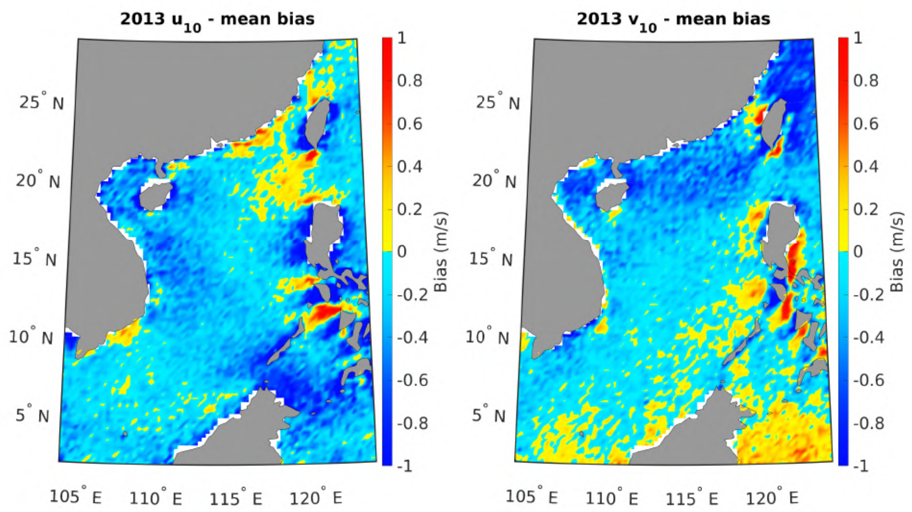

Figure 9.22: Mean annual bias in 2013 for both eastward and northward wind velocity components.

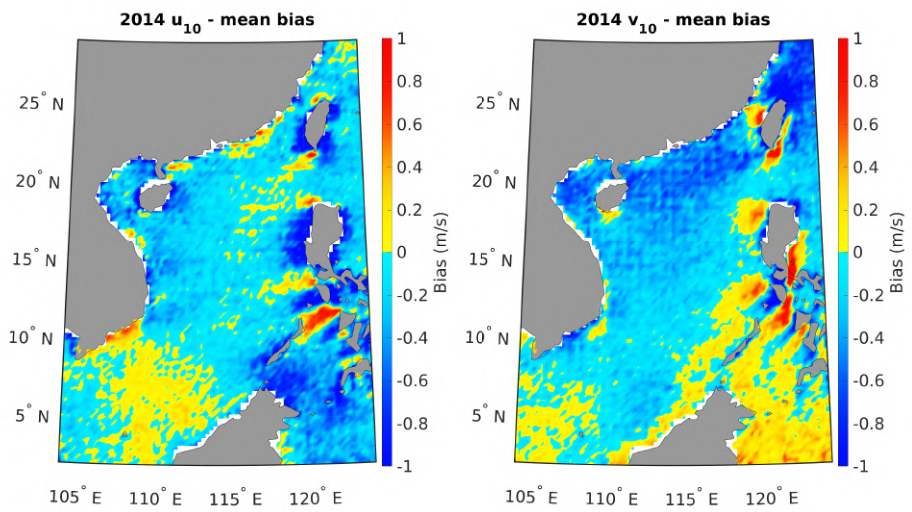

Figure 9.23: Mean annual bias in 2014 for both eastward and northward wind velocity components.

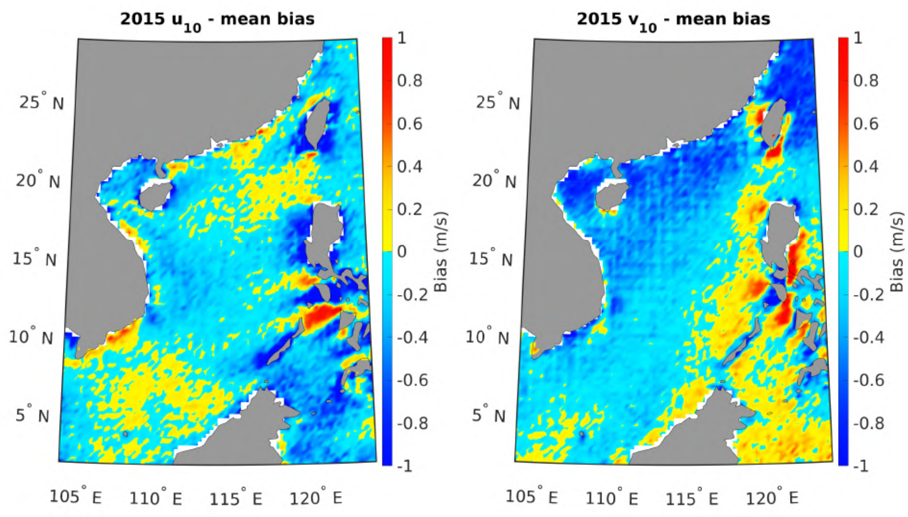

Figure 9.24: Mean annual bias in 2015 for both eastward and northward wind velocity components.

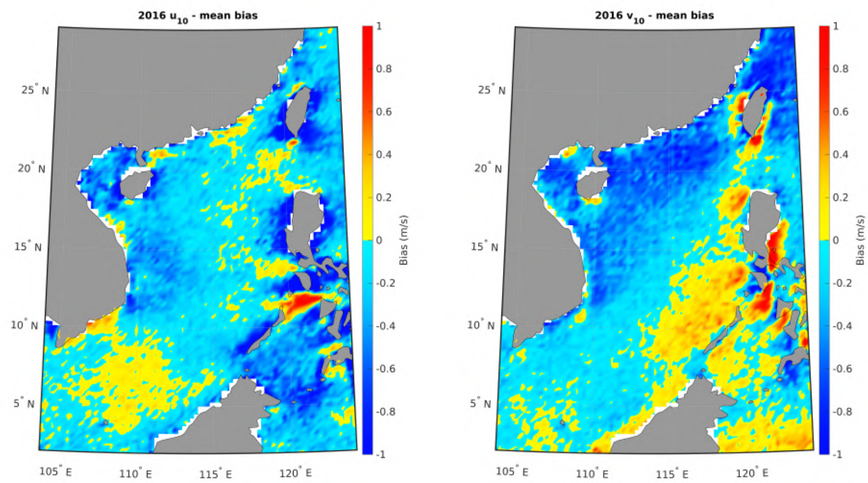

Figure 9.25: Mean annual bias in 2016 for both eastward and northward wind velocity components.

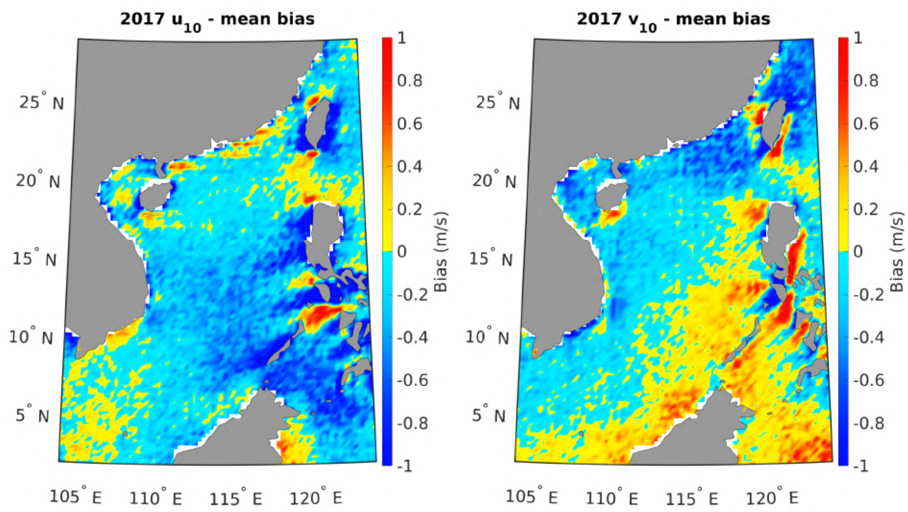

Figure 9.26: Mean annual bias in 2017 for both eastward and northward wind velocity components.

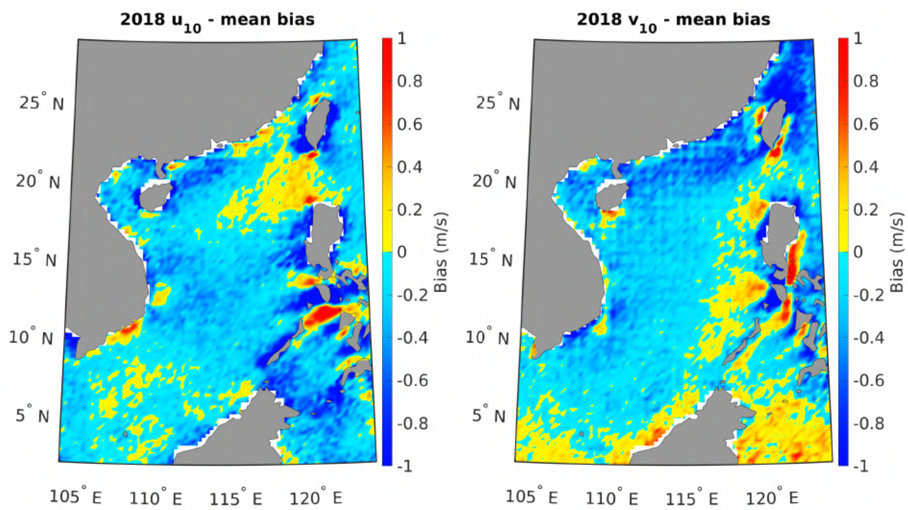

Figure 9.27: Mean annual bias in 2018 for both eastward and northward wind velocity components.

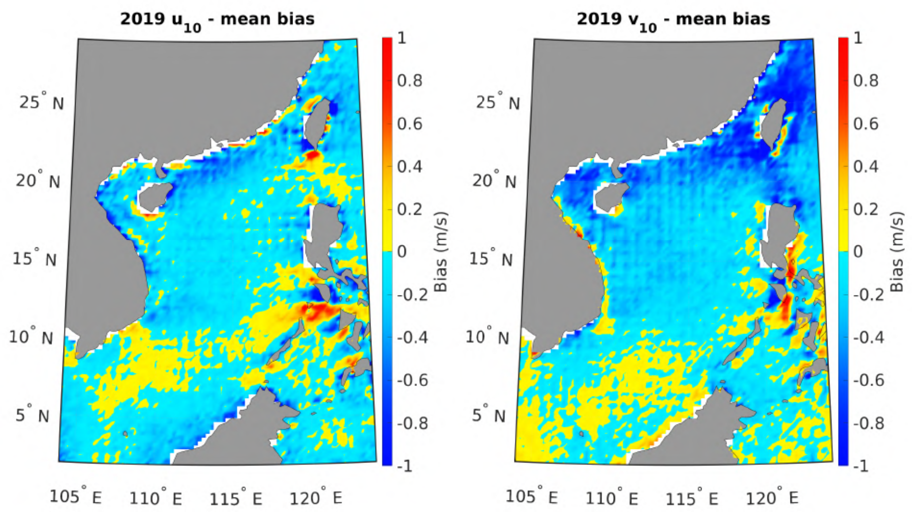

Figure 9.28: Mean annual bias in 2019 for both eastward and northward wind velocity components.

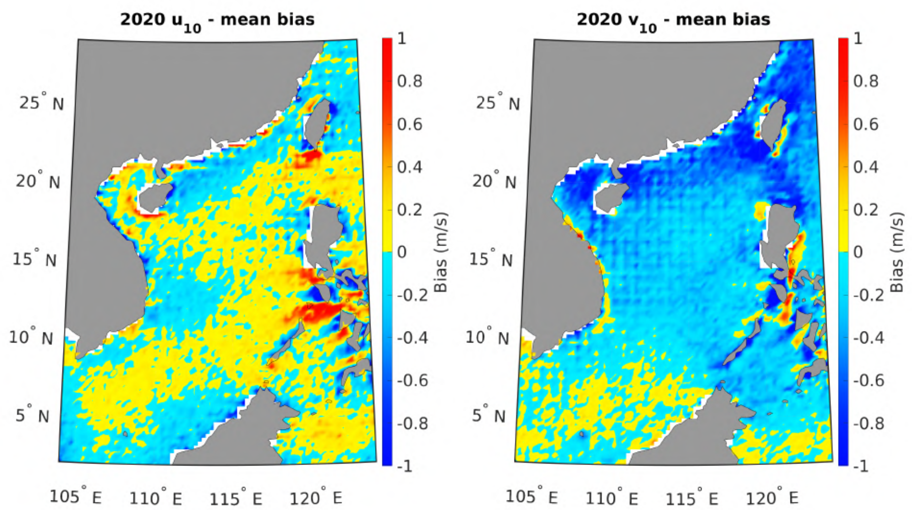

Figure 9.29: Mean annual bias in 2020 for both eastward and northward wind velocity components.

Appendix 2: Comparisons among different coupling strategies

The purpose of this analysis is to prove the differences and benefits of several coupling mechanisms between the hydrodynamic model (SCHISM) and the wave model (WWMIII) in nearshore areas.

W1 station

coupling	CC	BIAS [m]	RMSE [m]	SI	SKILL	NBI [%]	HH
0	0.720	0.063	0.162	0.321	0.560	0.18	0.390
1	0.729	0.061	0.159	0.315	0.581	0.18	0.383
2	0.730	0.062	0.159	0.316	0.586	0.18	0.383
7	0.720	0.063	0.162	0.321	0.560	0.18	0.390

Table 9.1: Statistical parameters at station W1.

W2 station

coupling	CC	BIAS [m]	RMSE [m]	SI	SKILL	NBI [%]	HH
0	0.729	0.118	0.211	0.429	0.650	0.33	0.457
1	0.752	0.142	0.224	0.470	0.761	0.39	0.473
2	0.753	0.142	0.224	0.471	0.766	0.39	0.473
7	0.749	0.143	0.226	0.474	0.763	0.39	0.477

Table 9.2: Statistical parameters at station W2.

Coupling 0 refers to results obtained with WWMIII only, hence no coupling; coupling 1 means that SCHISM and WWMIII are fully coupled; coupling 2 is a one-way coupling (elevation and currents in SCHISM, no wave force in WWMIII); coupling 7 is another type of one-way coupling (no elevation but currents in WWMIII, no wave force in SCHISM). Tables 9.1 and 9.2 show some statistical parameters related to the comparison between observed significant wave heights at stations W1, W2 and simulated significant wave heights under different coupling techniques for a one-year simulation (starting from 01/01/2018).

A similar comparison has been performed using the satellite altimeter data. To this end, only the nodes characterized by a water depth smaller than 200 meters were considered, with the aim to investigate the performance of the model in nearshore areas under different coupling mechanisms. Figure 9.30 shows in red the mesh nodes used for the statistical parameters evaluation. They have been selected among those nodes included between the shoreline and the green line that almost follows the 200 m isobath.

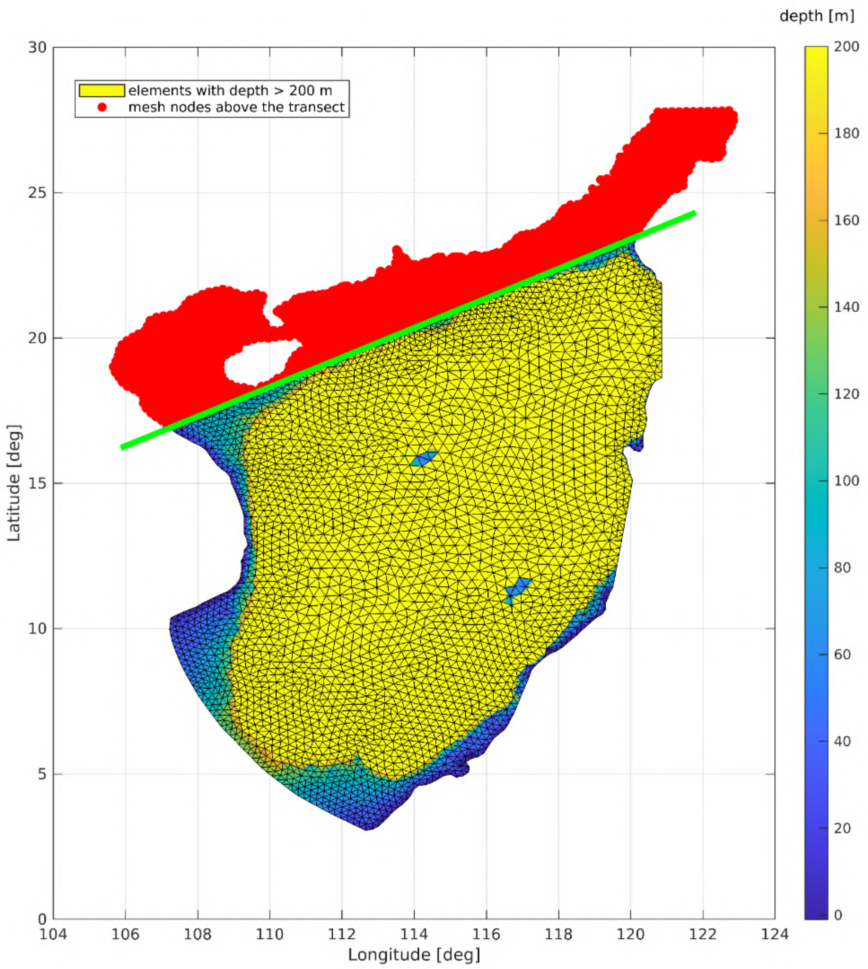

Figure 9.30: Unstructured mesh domain and nodes selected for the comparison.

The results have been reported in the following Table:

Similarly to the analysis performed on the wave heights, also water levels were simulated under different coupling mechanisms and then compared to the observations provided by the tide stations T1, T2, T3 and T4. Statistics are shown in Tables 9.4, 9.5, 9.6 and 9.7:

SATELLITE COMPARISONS - 2018							
coupling	CC	BIAS [m]	RMSE [m]	SI	SKILL	NBI [%]	HH
0	0.906	-0.180	0.380	0.202	0.496	-0.14	0.268
1	0.906	-0.182	0.381	0.202	0.495	-0.14	0.269
2	0.906	-0.182	0.381	0.202	0.495	-0.14	0.269
7	0.906	-0.182	0.382	0.202	0.494	-0.14	0.269

Table 9.3: Statistical parameters of significant wave heights related to the nodes above the selected transect.

T1 station							
coupling	CC	BIAS [m]	RMSE [m]	SI	SKILL	NBI [%]	HH
0	0.831	0.041	0.377	-8.843	0.762	-1.170	0.729
1	0.859	0.123	0.369	-9.860	0.821	-4.000	0.707
2	0.854	0.124	0.377	-10.077	0.814	-4.020	0.721
7	0.854	0.125	0.378	-8.899	0.813	-3.580	0.723

Table 9.4: Statistical parameters at the tidal gauge station T1.

T2 station							
coupling	CC	BIAS [m]	RMSE [m]	SI	SKILL	NBI [%]	HH
0	0.824	0.020	0.380	70.708	0.759	4.510	0.733
1	0.853	0.099	0.367	38.019	0.829	12.340	0.693
2	0.848	0.100	0.375	-38.961	0.823	12.440	0.709
7	0.848	0.102	0.376	70.612	0.822	22.810	0.711

Table 9.5: statistical parameters at the tidal gauge station T2.

T3 station							
coupling	CC	BIAS [m]	RMSE [m]	SI	SKILL	NBI [%]	HH
0	0.817	-0.005	0.390	18.201	0.712	-0.290	0.763
1	0.850	0.075	0.369	14.228	0.798	3.480	0.706
2	0.844	0.076	0.377	14.584	0.790	3.500	0.722
7	0.844	0.077	0.378	17.899	0.789	4.380	0.724

Table 9.6: Statistical parameters at the tidal gauge station T3.

T4 station

coupling	CC	BIAS [m]	RMSE [m]	SI	SKILL	NBI [%]	HH
0	0.778	0.047	0.384	-7.593	0.694	-1.15	0.821
1	0.810	0.129	0.378	-8.241	0.730	-3.49	0.800
2	0.807	0.130	0.384	-8.343	0.726	-3.52	0.809
7	0.809	0.131	0.383	-7.613	0.731	-3.23	0.807

Table 9.7: Statistical parameters at the tidal gauge station T4.

Appendix 3: Simulation of extreme events

Table 9.8 reports the name, date range, maximum wind speed, and minimum pressure for each event. Source: (https://www.ncei.noaa.gov/products/international-best-track-archive).

The comparison between the observed maximum sea level at some station in the Hong Kong Waters and the simulated one using ERA5 forcing or IBtrACS is reported in table format for all events of Table 9.8. The observed data have been downloaded from the official website of the Hong Kong Observatory (https://www.hko.gov.hk/en/wservice/tsheet/pms/stormsurgedb.htm).

Storm name - Year	Date range	Max wind speed [kt]	Min pressure [mb]
NALGAE 2022	Oct 26 - Nov 03	75	972
RAI 2021	Dec 11 - Dec 21	150	908
LUPIT 2021	Aug 02 - Aug 15	45	976
HIGOS 2020	Aug 16 - Aug 20	60	988
MANGKHUT 2018	Sep 06 - Sep 17	155	896
EWINIAR 2018	Jun 02 - Jun 11	40	996
MAWAR 2017	Aug 30 - Sep 04	45	989
PAKHAR 2017	Aug 24 - Aug 28	60	983
HATO 2017	Aug 19 - Aug 25	90	956
ROKE 2017	Jul 21 - Jul 23	35	996
MERBOK 2017	Jun 10 - Jun 13	45	989
HAIMA 2016	Oct 14 - Oct 26	145	914
DIANMU 2016	Aug 15 - Aug 20	45	989
NIDA 2016	Jul 29 - Aug 03	80	963
LINFA 2015	Jul 01 - Jul 10	75	967
USAGI 2013	Sep 16 - Sep 24	135	922
VICENTE 2012	Jul 18 - Jul 25	115	937
DOKSURI 2012	Jun 25 - Jun 30	40	993
KOPPU 2009	Sep 11 - Sep 15	75	967
GONI 2009	Jul 31 - Aug 10	45	988
MOLAVE 2009	Jul 15 - Jul 19	65	974
NANGKA 2009	Jun 22 - Jun 27	45	988
HIGOS 2008	Sep 27 - Oct 06	40	993
NURI 2008	Aug 16 - Aug 23	100	948
KAMMURI 2008	Aug 03 - Aug 08	50	985
FENGSHEN 2008	Jun 17 -Jun 27	110	941
NEOGURI 2008	Apr 13 - Apr 19	100	948
PABUK 2007	Aug 04 - Aug 15	70	970
BOPHA 2006	Aug 05 - Aug 11	55	984
DUJUAN 2003	Aug 27 - Sep 03	125	916
KAMMURI 2002	Aug 01 - Aug 07	50	987
NARI 2001	Sep 05 - Sep 21	100	944

Table 9.8: Official name, date range, maximum wind speed and minimum atmospheric pressure of the events simulated, source International Best Track Archive for Climate Stewardship (IBtrACS).

	Max sea level (above chart datum)		Max sea level (above chart datum)	
Station	Height [m]	Date time	ERA5 Height [m]	IBTRACS Height [m]
Quarry Bay	2.39	2001-09-19 23:08	2.84	2.80
Shek Pik	2.37	2001-09-19 23:33	2.86	2.83
Waglan Island	2.47	2001-09-19 23:34	2.75	2.71

Table 9.9: Water levels comparisons during Typhoon Nari - September 2001.

	Max sea level (above chart datum)		Max sea level (above chart datum)	
Station	Height [m]	Date time	ERA5 Height [m]	IBTRACS Height [m]
Quarry Bay	2.28	2002-08-04 06:17	2.36	2.31
Shek Pik	2.31	2002-08-04 04:56	2.38	2.31
Tai Po Kau	2.08	2002-08-04 05:49	2.41	2.40
Waglan Island	2.43	2002-08-04 06:03	2.34	2.34

Table 9.10: Water levels comparisons during Severe Tropical Storm Kammuri - August 2002.

	Max sea level (above chart datum)		Max sea level (above chart datum)	
Station	Height [m]	Date time	ERA5 Height [m]	IBTRACS Height [m]
Quarry Bay	2.59	2003-09-02 22:40	2.47	2.84
Shek Pik	2.63	2003-09-02 23:37	2.49	2.79
Tai Po Kau	3.54	2003-09-02 22:08	2.57	4.35
Tsim Bei Tsui	3.12	2003-09-03 01:22	2.78	3.44

Table 9.11: Water levels comparisons during Typhoon Dujuan - September 2003.

	Max sea level (above chart datum)		Max sea level (above chart datum)	
Station	Height [m]	Date time	ERA5 Height [m]	IBTRACS Height [m]
Quarry Bay	2.66	2006-08-10 10:11	2.94	2.89
Shek Pik	2.89	2006-08-10 10:12	2.96	2.90
Tai Po Kau	2.71	2006-08-10 10:32	3.01	2.98
Tsim Bei Tsui	3.25	2006-08-10 09:57	3.22	3.21

Table 9.12: Water levels comparisons during Severe Tropical Storm Bopha - August 2006.

	Max sea level (above chart datum)		Max sea level (above chart datum)	
Station	Height [m]	Date time	ERA5 Height [m]	IBTRACS Height [m]
Quarry Bay	2.43	2007-08-08 05:35	2.46	2.68
Shek Pik	2.64	2007-08-08 05:14	2.52	2.73
Tai Miu Wan	2.43	2007-08-08 05:04	2.48	2.83
Tai Po Kau	2.80	2007-08-08 06:34	2.54	3.20
Tsim Bei Tsui	2.51	2007-08-08 05:13	2.63	2.78
Waglan Island	2.75	2007-08-08 04:54	2.46	2.81

Table 9.13: Water levels comparisons during Severe Tropical Storm Pabuk - August 2007.

	Max sea level (above chart datum)		Max sea level (above chart datum)	
Station	Height [m]	Date time	ERA5 Height [m]	IBTRACS Height [m]
Quarry Bay	2.08	2008-04-19 08:54	2.72	2.56
Shek Pik	2.36	2008-04-19 09:37	2.77	2.64
Tai Miu Wan	2.09	2008-04-19 08:50	2.64	2.48
Tai Po Kau	2.23	2008-04-19 10:13	2.73	2.58
Waglan Island	2.20	2008-04-19 08:46	2.62	2.47

Table 9.14: Water levels comparisons during Typhoon Neoguri - April 2008.

	Max sea level (above chart datum)		Max sea level (above chart datum)	
Station	Height [m]	Date time	ERA5 Height [m]	IBTRACS Height [m]
Quarry Bay	1.95	2008-06-23 10:54	2.64	2.59
Shek Pik	2.38	2008-06-23 11:25	2.67	2.61
Tai Miu Wan	2.25	2008-06-23 10:33	2.58	2.59
Tai Po Kau	2.18	2008-06-23 10:21	2.66	3.13
Waglan Island	2.18	2008-06-23 10:38	2.58	2.56

Table 9.15: Water levels comparisons during Typhoon Fengshen - June 2008.

	Max sea level (above chart datum)		Max sea level (above chart datum)	
Station	Height [m]	Date time	ERA5 Height [m]	IBTRACS Height [m]
Quarry Bay	2.16	2008-08-06 13:03	2.75	2.78
Shek Pik	2.67	2008-08-06 12:25	2.82	3.08
Tai Po Kau	2.82	2008-08-06 09:25	2.86	2.77
Waglan Island	2.42	2008-08-06 10:12	2.69	2.60

Table 9.16: Water levels comparisons during Severe Tropical Storm Kammuri - August 2008.

	Max sea level (above chart datum)		Max sea level (above chart datum)	
Station	Height [m]	Date time	ERA5 Height [m]	IBTRACS Height [m]
Quarry Bay	2.16	2008-08-22 11:10	2.50	2.58
Shek Pik	2.46	2008-08-22 00:30	2.51	2.59
Tai Miu Wan	2.50	2008-08-22 11:10	2.50	2.78
Tai Po Kau	2.61	2008-08-22 13:51	2.62	3.89
Waglan Island	2.43	2008-08-22 12:15	2.48	2.71

Table 9.17: Water levels comparisons during Typhoon Nuri - August 2008.

	Max sea level (above chart datum)		Max sea level (above chart datum)	
Station	Height [m]	Date time	ERA5 Height [m]	IBTRACS Height [m]
Quarry Bay	2.33	2008-10-03 21:39	2.73	2.55
Tai Po Kau	2.45	2008-10-03 00:17	2.74	2.52
Tsim Bei Tsui	2.60	2008-10-03 23:08	3.07	2.82

Table 9.18: Water levels comparisons during Tropical Storm Higos - October 2008.

	Max sea level (above chart datum)		Max sea level (above chart datum)	
Station	Height [m]	Date time	ERA5 Height [m]	IBTRACS Height [m]
Quarry Bay	2.58	2009-06-26 10:53	2.99	2.88
Shek Pik	2.71	2009-06-26 10:54	3.04	2.90
Tai Miu Wan	2.55	2009-06-26 12:06	2.96	2.83
Tai Po Kau	2.59	2009-06-26 13:09	3.09	2.92
Tsim Bei Tsui	3.05	2009-06-26 11:52	3.36	3.23
Waglan Island	2.58	2009-06-26 11:50	2.94	2.81

Table 9.19: Water levels comparisons during Tropical Storm Nangka - June 2009.

	Max sea level (above chart datum)		Max sea level (above chart datum)	
Station	Height [m]	Date time	ERA5 Height [m]	IBTRACS Height [m]
Quarry Bay	2.67	2009-07-19 03:30	2.49	2.69
Shek Pik	2.63	2009-07-19 05:48	2.50	2.72
Tai Miu Wan	2.67	2009-07-19 03:29	2.46	2.62
Tai Po Kau	2.90	2009-07-19 03:43	2.54	3.05
Tsim Bei Tsui	3.15	2009-07-19 04:57	2.92	3.39

Table 9.20: Water levels comparisons during Typhoon Molave - July 2009.

	Max sea level (above chart datum)		Max sea level (above chart datum)	
Station	Height [m]	Date time	ERA5 Height [m]	IBTRACS Height [m]
Quarry Bay	2.58	2009-08-04 07:53	2.71	2.68
Shek Pik	2.61	2009-08-04 07:07	2.77	2.82
Tai Miu Wan	2.58	2009-08-04 07:40	2.70	2.56
Tai Po Kau	2.55	2009-08-04 05:56	2.79	2.68
Waglan Island	2.72	2009-08-04 07:26	2.68	2.54

Table 9.21: Water levels comparisons during Severe Tropical Storm Goni - August 2009.

	Max sea level (above chart datum)		Max sea level (above chart datum)	
Station	Height [m]	Date time	ERA5 Height [m]	IBTRACS Height [m]
Quarry Bay	3.02	2009-09-15 04:33	2.55	3.08
Tai Po Kau	3.43	2009-09-15 01:43	2.58	3.04

Table 9.22: Water levels comparisons during Typhoon Koppu - September 2009.

	Max sea level (above chart datum)		Max sea level (above chart datum)	
Station	Height [m]	Date time	ERA5 Height [m]	IBTRACS Height [m]
Quarry Bay	2.33	2012-06-30 05:03	2.59	2.66
Shek Pik	2.56	2012-06-30 04:33	2.64	2.72
Tai Miu Wan	2.35	2012-06-30 04:30	2.55	2.59
Tai Po Kau	2.47	2012-06-30 05:57	2.64	2.75
Tsim Bei Tsui	2.91	2012-06-30 05:13	2.98	3.01
Waglan Island	2.42	2012-06-30 04:22	2.53	2.56

Table 9.23: Water levels comparisons during Tropical Storm Doksuri - June 2012.

	Max sea level (above chart datum)		Max sea level (above chart datum)	
Station	Height [m]	Date time	ERA5 Height [m]	IBTRACS Height [m]
Quarry Bay	2.76	2012-07-24 01:48	2.88	3.74
Shek Pik	3.19	2012-07-24 02:08	2.93	5.17
Tai Miu Wan	2.78	2012-07-24 01:45	2.88	3.49
Tai Po Kau	3.09	2012-07-24 01:53	3.07	3.94

Table 9.24: Water levels comparisons during Severe Typhoon Vicente - July 2012.

	Max sea level (above chart datum)		Max sea level (above chart datum)	
Station	Height [m]	Date time	ERA5 Height [m]	IBTRACS Height [m]
Quarry Bay	2.81	2013-09-22 22:58	2.66	2.94
Shek Pik	2.78	2013-09-22 23:24	2.68	2.95
Tai Miu Wan	2.69	2013-09-22 22:55	2.63	2.92
Tai Po Kau	3.16	2013-09-22 22:32	2.71	3.31
Tsim Bei Tsui	3.38	2013-09-23 00:28	3.16	3.42
Waglan Island	2.91	2013-09-22 22:56	2.61	2.90

Table 9.25: Water levels comparisons during Super Typhoon Usagi - September 2013.

	Max sea level (above chart datum)		Max sea level (above chart datum)	
Station	Height [m]	Date time	ERA5 Height [m]	IBTRACS Height [m]
Quarry Bay	2.22	2015-07-08 14:27	2.44	2.40
Tai Miu Wan	2.16	2015-07-08 14:16	2.39	2.36
Tai Po Kau	2.29	2015-07-10 05:03	2.54	2.46
Tsim Bei Tsui	2.33	2015-07-08 14:11	2.38	2.53
Waglan Island	2.37	2015-07-10 04:50	2.38	2.35

Table 9.26: Water levels comparisons during Typhoon Linfa - July 2015.

	Max sea level (above chart datum)		Max sea level (above chart datum)	
Station	Height [m]	Date time	ERA5 Height [m]	IBTRACS Height [m]
Quarry Bay	2.93	2016-08-02 08:22	2.96	3.33
Shek Pik	3.08	2016-08-02 08:06	3.00	3.36
Tai Miu Wan	2.83	2016-08-02 08:09	2.92	3.23
Tai Po Kau	2.76	2016-08-02 08:12	2.95	3.36
Tsim Bei Tsui	3.60	2016-08-02 09:49	3.42	3.93
Waglan Island	2.92	2016-08-02 08:01	2.90	3.17

Table 9.27: Water levels comparisons during Typhoon Nida - July 2016.

	Max sea level (above chart datum)		Max sea level (above chart datum)	
Station	Height [m]	Date time	ERA5 Height [m]	IBTRACS Height [m]
Quarry Bay	2.54	2016-08-18 08:05	2.73	2.68
Shek Pik	2.72	2016-08-18 08:01	2.78	2.72
Tai Miu Wan	2.44	2016-08-18 07:56	2.68	2.62
Tai Po Kau	2.43	2016-08-18 08:19	2.75	2.67
Tsim Bei Tsui	3.15	2016-08-18 09:36	3.04	2.97
Waglan Island	2.52	2016-08-18 07:31	2.66	2.61

Table 9.28: Water levels comparisons during Tropical Storm Dianmu - August 2016.

	Max sea level (above chart datum)		Max sea level (above chart datum)	
Station	Height [m]	Date time	ERA5 Height [m]	IBTRACS Height [m]
Quarry Bay	2.74	2016-10-21 00:28	2.63	2.84
Shek Pik	2.75	2016-10-21 01:01	2.62	2.82
Tai Miu Wan	2.75	2016-10-21 01:34	2.61	2.89
Tai Po Kau	2.80	2016-10-21 01:28	2.63	3.09

Table 9.29: Water levels comparisons during Super Typhoon Haima - October 2016.

	Max sea level (above chart datum)		Max sea level (above chart datum)	
Station	Height [m]	Date time	ERA5 Height [m]	IBTRACS Height [m]
Quarry Bay	2.35	2017-06-12 10:12	2.64	2.66
Shek Pik	2.57	2017-06-12 10:06	2.69	2.72
Tai Miu Wan	2.36	2017-06-12 10:35	2.62	2.67
Tai Po Kau	2.28	2017-06-12 11:46	2.67	2.86
Tsim Bei Tsui	2.86	2017-06-12 11:13	2.97	2.62
Waglan Island	2.42	2017-06-12 09:29	2.61	2.65

Table 9.30: Water levels comparisons during Severe Tropical Storm Merbok - June 2017.

	Max sea level (above chart datum)		Max sea level (above chart datum)	
Station	Height [m]	Date time	ERA5 Height [m]	IBTRACS Height [m]
Quarry Bay	2.66	2017-07-23 08:53	3.05	2.92
Shek Pik	2.75	2017-07-23 08:04	3.11	2.87
Tai Miu Wan	2.61	2017-07-23 09:06	2.97	2.90
Tsim Bei Tsui	3.18	2017-07-23 09:04	3.44	3.16
Waglan Island	2.71	2017-07-23 08:58	2.95	2.87

Table 9.31: Water levels comparisons during Tropical Storm Roke - July 2017.

	Max sea level (above chart datum)		Max sea level (above chart datum)	
Station	Height [m]	Date time	ERA5 Height [m]	IBTRACS Height [m]
Quarry Bay	3.57	2017-08-23 10:27	3.07	3.96
Shek Pik	3.91	2017-08-23 11:30	2.99	4.73
Tai Miu Wan*	3.14	2017-08-23 07:53	3.16	4.04
Tai Po Kau	4.09	2017-08-23 10:58	3.39	5.17
Waglan Island*	2.97	2017-08-23 07:35	3.10	3.60

Table 9.32: Water levels comparisons during Super Typhoon Hato - August 2017.

	Max sea level (above chart datum)		Max sea level (above chart datum)	
Station	Height [m]	Date time	ERA5 Height [m]	IBTRACS Height [m]
Quarry Bay	2.23	2017-08-27 02:45	2.31	2.43
Shek Pik	2.38	2017-08-27 12:22	2.36	2.47
Tai Miu Wan	2.23	2017-08-27 00:51	2.27	2.37
Tai Po Kau	2.28	2017-08-27 02:14	2.36	2.44
Tsim Bei Tsui	2.63	2017-08-27 12:51	2.49	2.56
Waglan Island	2.27	2017-08-27 02:48	2.26	2.37

Table 9.33: Water levels comparisons during Severe Tropical Storm Pakhar - August 2017.

	Max sea level (above chart datum)		Max sea level (above chart datum)	
Station	Height [m]	Date time	ERA5 Height [m]	IBTRACS Height [m]
Quarry Bay	2.41	2017-09-03 06:22	2.45	2.52
Shek Pik	2.48	2017-09-03 06:42	2.47	2.53
Tai Miu Wan	2.39	2017-09-03 06:39	2.39	2.47
Tai Po Kau	2.36	2017-09-03 07:23	2.44	2.54
Tsim Bei Tsui	2.89	2017-09-03 08:11	2.66	2.71
Waglan Island	2.42	2017-09-03 06:33	2.39	2.45

Table 9.34: Water levels comparisons during Severe Tropical Storm Mawar - September 2017.

	Max sea level (above chart datum)		Max sea level (above chart datum)	
Station	Height [m]	Date time	ERA5 Height [m]	IBTRACS Height [m]
Quarry Bay	2.18	2018-06-05 12:59	2.27	2.12
Shek Pik	2.24	2018-06-05 11:44	2.32	2.14
Tai Miu Wan	2.08	2018-06-05 12:43	2.24	2.09
Tai Po Kau	2.13	2018-06-05 11:17	2.27	2.12
Tsim Bei Tsui	2.52	2018-06-05 13:34	2.38	2.22

Table 9.35: Water levels comparisons during Tropical Storm Ewiniar - June 2018.

	Max sea level (above chart datum)		Max sea level (above chart datum)	
Station	Height [m]	Date time	ERA5 Height [m]	IBTRACS Height [m]
Quarry Bay	3.88	2018-09-16 14:42	2.82	3.73
Shek Pik	3.89	2018-09-16 14:16	2.94	4.50
Tai Miu Wan*	4.19	2018-09-16 13:41	2.92	4.11
Tai Po Kau	4.71	2018-09-16 12:34	3.27	5.12

Table 9.36: Water levels comparisons during Super Typhoon Mangkhut - September 2018.

	Max sea level (above chart datum)		Max sea level (above chart datum)	
Station	Height [m]	Date time	ERA5 Height [m]	IBTRACS Height [m]
Quarry Bay	2.75	2020-08-19 07:28	2.95	3.16
Shek Pik	3.00	2020-08-19 07:22	2.99	3.30
Tai Miu Wan	2.79	2020-08-19 07:40	2.87	2.79
Tai Po Kau	2.77	2020-08-19 06:43	2.98	3.26

Table 9.37: Water levels comparisons during Typhoon Higos - August 2020.

	Max sea level (above chart datum)		Max sea level (above chart datum)	
Station	Height [m]	Date time	ERA5 Height [m]	IBTRACS Height [m]
Quarry Bay	2.14	2021-08-04 06:30	2.27	2.19
Shek Pik	2.20	2021-08-04 06:29	2.29	2.21
Tai Miu Wan	2.15	2021-08-04 05:59	2.22	2.16
Tai Po Kau	2.15	2021-08-04 05:51	2.29	2.16
Tsim Bei Tsui	2.33	2021-08-04 06:02	2.48	2.26

Table 9.38: Water levels comparisons during Tropical Storm Lupit - August 2021.

	Max sea level (above chart datum)		Max sea level (above chart datum)	
Station	Height [m]	Date time	ERA5 Height [m]	IBTRACS Height [m]
Quarry Bay	2.56	2021-12-20 21:17	2.87	2.61
Shek Pik	2.68	2021-12-20 21:00	2.90	2.64
Tai Miu Wan	2.53	2021-12-20 21:05	2.82	2.55
Tai Po Kau	2.53	2021-12-20 19:49	2.91	2.60
Tsim Bei Tsui	2.93	2021-12-20 22:13	3.22	2.87

Table 9.39: Water levels comparisons during Super Typhoon Rai - December 2021.

	Max sea level (above chart datum)		Max sea level (above chart datum)	
Station	Height [m]	Date time	ERA5 Height [m]	IBTRACS Height [m]
Quarry Bay	2.93	2022-11-02 02:38	2.70	2.37
Shek Pik	2.99	2022-11-02 02:41	2.68	2.40
Tai Miu Wan	2.95	2022-11-02 03:14	2.68	2.42
Tai Po Kau	2.95	2022-11-02 01:56	2.71	2.63
Tsim Bei Tsui	3.00	2022-11-02 03:54	2.77	2.36

Table 9.40: Water levels comparisons during Severe Tropical Storm Nalgae - November 2022.

* refers to incomplete data.